Georgia State University
ScholarWorks @ Georgia State University

Physics and Astronomy Dissertations | Department of Physics and Astronomy

Summer 8-12-2013

Indium Nitride Surface Structure, Desorption Kinetics and Thermal Stability

Ananta R. Acharya

Follow this and additional works at: https://scholarworks.gsu.edu/phy_astr_diss

Recommended Citation
Acharya, Ananta R., "Indium Nitride Surface Structure, Desorption Kinetics and Thermal Stability." Dissertation, Georgia State University, 2013.
https://scholarworks.gsu.edu/phy_astr_diss/62

This Dissertation is brought to you for free and open access by the Department of Physics and Astronomy at ScholarWorks @ Georgia State University. It has been accepted for inclusion in Physics and Astronomy Dissertations by an authorized administrator of ScholarWorks @ Georgia State University. For more information, please contact scholarworks@gsu.edu.

INDIUM NITRIDE SURFACE STRUCTURE, DESORPTION KINETICS AND THERMAL STABILITY

by

ANANTA ACHARYA

Under the Direction of Dr. Brian D. Thoms

ABSTRACT

Unique physical properties such as small effective mass, high electron drift velocities, high electron mobility and small band gap energy make InN a candidate for applications in high-speed microelectronic and optoelectronic devices. The aim of this research is to understand the surface properties, desorption kinetics and thermal stability of InN epilayers that affect the growth processes and determine film quality as well as device performance and life time. We have investigated the structural properties, the surface desorption kinetics, and the thermal stability using Auger electron spectroscopy (AES), x-ray diffraction (XRD), Raman spectroscopy, atomic force microscopy (AFM), high resolution electron energy loss spectroscopy

(HREELS), and temperature programmed desorption (TPD). Investigations on high pressure chemical vapor deposition (HPCVD)-grown InN samples revealed the presence of tilted crystallites, which were attributed to high group V/III flux ratio and lattice mismatch. A study of the thermal stability of HPCVD-grown InN epilayers revealed that the activation energy for nitrogen desorption was 1.6±0.2 eV, independent of the group V/III flux ratio. Initial investigations on the ternary alloy $In_{0.96}Ga_{0.04}N$ showed single-phase, N-polar epilayers using XRD and HREELS, while a thermal desorption study revealed an activation energy for nitrogen desorption of 1.14 ± 0.06 eV.

HREELS investigations of atomic layer epitaxy (ALE)-grown InN revealed vibrational modes assigned to N-N vibrations. The atomic hydrogen cleaned InN surface also exhibited modes assigned to surface N-H without showing In-H species, which indicated N-polar InN. Complete desorption of hydrogen from the InN surface was best described by the first-order desorption kinetics with an activation energy of 0.88 ± 0.06 eV and pre-exponential factor of $(1.5 \pm 0.5) \times 10^5\ s^{-1}$.

Overall, we have used a number of techniques to characterize the structure, surface bonding configuration, thermal stability and hydrogen desorption kinetics of InN and $In_{0.96}Ga_{0.04}N$ epilayers grown by HPCVD and ALE. High group V/III precursors ratio and lattice mismatch have a crucial influence on the film orientation. The effects of hydrogen on the decomposition add to the wide variation in the activation energy of nitrogen desorption. Presence of surface defects lowers the activation energy for hydrogen desorption from the surface.

INDEX WORDS: Indium nitride, surface structure, high resolution electron energy loss spectroscopy, tilted crystallites, polarity, thermal desorption, activation energy

INDIUM NITRIDE SURFACE STRUCTURE, DESORPTION KINETICS AND THERMAL STABILITY

by

ANANTA ACHARYA

A Dissertation Submitted in Partial Fulfillment of the Requirements for the Degree of

Doctor of Philosophy

in the College of Arts and Sciences

Georgia State University

2013

Copyright by
Ananta Raj Acharya
2013

INDIUM NITRIDE SURFACE STRUCTURE, DESORPTION KINETICS AND THERMAL STABILITY

by

ANANTA ACHARYA

Committee Chair: Brian D. Thoms

Committee: Nikolaus Dietz

Vadyam Apalkov

Douglas Gies

Mukesh Dhamala

Electronic Version Approved:

Office of Graduate Studies

College of Arts and Sciences

Georgia State University

August 2013

Dedicated to my parents, lovely daughter Monica, son Asmin

And

wife Muna

ACKNOWLEDGEMENTS

I would like to express my deepest gratitude and sincere thanks to a number of people who inspired and supported me towards my Ph.D. studies and helped me complete it. First of all, I would like to thank my advisor Dr. Brian D. Thoms for his continuous guidance and supervision that made this work possible. He was always ready to explain and help me when I had problems and confusion about conducting experiments, maintaining devices, analyzing the data and correcting my writing. I found myself extremely fortunate to work with an advisor like Dr. Thoms.

Next, I would like to express my sincere thanks to Prof. Nikolaus Dietz, not only for providing the InN and InGaN samples but also for reviewing the contents of my papers and his constructive advice from his expertise in nitride semiconductors. I am grateful to my previous lab mate, Dr. Rudra P. Bhatta, who helped me in handling and maintaining UHV equipment, and running the experiments. I definitely express my thanks to Dr. Max Buegler and Sampath Gamage from Dr. Dietz's group who worked late nights frequently to produce good quality InN and InGaN samples. Also, I am grateful to other members in Dr. Dietz's research group, Dr. Ramazan Atalay, Indika Kankanamge, Rasanga Samaraweera, and Kasuni Nanayakkara for their valuable suggestions and conversations related to research and daily life. I would like to acknowledge Charles Hopper, Peter Walker and others in the instrument shop of Physics and Astronomy at GSU for construction and repairing parts of UHV system. I want to gratefully acknowledge former head of the department Dr. Richard Miller, former graduate director Dr. Unil Perera, present department chair Dr. Michael Crenshaw, and graduate director Dr. Xiaochun

He for helping me in every aspect and providing me with useful guidance in order to complete my graduate study.

I would like to thank to my parents, my daughter Monica, son Asmin and my brothers for their unconditional infinite love and support throughout my endeavor. I am forever indebted to them for their constant support which made me what I am today. Finally, I would like to express my special thanks to my lovely wife, Muna, for her all love, invaluable dedication, sacrifice and companionship. For me, she has always been a source of inspiration to work hard and succeed. Without her presence, it would have been much more difficult to finish this dissertation. Being the closest person to me, she had to suffer through a number of ups and downs during my Ph.D. studies. However, she never stopped bringing happiness and joy in my life which always encouraged me to work harder and make my studies successful. Thank you so much for everything you have done for me.

TABLE OF CONTENTS

ACKNOWELEDGEMENTS……………………………………………………………v

LIST OF TABLES..xi

LIST OF FIGURES xii

LIST OF ABBREVIATIONS...xiv

1 INTRODUCTION AND MOTIVATION ………………………………………....1

1.1 Introduction...1

1.2 Motivation 3

2 GROUP III-NITRIDE SEMICONDUCTORS 5

2.1 Introduction 5

2.2 Properties 6

2.3 InN 10

2.3.1 Introduction 10

2.3.2 Growth.. 12

2.3.2.1 Metal organic chemical vapor deposition 13

2.3.2.2 Molecular beam epitaxy.. 15

2.3.2.3 High pressure chemical vapor deposition 17

2.3.2.4 Hydride vapor phase epitaxy 18

2.3.2.5 Atomic layer deposition 19

2.3.3 Structural properties...21

2.3.4 Electrical properties... 22

2.3.5 Optical properties... 24

2.3.6 Polarity... 25

2.3.7 Desorption of hydrogen 28

2.4 References 30

3 CHARATERIZATION TECHNIQUES AND METHODS 38

3.1 Introduction 38

3.2 Low energy electron diffraction 39

3.3 Auger electron spectroscopy 43

3.4 Raman spectroscopy 48

3.5 X-ray diffraction 51

3.6 Infrared reflection spectroscopy 53

3.6.1 Theoretical model 53

3.6.2 Experimental methods 54

3.7 High resolution electron energy loss spectroscopy 54

3.8 Temperature programed desorption 59

3.8.1 Experimental set up 59

3.8.2 Theoretical background 60

3.9 Atomic force microscopy 64

3.10 Experimental methods 67

3.10.1 Sputtering 67

3.10.2 Atomic hydrogen cleaning 68

3.10.3 Annealing 71

3.11 Gas handling system 72

3.12 References 73

4 OBSERVATION OF NH2 SPECIES ON TILTED INDIUM NITRIDE(01$\bar{1}$ 1) FACETS........ 76

4.1 Abstract........ 76

4.2 Introduction........ 76

4.3 Experimental methods........ 78

4.4 Results and discussion........ 80

4.5 Conclusion........ 84

4.6 References........ 91

5 THERMAL STABILITY OF INDIUM NITRIDE EPILAYERS GROWN BY HIGH PRESSURE CHEMICAL VAPOR DEPOSITION........95

5.1 Abstract........ 95

5.2 Introduction........ 95

5.3 Experimental methods........ 98

5.4 Results and discussion........ 100

5.5 Conclusion........ 103

5.6 References........ 110

6 SURFACE STRUCTURE, POLARITY AND SURFACE KINETICS OF INDIUM NITRIDE GROWN BY PLASMA-ASSISTED ATOMIC LAYER EPITAXY: A HREELS STUDY........112

6.1 Abstract........ 112

6.2 Introduction........ 112

6.3 Experimental methods........ 114

6.4 Results and discussion........ 116

6.5 Conclusion 120

6.6 References 124

7 STURCTURAL, COMPOSITIONAL, AND THERMAL STABILITY STUDIES ON $In_{1-X}Ga_XN$ EPILAYERS GROWN BY HIGH PRESSURE CHEMICAL VAPOR DEPOSITION 126

7.1 Abstract 126

7.2 Introduction 127

7.3 Experimental methods 128

7.4 Results and discussion 130

7.5 Conclusion 134

7.6 References 138

8 SUMMARY AND FUTURE WORK 141

8.1 Summary 141

8.2 Furure work 143

8.3 References 145

LIST OF TABLES

Table 2.1 Properties of wurtzite III-nitride materials 9

Table 3.1 Raman selection rules for hexagonal group III-nitrides. 50

Table 4.1 Raman spectroscopy results and assignments 86

Table 4.2 HREELS vibrational frequencies and assignments from InN 87

Table 5.1 Summary of the results for thermal stability of InN reported in the literature and current work 105

LIST OF FIGURES

Figure 2.1 Wurtzite crystal structures of a) In-polar InN and b) N-polar InN............................ 27

Figure 3.1 Schematic diagram of the LEED system.. 42

Figure 3.2. Schematic representation of Auger electron process...46

Figure 3.3 Schematic diagram of AES apparatus...47

Figure 3.4 A schematic diagram of x-ray diffraction...52

Figure 3.5 Schematic representation of HREELS theory...57

Figure 3.6 Schematic representation of HREEL spectrometer..58

Figure 3.7 Schematic diagram of TPD system..62

Figure 3.8 Schematic representation of various desorption orders from the surface....................63

Figure 3.9 Diagram of an atomic force microscopy set up.. 66

Figure 3.10 Schematic representation of atomic hydrogen cleaning process...............................70

Figure 4.1 Raman spectrum of an InN layer grown on sapphire with deconvolution of the Raman modes using Gaussian curves...88

Figure 4.2 X-Ray diffraction results of HPCVD-grown InN in ω-2Θ-geometry……………….89

Figure 4.3 HREEL spectra of HPCVD-grown InN after atomic hydrogen cleaning……………90

Figure 5.1 Mass spectrometer signal intensity of nitrogen species desorbed from InN as a function of temperature. These data were collected from InN layer grown with a V/III precursor ratio of 2400 although data from other samples are similar…………………………106

Figure 5.2 Mass spectrometer signal intensity for 28 amu as a function of temperature measured while sample temperature was increased linearly at 30 °C /min from InN samples of V/III precursor ratios varying from 1200 to 4800…………………………………107

Figure 5.3 1µm × 1µm AFM images for InN epilayers deposited on sapphire (0001) substrates. The layers were grown with group V/III molar precursor ratios of (a) 1200 (b) 2400, and (c)

4800. Analysis of the images yields average grain sizes of 180 nm, 200 nm and 220 nm for the three films, respectively..108

Figure 5.4 Natural log of 28 amu mass spectrometer signal as a function of 1/kT for InN sample with V/III- ratio of 2400 while sample temperature was linearly increased at 30 °C per minute. The activation energy was calculated using the slope of the best fit line for the linear region of the graph...109

Figure 6.1 HREELS of InN after atomic hydrogen and atomic deuterium cleaning. Spectra were acquired in the specular direction with an incident electron energy of 7.0 eV..................121

Figure 6.2 HREEL spectra after InN sample preparation by atomic deuterium cleaning (ADC) and after heating to 275, 300, 325, 350 and 375 ºC for 900 s. The surface was restored to the same initial state with ADC prior to each heat treatment...................................122

Figure 6.3 Fitting of first and second-order desorption kinetics to deuterium coverage (obtained from HREELS N-D stretch intensity) for InN sample after preparation by atomic deuterium cleaning and after heating for 900 s to 275, 300, 325, 350, and 375 ºC. Equations and parameters used in the fitting are described in the text.. 123

Figure 7.1 X-Ray diffraction results of HPCVD-grown $In_{0.96}Ga_{0.04}N$ in ω-2Θ-geometry......... 135

Figure 7.2 HREEL spectra of HPCVD-grown $In_{0.96}Ga_{0.04}N$ after atomic hydrogen and atomic deuterium cleaning..136

Figure 7.3 Mass spectrometer signal intensity of nitrogen species desorbed from $In_{0.96}Ga_{0.04}N$ as a function of temperature...137

LIST OF ABBREVIATIONS

ADC	atomic deuterium cleaning
AES	auger electron spectroscopy
AHC	atomic hydrogen cleaning
Al	aluminum
ALD	atomic layer deposition
ALE	atomic layer epitaxy
AlGaN	aluminum gallium nitride
AlGaInN	aluminum gallium indium nitride
AlN	aluminum nitride
Al_2O_3	alumina (sapphire)
Ar	argon
CAICISS	coaxial impact collision ion scattering spectroscopy
CBED	convergent beam electron diffraction
CCD	charge-coupled device
CO	carbon monoxide
D_2	deuterium
ECR	electron cyclotron resonance
EELS	electron energy loss spectroscopy
F-K	Fuchs-Kliewer
FWHM	full-width at half-maximum
Ga	galllium
GaAs	gallium arsenide

GaN	gallium nitride
GPa	gigapascal
H_2	hydrogen
HPCVD	high pressure chemical vapor deposition
HREELS	high resolution electron energy loss spectroscopy
HVPE	hydride vapor phase epitaxy
In	indium
InAlN	indium aluminum nitride
InCl	indium chloride
$InCl_3$	indium trichloride
InGaAlN	indium gallium aluminum nitride
InGaN	indium gallium nitride
InH	indium hydrogen
InN	indium nitride
InP	indium phosphide
IR	infrared
K	kelvin
keV	kiloelectron volt
KOH	potasium hydroxide
L	Langmuir
LCD	liquid crystal diode
LD	laser diode
LED	light emitting diode

LO	longitudinal optical
LPCVD	low-pressure chemical vapor deposition
LPE	liquid phase epitaxy
MEE	migration enhanced epitaxy
MESFET	metal-semiconductor field effect transistor
MgO	magnesium oxide
MMHy	monomethylhydrazine
MOCVD	metal organic chemical vapor deposition
N_2	nitrogen
NaOH	sodium hydroxide
NH_3	ammonia
N-H	nitrogen-hydrogen
N-N	nitrogen- nitrogen
PA-ALE	plasma-assisted atomic layer epitaxy
PID	proportional integral differential
PL	photoluminescence
PLE	photoluminescence excitation
PR	photo modulated reflection
QMS	quadrupole mass spectrometer
RBS	rutherford back scattering spectroscopy
RF	radio-frequency
RFA	retarding field analyzer
Ru	ruthenium

SCCM	standard cubic centimeter
Si	silicon
STM	scanning tunneling microscope
TEM	transmission electron microscopy
TMG	trimethylgallium
TMI	trimethylindium
TO	transverse optical
TPD	temperature programmed desorption
UHP	ultrahigh purity
UHV	ultrahigh vacuum
UV	ultraviolet
XRD	x-ray diffraction
W	watt

1 INTRODUCTION AND MOTIVATION

1.1 Introduction

This thesis describes the surface properties, desorption kinetics and thermal stability of InN and $In_{1-x}Ga_xN$ epilayers. This work contains a detailed description of the characterization techniques and apparatus in addition to the results of the investigations themselves. Chapter 2 gives an introduction to Group III-nitride semiconductors, especially InN, which is followed by a discussion of some important properties and applications. In addition, a brief introduction of the most common growth techniques for III-nitride semiconductors is presented. In chapter 3, the experimental techniques and methods which were employed to characterize the grown films are discussed. The structure, film orientation and surface configuration of high pressure chemical vapor deposition (HPCVD)-grown InN are described in chapter 4. An investigation of thermal stability of HPCVD-grown InN epilayers is reported in chapter 5. In chapter 6, the surface properties and the desorption of hydrogen from the atomic layer deposition (ALD)-grown N-polar InN surface are presented along with the determination of the thermal desorption kinetic parameters. In chapter 7, structural, compositional, and thermal stability studies on $In_{0.96}Ga_{0.04}N$ epilayers are discussed. Finally, the important conclusions of the whole study and future goals of the research are presented in chapter 8.

The experimental results discussed in chapters 4 and 5 have already been published in scientific journals.

- **Observation of NH_2 species on tilted InN($01\bar{1}1$) facets**

  A. R. Acharya, M. Buegler, R. Atalay, J. S. Tweedie, R. Collazo, N. Dietz, and B. D. Thoms, Journal of Vacuum Science and Technology A 29 (4), 041402 (2011).

- **Thermal stability of InN epilayers grown by high pressure chemical vapor Deposition**

  A.R. Acharya, S. Gamage, M. K. I. Senevirathne, M. Alevli, K. Bahadir, A. G. Melton, I. Ferguson, N. Dietz, and B. D. Thoms, Applied Surface Science **269**, 1 (2013).

In addition, one related article has been published that is not included in this dissertation.

- **Effect of reactor pressure on the electrical and structural properties of InN epilayers grown by high-pressure chemical vapor deposition**

  M. K. I. Senevirathna, S. Gamage, R. Atalay, **A. R. Acharya**, A. G. U. Perera, M. Buegler, A. Hoffmann, L. Su, A. Melton, I. Ferguson, and N. Dietz

  J. Vac. Sci. Technol. A 30, 031511 (2012).

The experimental results discussed in chapters 6 and 7 are being prepared for submission.

- **Surface structure, polarity and surface kinetics of InN grown by Atomic Layer Deposition: A HREELS study**

  A. R. Acharya, N. Nepal, C. R. Eddy, and B. D. Thoms, in preparation (2013).

- **Structural, compositional, and thermal stability studies on $In_{0.96}Ga_{0.04}N$ epilayers grown by high pressure chemical vapor deposition**

  A. R. Acharya, M. Buegler, S. Gamage, N. Dietz and B. D. Thoms, in preparation

  (2013).

One additional study is being prepared for publication but is not included in this dissertation.

- **Desorption of hydrogen from a mixed polar InN surface grown by high pressure chemical vapor deposition: A HREELS and TPD study**

  A. R. Acharya, S. Gamage, N. Dietz and B. D. Thoms, in preparation (2013).

1.2 Motivation

The unique physical properties of InN such as low effective mass, high electron mobility, saturation velocity and direct band gap make it a potential material for optoelectronic and microelectronic device structures such as light emitters, sensors, and high electron mobility transistors. In addition, InN is one of the binary corners in the ternary alloy system, $In_{1-x}Ga_xN$. By changing the composition of In, the band gap of $In_{1-x}Ga_xN$ can be tuned from 0.7 eV to 3.4 eV covering a broad range of spectrum from near infrared to ultraviolet regions. This property has made the $In_{1-x}Ga_xN$ alloy system a promising one for high efficiency light emitting diodes, laser diodes and solar cells. The performance of the devices depends upon the quality of the films. However, the growth of high quality InN and indium-rich $In_{1-x}Ga_xN$ has remained a challenge mainly due to low dissociation temperatures, high equilibrium vapor pressure of nitrogen and lack of lattice matched substrates. Improving the growth of high quality materials requires a better understanding of the growth mechanism which enables choosing the appropriate growth parameters such as temperature, reactor pressure, precursors ratio, precursors flow rate, and substrate. Furthermore, understanding the surface properties, reactions and thermal stability of the grown epilayers provides better choices in the growth conditions and techniques. The work described in this dissertation is part of an effort to gain a better understanding of the surface properties, growth reactions and thermal stability of InN and $In_{1-x}Ga_xN$ epilayers.

Developing detailed models of film growth requires detailed knowledge of surface properties such as structure, morphology and bonding configuration. To make heterostructure devices, layers of one material are grown on the surface of other materials. The growth rate and quality of the epilayers depend on a number of factors such as surface termination, defects and morphology. For example, the growth rate on the N-terminated surface is greater than that on In-

terminated surface and the growth rate is higher on a surface with fewer defects. In addition, the study of these properties provides a knowledge foundation for the design and production of device structures with predictable device properties.

During the metalorganic growth of InN films, surface reactions involving hydrogen are important steps. When a precursor such as trimethylindium (TMI) is decomposed during the growth of InN, surface hydrogen atoms are produced. These surface hydrogen atoms may reduce the number of available reaction sites for indium and nitrogen precursors affecting the quality and composition of the films. Surface hydrogen atoms produced by the decomposition of precursors during the growth are most frequently eliminated by desorption after reacting with adsorbed methyl groups or other hydrogen atoms. Therefore, understanding the mechanism and kinetics of hydrogen desorption is an important step in the growth mechanism. On the other hand, the study on the thermal stability of the epilayers is significantly important for a better understanding in the growth mechanism which provides information about the temperature up to which the epilayers are stable. Therefore, understanding the kinetics of hydrogen desorption and thermal stability of the epilayers provides limits for the growth window and informs choices regarding the growth conditions and techniques toward the growth of better quality epilayer.

2 GROUP III – NITRIDE SEMICONDUCTORS

2.1 Introduction

A III-nitride compound semiconductor is formed due the bonding of one of the group III elements such as, boron, aluminum, gallium or indium with the group V element, nitrogen. The III-nitrides and their alloys are direct band gap semiconductors. Their band gap varies from 0.7 eV for indium nitride (InN), 3.4 eV for gallium nitride (GaN), to 6.2 eV for aluminum nitride (AlN). Ternary III-nitride alloys like indium gallium nitride (InGaN), indium aluminum nitride (InAlN), and aluminum gallium nitride (AlGaN) offer the tunable band gap which covers the whole visible spectrum and into the deep ultraviolet (UV) region. So, III-nitride alloys are particularly suitable for applications in optoelectronic devices for solid state lighting, such as laser diodes (LDs) and light emitting diodes (LEDs). High electron mobility and saturation velocity, high breakdown field, and high thermal conductivity are advantages of III-nitrides especially for high-power, high-speed electronics. The developments in the field of III–nitride semiconductors have been spectacular due to their highly attractive inherent properties. The outstanding achievements in the development of blue/ultraviolet (UV) LEDs, LDs and high-frequency transistors operating at high powers and temperatures [1-3] have proved the remarkable advantages of III-nitride semiconductor systems. The wide band gap energy range also makes these materials good candidates for absorber layers in solar cells since the absorption edge of these materials can be varied to optimize cell efficiency. III- nitride based electronic devices are also more environmentally friendly because they do not contain toxic elements such as arsenic that are used to fabricate other compound semiconductors such as gallium arsenide (GaAs).

In the recent years, the III-nitrides based research has attracted remarkable attention and gained a significant position in the science and technology of compound semiconductors due to a great number of possible applications of III-nitride semiconductors. GaN and its alloy InGaN have become dominant materials for producing high brightness LEDs and LDs that emit light in the green/blue region of the visible spectrum. InGaN based light emitting diodes are already in use in full color liquid crystal diode (LCD) displays and traffic lights. All these applications demonstrate the technological relevance of the III-nitride compounds and the reason for these materials to be the subject of an active research field.

2.2 Properties

The binary group III-nitrides AlN, GaN and InN can crystallize in three structural phases; (a) wurtzite, (b) zincblende and (c) rock-salt (NaCl). However, wurtzite structure is the thermodynamically stable phase at ambient conditions [4-6]. The zincblende structure is metastable and can be stabilized by heteroepitaxial thin film growth on the (001) crystal planes of cubic structures such as Si, MgO and GaAs [7]. A phase transition to the rock-salt structure takes place at high pressure [7]. The wurtzite and zincblende structures are similar in many aspects. In both cases, the group III element is surrounded by four atoms of the group V element, which are arranged at the edges of a tetrahedron. Likewise, the group V element is surrounded by four atoms of group III elements. Also, the twelve next-nearest neighbors are at the equal distance in both structures. The main difference between wurtzite and zincblende structure is found only from the third next nearest neighbors, that is, they have different stacking sequences. The stacking sequence of the wurtzite structure along [0001] is ABAB, while that of zincblende structure along [001] direction is ABCABC, where A, B, and C refer to allowed sites of the III-N

pairs of the closed-packed layers. A fault in stacking sequence may transform one structure into another or create a structural defect. The wurtzite structure can be transformed into the rock-salt structure at high pressures. In this transformation, the bond character changes mostly from covalent to ionic and from four to six fold coordination of atoms. The structural phase transition was experimentally observed at pressures of 22.9 GPa, 52.2 GPa and 12.1 GPa for AlN, GaN and InN, respectively [8-10].

As mentioned above, the III-nitride semiconductors and their alloys are direct band gap semiconductors. The band gap energy of a semiconductor is an important parameter that determines its transport and optical properties as well as many other phenomena. The major technological advantage of the III-nitride system is that by alloying GaN with InN and/or AlN the band gap can be tuned in a controllable fashion covering a wide spectral range from deep UV (AlN = 6.2 eV) to near IR (InN = 0.7 eV). So, ternary and quaternary alloy systems of AlN, GaN and InN (such as InGaN, InAlN, AlGaN, and AlGAInN) can have continuous band gap energy from 0.7 eV to 6.2 eV depending upon the composition of In or Ga or Al in the alloy system.

A unique characteristic inherent in III-nitrides is the strong polarization [11, 12]. Due to the lack of a center of symmetry and the large ionicity of the metal-nitrogen bonds, spontaneous polarization is present along the c-axis in the wurtzite structure of the III-nitride materials. Also, the introduction of an external strain on this structure produces piezoelectric polarization. So, the net polarization is composed of two parts: (1) spontaneous, which is inherent to the material and (2) strain-induced piezoelectricity; both are influenced by the polarity of the III-nitride. Spontaneous and piezoelectric polarizations present in wurtzite III-nitrides influence the optical and electrical properties of the material.

The chemical bonding within III-nitrides is very strong. Due to this strong chemical bonding, III-nitride semiconductors have a high melting point, mechanical strength and chemical stability. In addition, their strong bonding makes them resistant to high-current electrical degradation and radiation damage that is present in the active regions of light emitting devices [13]. These materials also possess good thermal conductivity. III-nitride based devices can operate at high temperatures as well as in hostile environments.

The performance and efficiency of III-nitrides based electronic devices depend upon the electronic properties, particularly carrier concentration and mobility. A range of values of electron mobility and background concentration have been measured for AlN, GaN, and InN by using Hall measurements. Carrier mobility depends upon various factors such as temperature, electric field, doping concentration and material quality of the semiconductors. If the lattice mismatch is large then the value of carrier mobility is low. Using a buffer layer during the nucleation reduces the strain which enhances the carrier mobility.

The optical properties of the III-nitride based devices depend upon some important factors such as refractive index and dielectric constant of the materials. Some important structural, electronic, thermal and optical properties of wurtzite AlN, GaN and InN are listed in Table 2.1.

Table 2.1 Properties of wurtzite III-nitride materials.[7, 14-21]

Property	AlN	GaN	InN
Thermal expansion coefficient (300K)			
a ($\times 10^{-6}$ K^{-1})	4.2	5.59	5.7
c ($\times 10^{-6}$ K^{-1})	5.3	3.17	3.7
Thermal conductivity ($Wcm^{-1}K^{-1}$)	2.0	1.3	0.8
Melting point (°C)	>3000	>2500	>1100
Bulk modulus (GPa) (300K)	210	210 ± 10	140
Refractive index	2.2	2.35	2.56
Bond length (Å)	1.89	1.94	2.15
Cohesive energy per bond (eV)	2.88	2.24	1.93
Lattice constant (Å)	$^{a}3.11$, $^{c}4.97$	$^{a}3.18$, $^{c}5.18$	$^{a}3.54$, $^{c}5.70$
Energy gap (eV)	6.2	3.39	0.7
Effective electron mass (m_o)	0.48	0.2	0.06
Electron mobility ($cm^2V^{-1}s^{-1}$)	300(Theo.)	1000 (Theo.)	14000(Theo.)
	426 (Expt.)	900(Expt.)	3980(Expt.)
Peak drift velocity ($\times 10^7$ cm s^{-1})	0.02	3.1	4.3
Electron concentration (cm^{-3})	$<10^{16}$	$\sim 10^{17}$	$>10^{19}$
Dielectric constant	$\varepsilon_0 = 8.5 \pm 0.2$	$\varepsilon_0 = 10.0$	$\varepsilon_0 = 15.3$
	$\varepsilon_\infty = 4.68$-$4.84$	$\varepsilon_\infty = 5.5$	$\varepsilon_\infty = 8.4$

2.3 InN

2.3.1 Introduction

Among the III-nitride semiconductors (InN, AlN and GaN), InN has been the least studied semiconductor. The main reasons for paying less attention to the study of InN than that of GaN and AlN are as follows. First, the growth of high quality single crystalline InN is a challenge mainly due to the low dissociation temperature of InN and high equilibrium vapor pressure of nitrogen over InN. One of the ways to avoid thermal dissociation is to grow InN epilayers at low temperatures. However, at low temperature, the cracking efficiency of ammonia (NH_3) precursor is extremely low. Second, there exist alternative, well characterized semiconductors such as GaAs and AlGaAs, which have energy band gaps close to 1.89 eV, the band gap previously associated with InN. However, in recent years, the number of publications concerning InN research has increased remarkably since there have been significant improvements in the growth of InN films.

The first attempt to synthesize InN was made by Juza and Hahn in 1938 [22]. They obtained InN from $InF_6(NH_4)_3$ and reported the crystal structure of InN to be wurtzite. After that, several attempts were made to synthesize InN by Juza and Rabenua in 1956 [23], Renner in 1958 [24], Pastrnak and Souckova in 1963 [25], and Samsonov in 1969 [26]. It was pointed out that direct interaction of metallic indium and nitrogen in an inactivated form does not take place even at rather high temperatures [27]. McChesney *et al.* reported that the dissociation pressure of InN is extremely high and InN is not formed by direct reaction of N_2 molecules and indium [28]. In all of the above methods, interaction of indium compound with ammonia or thermal decomposition of the complex compound containing In and N was used, and the prepared InN was in the form of powder or small crystals. The earliest success in the growth of InN with some

good electrical properties was obtained by Hovel and Cuomo in 1972 [29]. A number of investigations were carried out to characterize the fundamental properties of InN. However, there were wide variations in the reported values of fundamental parameters, including the band gap, lattice constants, electron effective mass, and electron mobility. After realization of the commercial importance of the InGaN alloy system, growth of good quality InN was pursued by several groups but was not successful until the late 1980s.

In the recent years, there have been significant improvements in the growth of InN films. High quality single crystalline InN film with two-dimensional growth and high growth rate are now routinely obtained. The background carrier concentration and Hall mobility have also improved. A major breakthrough in InN research occurred few years ago, when the growth of good quality single crystalline films of InN on sapphire substrate by molecular beam epitaxy (MBE) was reported [30-32] and the band gap energy was claimed to be 0.67 ± 0.05 eV [30,33,34]. With the discovery of this low band gap energy value of InN, the research interest in the study of InN has increased dramatically. Both theoretical calculations and experimental results have shown that InN has some remarkable material properties such as low electron effective mass, high electron mobility, high peak and saturation velocity and a small direct band gap [33].

InN is considered to be a very attractive material for future photonic and electronic devices, such as high speed field-effect transistors, terahertz emitters, and high efficiency solar cells, owing to its outstanding material properties like smallest effective mass, largest mobility, highest peak and saturation velocities, and smallest direct band gap energy among nitride semiconductors. The higher refractive index of InN compared to GaN and AlN is one of the important aspects of using this material for photonic band edge design [35]. The use of InN-

based optoelectronic devices offers the potential of an environmentally friendly red emitter with no toxic elements to replace GaAs-based devices. InN is also a potential material for transparent conducting window material for heterojunction tandem solar cells [36]. InN has a stronger surface charge accumulation than InAs [37]. The accumulated electrons, which largely stay within 4 nm from the top InN surface, contribute considerably to the lateral conductivity of thin InN films [38]. If this surface charge is sensitive to environment and can be modulated by external treatments, InN could be a sensitive surface-sensing material. InN and In-rich nitrides have shown radiation hardness as measured by photoluminescence and will be useful for a wide range of sensing units operating in a high radiation environment [39]. Lu *et al.* [40] studied the electrical response of InN surface to chemical exposure and demonstrated that InN surface shows a fast response to certain solvent exposures with a large increase in surface carrier density. This increase in surface charge is accompanied by an enhancement of an average Hall mobility and both decay gradually. Similarly, by performing Monte Carlo simulations it has been shown that InN is promising material for an emitter in the THz frequency range [41-44]. Other potential applications of InN are in fabrication of metal-semiconductor field effect transistor (MISFET) devices [45], anodes for Lithium - ion thin film batteries [46], and thermoelectric devices [47, 48].

2.3.2 Growth

As discussed before, the growth of InN is the most difficult among the III-nitride semiconductors because the equilibrium vapor pressure of nitrogen over the InN is several orders higher than that of AlN and GaN [49]. Due to the low InN dissociation temperature and high equilibrium nitrogen vapor pressure over the InN film, the preparation of InN requires a low

growth temperature. Therefore, the current growth methods for InN and indium rich group III-nitride materials have been dominated by low temperature growth techniques such as, molecular beam epitaxy (MBE), metal organic chemical vapor deposition (MOCVD), hydride vapor phase epitaxy (HVPE), and atomic layer deposition (ALD). The important growth techniques which are aimed to the growth of high quality InN and in-rich group III-nitrides are discussed below.

2.3.2.1 Metal organic chemical vapor deposition

Metal organic chemical vapor deposition (MOCVD), also known as metal organic vapor phase epitaxy (MOVPE), is an arranged chemical vapor deposition method. In this technique, the crystals are grown by chemical reaction and not physical deposition. As of today, this technique is preferred for the formation of devices incorporating thermodynamically metastable alloys, and it has become one of the major processes in the manufacture of optoelectronic devices. For MOCVD growth of InN, trimethylindium (TMI) and ammonia (NH_3) are used as an indium source and a nitrogen source respectively. Nitrogen (N_2) and Hydrogen (H_2) are being used as carrier gas. Due to the low (~ 500 ºC) growth temperature, the MOCVD growth of InN is thought to be restricted by a low decomposition rate of NH_3. Although a higher growth temperature is expected to result in a higher decomposition rate of NH_3, it can also bring about thermal decomposition or thermal etching of the grown InN. On the other hand, growth at a low temperature (<400 ºC) is dominated by the formation of metallic In droplets due to the shortage of reactive nitrogen [50]. Epitaxial growth at low temperature becomes impossible due to reduced migration of the deposited materials. Therefore, the region suitable for the deposition of InN is very narrow. Experimental results show that enhancement of NH_3 decomposition, by increasing growth temperature, group V/III precursor ratio and growth pressure, favors the

MOCVD growth of InN. Matsuoaka *et al.* reported that at a V/III ratio lower than 1.6×10^4, indium droplets formed on a surface [51]. The amount of indium droplets present was decreased with the increasing V/III ratio. At a ratio of more than 1.6×10^5, the indium peak in the XRD spectrum disappeared. The reason that a high input V/III ratio is required is to provide sufficient amount of reactive nitrogen, since the NH_3 decomposition rate is low at low growth temperature. However, in the case of a relatively high growth temperature (~650 ºC), the growth mechanism is different. Since NH_3 decomposition is highly enhanced at such a high temperature, a high input V/III ratio impedes the growth. In addition, enhancement of NH_3 decomposition results in an increase of H_2 partial pressure. Koukitu *et al*. [52] reported that an increase of hydrogen in the growth system resulted in a decrease of the InN deposition rate. Thus the reaction depositing InN proceeds more effectively in the inert gas system and is prevented with the increase of H_2. This is the reason that it is necessary to use an inert carrier gas in the growth of InN from indium containing nitrides. In the growth of InN by MOCVD, the most crucial parameter to control the film quality is the growth temperature. Growth temperature has a strong influence on the crystallinity, surface morphology, growth rate, electrical, and optical properties of the grown InN epilayers. Based on the overall quality of the grown InN film, the most suitable region for the MOCVD growth of InN is 500 – 650 ºC [50]. The growth rate is found to be dependent on the growth temperature. The growth rate increases with increasing growth temperature and TMI supply. Adachi et al. carried out a detailed study about the growth rate and its limiting parameters for MOCVD growth of InN [53]. They reported that the growth rate of InN increases with increasing temperature over the range 400 – 630 ºC even at a constant TMI supply, and showed a saturation against an increase in TMI supply, which indicates that the growth rate is limited by NH_3 decomposition at such temperatures. At 630 – 650 ºC, the growth rate is

proportional to TMI supply as NH_3 decomposition is highly enhanced and a growth rate as high as 0.8 microns per hour was attained at around 650 ºC. Above 650 ºC, the growth rate decreased with increasing temperature due to decomposition of InN, and In droplet formation dominated. However, according to Keller *et al.* [54] the growth rate drastically decreased with increasing the temperature above 620 °C. The variation of the temperature dependence in crystalline quality and growth rate found by different groups is likely due to differences in the temperature measurement methods and other parameters of the MOVPE growth system (e.g., horizontal or perpendicular reactor, growth pressure, gas velocity and flow system, susceptor structure, etc.). The growth temperature was also found to be a critical parameter for the electrical properties of the InN films. From both experimental and theoretical analysis it has been reported that the most suitable region of temperature for the MOCVD growth of InN is 550 – 650 ºC. In the MOCVD growth system, growth pressure is also one of the basic parameters. However, there are very few studies about the influence of growth pressure in the MOCVD growth of InN. It was reported that growth pressure significantly influences the grown InN film, especially the electrical properties. The crystalline quality of the InN film grown in low pressure was better than that grown in an atmospheric pressure at low growth temperature regime (~ 450 ºC) [55]. However, the electrical properties of the InN film grown at atmospheric pressure was found to be better than that for the film grown at low pressure, over a wide temperature range [56, 57].

2.3.2.2 Molecular beam epitaxy

Molecular beam epitaxy (MBE) is another technique used for the epitaxial growth of crystals. MBE growth is characterized by the interaction of a single or multiple molecular or atomic beams at the surface of a heated crystalline substrate. This interaction takes place in an

ultra-high vacuum chamber (~10^{-9} Torr). At this pressure the mean free path of a gas particle is approximately 40 km; therefore the gas molecules will collide with the chamber walls many times before colliding with each other. The low background pressure also provides the best available purity, because the arrival rates of contaminants are significant orders of magnitude less than typical chemical vapor deposition conditions. Unlike other deposition techniques, MBE growth is able to grow impurity-free, quality films with abrupt layers. For the growth of III-nitrides, the solid sources of the group III elements such as Ga, In, and Al are used. However, nitrogen is supplied by the gas source such as N_2 and NH_3. If the metalorganic chemical beams are used as the group III element sources, it is called metalorganic molecular beam epitaxy (MOMBE) or chemical beam epitaxy. In both cases, the key issue in the growth is the nitrogen source. Since the dissociation energy of N_2 molecules is as high as 9.5 eV, the supply of N_2 gas to the substrate surface with the group-III elemental beams cannot induce any growth of the nitrides. In order to get atomic reactive nitrogen, the N_2 molecules are dissociated by the radio-frequency (RF)-plasma or the electron cyclotron resonance (ECR). In RF plasma, effective generation of reactive nitrogen requires a small aperture size. In case of an ECR plasma source, the generation rate of reactive atomic nitrogen increases with increasing input microwave power. Therefore, nitrogen ions with energy higher than ~ 60 eV may induce defects in the epitaxial layer. Koukitu and Seki [58] reported a thermodynamic analysis on the MBE growth of III-nitrides. The chemical reaction, which connects all species at the substrate is,

$$In(g) + N(g) = InN(s). \quad (2.1)$$

In the case of NH_3, the reaction is

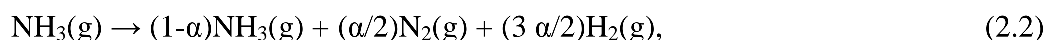

$$NH_3(g) \rightarrow (1-\alpha)NH_3(g) + (\alpha/2)N_2(g) + (3\,\alpha/2)H_2(g), \quad (2.2)$$

where α is the molar fraction of the decomposed NH_3.

Koukitu and Seki calculated the phase diagram during the deposition to find the suitable growth conditions for the MBE growth of III-nitrides. They reported that the growth temperature suitable for the growth of InN is 600 to 700 ºC with V/III ≥ 1. However, experimental growth temperature range is from 450 to 550 ºC which is much lower than that predicted theoretically.

The growth of good quality InN epilayers by MBE technique started in 2002. In this year, Davydov *et al.* [30] grew single crystalline hexagonal InN samples which had a band gap value of < 1.1 eV. Mamutin *et al.* [59] grew undoped InN layers on the c-plane sapphire substrates using ECR- plasma assisted MBE. Lu *et al.* [60] grew InN layers by rf-MBE technique which provided the band gap energy of < 1 eV. For the growth of InN layers in the MBE chamber, both groups used a turbo molecular pump to get the base pressure ~ 10^{-10} Torr. Metallic indium was supplied from an effusion cell. An ECR plasma source or EPI unibulk rf-plasma source was used for generating atomic reactive nitrogen with flow rates from 0.7 to 5 standard cubic centimeters per minute. During the growth, the nitrogen flux caused a nitrogen partial pressure of 1.8×10^{-5} Torr in the MBE chamber.

2.3.2.3 High pressure chemical vapor deposition

In MOCVD and MBE techniques, InN epilayers are grown under low pressure conditions. However, this is problematic because the decomposition temperature of InN is low and the equilibrium pressure of nitrogen rises rapidly with the increase of growth temperature [61].These problems of growth at low pressure create variations in the measured values of material properties due to point defect chemistry in InN which at present are not well understood [62]. In addition, the growth of III-nitride alloys at low pressure is a challenge due to the constraint that InN growth requires temperatures < 600 ºC while good quality GaN and AlN

growth requires temperatures > 1000 ºC. It is reported that InN can be grown at much higher temperature if stabilized at high nitrogen pressures [63]. Motivated by this, a novel high pressure chemical vapor deposition (HPCVD) system has been developed in Dr. Dietz's research lab at Georgia State University, Atlanta, USA. This system allows the control of vastly different partial pressures of constituents involved in the growth of InN and indium-rich group III-nitride alloys [64-69]. The HPCVD reactor system utilizes the pulsed precursor injection technique, which is essential in order to achieve compression of the precursors to reactor pressure, minimization of gas phase reactions, optimization of nucleation kinetics and analysis of gas phase and surface decomposition dynamics in real-time. The details of the design of HPCVD reactor system, growth procedure and real time optical characterization of InN growth can be found in Mustafa Alevli's dissertation [70].

2.3.2.4 Hydride vapor phase epitaxy

Hydride vapor phase epitaxy (HVPE) was demonstrated as the first epitaxial growth of InN [71]. This growth technique has received much attention due to its capability of high growth rate compared with that of MOCVD and MBE growth techniques. HVPE method has been used to deposit single crystal layers of both GaN and AlN for over 3 decades. The HVPE process is a chemical vapor deposition method, which is usually carried out in a hot wall reactor (horizontal or vertical) at atmospheric pressure. For the growth of InN, the source materials are indium monochloride (InCl) or indium trichloride ($InCl_3$) as In source and NH_3 or monomethylhydrazine (MMHy) as N source. A higher growth rate was observed using the $InCl_3$-NH_3 material source system as compared to the InCl-NH_3 material source system. Due to the slow progress and technical challenges in growing bulk layers via MOCVD and MBE, the HVPE method has been

a pathway to produce substrate materials of group III-nitride semiconductors. Free standing GaN wafers with an electron mobility of 1320 cm^2/Vs and a donor concentration of 7.8×10^{15} cm^{-3} have been grown by this method [72, 33]. It is reported that the dislocation density in GaN layers decreases with an increase in layer thickness [73]. So, HVPE is an attractive method for the growth of quasibulk materials, which can provide lattice matched growth surfaces and thick, strain relieved buffer layers. The growth of InN epilayers has been attempted on a GaN buffer layer using $InCl_3$-NH_3 source system at growth temperatures as high as 750 ºC [74]. It is reported that the growth rate decreases with the increase of growth temperature and for the growth of InN at high temperature, a high input partial pressure of $InCl_3$ is required.

2.3.2.5 Atomic layer deposition

Atomic layer deposition (ALD) was originally developed for fabrication of polycrystalline luminescent ZnS:Mn and amorphous Al_2O_3 insulator films for electroluminescent flat panel displays, and the method itself was termed atomic layer epitaxy (ALE) [75]. The early ALE literature dealt with polycrystalline II–VI compounds and amorphous oxide films [76]. Since 1985, epitaxial growth of III–V and II–VI compounds gained much interest [77–79], but no real breakthrough was achieved in this area due to the complicated surface chemistry. Since the mid 1990s, rapidly increasing interest towards ALD has originated from the silicon based microelectronics. This increase is a consequence of the ever decreasing device dimensions and increasing aspect ratios in integrated circuits (IC). The ALD method relies on alternate pulsing of the precursor gases and vapors onto the substrate surface and subsequent chemisorption or surface reaction of the precursors [80]. The reactor is purged with an inert gas between the precursor pulses. With a proper adjustment of the experimental conditions the process proceeds

via saturative steps. Under such conditions the growth is stable and the thickness increase is constant in each deposition cycle. The self-limiting growth mechanism facilitates the growth of conformal thin films with accurate thickness on large areas [81]. The growth of different multilayer structures is also straightforward [82]. These advantages make the ALD method attractive for microelectronics for manufacturing of future generation integrated circuits [83]. Just like MOCVD, ALD processes may also be performed in many kinds of reactors over a wide pressure range. The characteristic feature of ALD, the use of sequential saturated surface reactions, gives rise to inherent surface control characteristics in ALD processing. Instead of being a source- or material flux-controlled method of material deposition, ALD can be classified as a surface-controlled method of growing material. Accordingly, the rate of growth in ALD is proportional to the repetition rate of the reaction sequences rather than to the flux of reactant. Any MBE or CVD system can be used in ALD mode provided that there are means for switching the fluxes of the reactants. In MBE systems, the switching is generally made by using shutters for internal heated sources. In CVD systems, all the reactants are normally volatile gases and can be switched by gas valving. The characteristic feature of ALD is that each reaction sequence is fed to a saturated surface condition on the substrate, which means that the substrate temperature and the vapor pressures of the reactants as well as the reaction products must fulfill the saturation requirements. The ALD method has already shown its versatility in industrial use for deposition of dielectric and luminescent films for electroluminescent flat panel displays. This technique has great potential because of the accurate thickness control in deposition of very thin films and 100% conformality. However, the major limitation of ALD is evidently its slower deposition rate.

The samples studied in this work were grown by two techniques (1) HPCVD in Dr. Dietz's lab at Georgia State University, Atlanta, USA and (2) plasma-assisted ALD in Dr. Eddy's lab at Naval Research Laboratory, Washington D. C.

2.3.3 Structural properties

The quality and performance of the InN based device structures are dependent on the crystal structure. Single crystal group III nitride semiconductors AlN, GaN and InN crystallize in three structures: wurtzite (hexagonal), zincblende (cubic) and rock salt. The hexagonal wurtzite structure of InN is the thermodynamically stable phase in contrast to cubic III-V semiconductors such as GaAs and InP which possess zincblende structure [84]. Juza and Hahn first reported the crystalline structure of InN to be wurtzite having lattice parameter a = 3.53 Å and c = 5.69 Å [85]. However, Tansley and Foley measured lattice parameter a = 3.548 Å and c = 5.760 Å for rf – sputtered InN film [86]. Davydov *et al.* reported the lattice parameter a = 3.536 Å and c = 5.7039 Å in the high quality hexagonal InN film [30]. A comparison of lattice parameters for polycrystalline and single crystalline InN reported by some authors shows that the variation in a-lattice parameter is very little and all the values are quite close and are in good agreement with the theoretical values scattered in the range of a = 3.501 – 3.536 Å. The experimental c-lattice parameter scattered in the range of c = 5.690 – 5.705 Å and the theoretical reported values scattered in the range of c = 5.540 – 5.709 Å. It is suggested that the possible reasons for the variation in experimental values are crystalline quality and incorporation of oxygen contamination [87].

There are several techniques to characterize the crystal structure. However, x-ray diffraction (XRD) is the most versatile and non destructive technique used for the

characterization of crystal structure. This technique divulges detailed information about the crystallographic structure as well as the chemical composition of any natural and manufactured materials. In order to investigate the microstructure of InN films such as dislocations and grain boundaries, transmission electron microscopy (TEM) is generally used. Rutherford back scattering spectroscopy (RBS) measurements are usually performed to assess the film stoichiometry. These techniques are commonly used to study the bulk crystal structure. However, to analyze the crystal structure of the surface, the low energy electron diffraction (LEED) technique is used. Details of this technique are presented in chapter three.

2.3.4 Electrical properties

With no intentional doping, as grown InN is always an n-type with a very high background carrier concentration. There has been much speculation as to what species is responsible for high background donor concentration in the grown InN. Both theoretical calculations and experimental results give conflicting views regarding the major reason responsible for such high n-type conductivity. The potential candidates for such high background donors are native defects, such as N vacancy, nitrogen antisite, oxygen impurities and possibly interstitial H [50]. According to Tansley and Foley, the n-type behavior is caused by an antisite defect: N on an In site (N_{In}), which they had suggested might be a double donor [88]. Another defect possibly responsible for the n-type character of InN is oxygen on an N site, which is not a native defect, but is likely to be present in significant concentration. It is most likely that every nitrogen vacancy donates a single donor but possibly donates three electrons to the conduction band [89]. The donor nature of the N vacancy is constructed as a missing N atom surrounded by four In atoms that provide three valence electrons to complete the bonding octet with the five

missing electrons of nitrogen. Two of these three electrons would be donated to the conduction band. Therefore, it has been believed that nitrogen vacancy is the dominant donor in the as-grown InN film.

Until the 1980s, most of the InN films were deposited using sputtering. The grown films were polycrystalline with a carrier concentration in the range of 10^{18} to 10^{21} cm^{-3} and Hall mobility from 20 to 250 cm^2/Vs. However, Tansley and Foley reported the carrier concentration in the range of 10^{16} cm^{-3} and carrier mobility as high as 2700 cm^2/Vs at room temperature [90]. Sato achieved a carrier density of 4×10^{19} cm^{-3} in the InN epitaxial layer grown on sapphire substrate by plasma assisted MOVPE in 1997 [91]. Yamaguchi *et al.* showed that selection of GaN for the underlying layer and increased InN film thickness significantly improve the Hall mobility. A Hall mobility of about 700 cm^2/Vs was obtained in the InN film grown on GaN even at an electron concentration of 5×10^{19} cm^{-3} [92]. Yamamoto *et al.* [56, 57, 93] showed a high NH_3/TMI molar ratio and enhanced NH_3 decomposition significantly improved the electrical properties of MOVPE grown InN film. As a result, a carrier concentration on the order of 10^{18} cm^{-3} and electron mobility of 730 cm^2/Vs were obtained. For HVPE-grown InN on GaN template, Lu *et al*. have achieved a carrier concentration in the order of 10^{17} cm^{-3} and a mobility of more than 2000 cm^2/Vs [94]. The carrier concentration and electron mobility in the InN film grown by migration enhanced epitaxy (MEE) were found to be 3×10^{18} cm^{-3} and 542 cm^2/Vs respectively. It is also reported that for both MEE and MBE growth methods, Hall mobility increases with the film thickness [95]. The use of a buffer layer of AlN, GaN or InN seems to contribute to the improved structural and electrical properties of MBE grown InN. The better electrical properties in the MBE InN films compared with MOVPE are believed to be due to the

ability to supply active nitrogen independent of the growth temperature and reduced impurity incorporation in the MBE growth.

2.3.5 Optical properties

There is a huge conflict about one of the basic physical properties of InN, the optical band gap energy. The band gap energy of InN reported by Tansley and Foley was ~ 1.9 eV [86] which was the most commonly accepted value until 2002. But various measurements such as, optical absorption, photoluminescence (PL) and photomodulated reflection (PR) resulted the band gap of MBE-grown InN to be 0.67± 0.05 eV [30, 33, and 34]. However, Shubina *et al.* [96] commented on this interpretation of optical absorption and photoluminescence data for the band gap of InN. They claimed that the band gap of InN is much wider than this newly accepted value. According to their report, the lower absorption edge is due to Mie scattering by metallic indium clusters and the PL peak at 0.7 eV in InN originates from optical transitions involving interface states between the indium clusters and the indium nitride matrix. Inushima *et al.* insisted that the fundamental absorption edge of MBE grown InN layer lies around 1.1 eV, which is much lower than the previously reported values [97]. Davydov *et al.* reported a band gap value of 0.9 eV for high quality MBE grown InN, studied by means of optical absorption, PL, photoluminescence excitation (PLE) spectroscopy, as well as by *ab initio* calculation [30]. Analysis of optical absorption, PL, PLE, and photoreflectivity data obtained on single crystalline hexagonal InN film leads to the conclusion that the true band gap of InN is E_g ~ 0.7 eV [98, 99]. However, to settle the band gap value of InN, growth of more high quality InN film and further studies on the measurement of optical properties are required.

2.3.6 Polarity

In group III-nitride semiconductors, either group III or N atoms can occupy the first atomic layer, i.e., the grown III-nitrides have a polar configuration. Generally, group III terminated plane is denoted as (0001) and group V terminated plane is denoted as ($000\bar{1}$). In other words, if three of the bonds of a tetrahedrally coordinated III atom point towards substrate, i.e., opposite of the growth direction, the film has metal-polarity. But if three bonds point away from the substrate or along the growth direction, the film is N-polar. The wurtzite crystal structure of a) N-polar and b) In-polar InN films are depicted in Fig. 2.1 [100]. Investigation has revealed that these two polar films have vastly different growth and surface structure properties. In addition, the film polarity has significant effects on the electrical and optical properties of the film [50]. Other properties of the material such as etching, defect generation and plasticity, and piezoelectricity also depend on its polarity. Therefore, it is very important to determine the polarity in the characterization of nitride semiconductors. There are various methods used in the determination of polarity of InN. One of the common and easy methods is the wet etching of the crystal by KOH or NaOH solution. However, this method is destructive since the sample cannot be used again once it is etched. The non-destructive methods are convergent beam electron diffraction (CBED), coaxial impact collision ion scattering spectroscopy (CAICISS) and high resolution electron energy loss spectroscopy (HREELS). HREELS is a non-destructive technique to determine the polarity of InN film. Details of the determination of polarity of InN film using HREELS have been presented in Rudra Bhatta's dissertation [101]. From study of GaN it is found that the polarity of the layer is a key parameter for obtaining smooth and low defect density film. In general, the N-terminated GaN epilayers are found to show a rough surface morphology consisting of grains and extended defects. In contrast, Ga-terminated GaN film has

an atomically flat surface [102]. However, Wang and Yoshikawa [103] reported that the surface morphology and the crystalline quality of N-polar InN are better than that of In-polar InN. They also reported that the electrical properties of N-polar InN films are better than those of In-polar films. The room temperature mobilities of N-polar InN films were 500-1500 cm^2/Vs with electron concentrations of (1-10) $\times 10^{18}$ cm^{-3} while the mobilities of In-polar InN films were 300-900 cm^2/Vs with electron concentrations of (4 -10) $\times 10^{18}$ cm^{-3}. Other properties such as stability are also affected by the polarity of InN. Naoi *et al.* have reported that the In-polar surface is chemically more stable whereas the N-polar surface is thermally more stable [104]. It is found that the substrate surface and its treatment such as nitridation, buffer layer material and growth condition such as V/III ratio are very important to control the polarity of the grown film. Wang and Yoshikawa [103] reported that the polarity of InN film depends on the polarity of the materials in the buffer layer. InN films grown on N-polar GaN or AlN buffer layers were N-polar and that grown on Ga-polar or Al-polar buffer layers were In-polar. Whereas, when grown on a sapphire substrate with an InN buffer layer, N-polar InN is generally obtained due to nitridation of the sapphire substrate before the deposition of InN. Saito *et al.* evaluated the polarity of single-crystalline InN using CAICISS [105]. They found that the polarity of the rf-MBE grown InN on sapphire is very sensitive to the growth temperature. Low temperature (~ 300 ºC) grown InN was found to be mainly N-polarity, high temperature (~ 550 ºC) grown InN was found to be mainly In-polarity, and two-step grown InN was found to be a mixture of In-polarity and N-polarity.

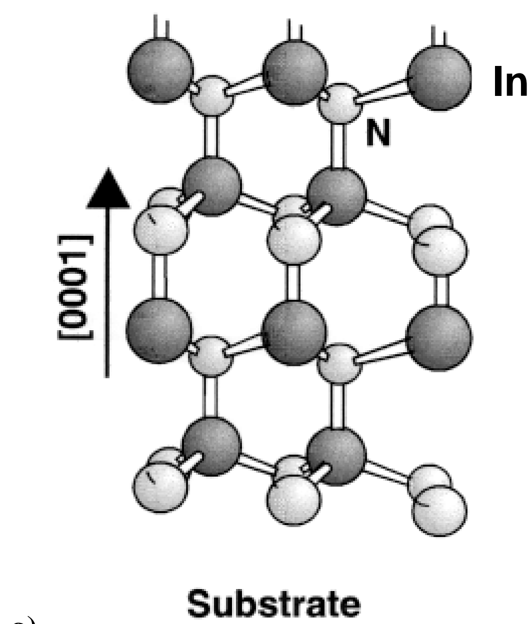

a)

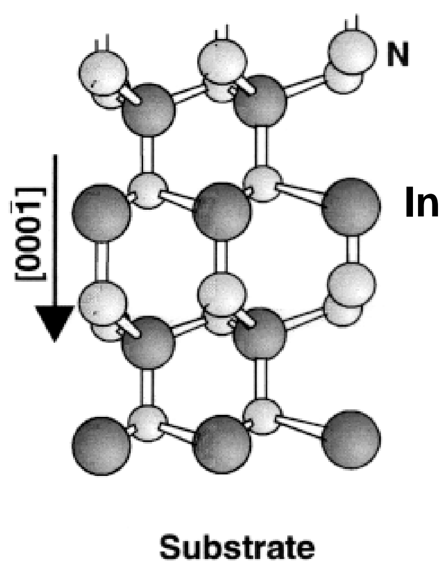

b)

Figure 2.1 Wurtzite crystal structures of a) In-polar InN and b) N-polar InN [3].

2.3.7 Desorption of hydrogen

Study of the stability of hydrogen bonding with surface atoms of nitride semiconductors like InN, GaN, and their alloys is of great interest because understanding the mechanisms and kinetics of hydrogen desorption is important for developing both qualitative and quantitative models of the growth of III-nitride semiconductors like GaN and InN or their alloys. For instance, if the growth temperature is lower than the hydrogen desorption temperature, sites on the III-nitride growth surface could be occupied by hydrogen, which is produced during the precursors decomposition process. This may reduce the number of reaction sites available for adsorption of precursors and could affect the growth rate and quality of the film. On the other hand, it is also reported that presence of hydrogen on the surface during the growth prevents the incorporation of impurities, particularly carbon and oxygen, into the film and enhances the growth. Since the presence of hydrogen stabilizes the semiconductor surfaces against surface reconstructions, the study of interaction of hydrogen with semiconductor surfaces is of great interest. The surface structure of the nitride semiconductors can be changed by the adsorption or desorption of any molecular species. Removal of adsorbates from the surface, such as hydrogen, leaves surface dangling bonds. This may cause surface reconstruction depending upon the proximity of neighboring atoms and energy considerations. Using first principle calculations, Rapcewizz *et al*. [106] reported that adsorption of three fourths of a monolayer of hydrogen stabilizes GaN surfaces of both polarities and results in 2×2 symmetry. However, Elsner *et al.* [107] calculated that three fourths monolayer hydrogen coverage results in a [1×1] periodicity for both polarities of GaN. Using electron energy loss spectroscopy (EELS) and photoelectron spectroscopy, Bermudez *et al.* [108] showed that adsorption of hydrogen affects electronic properties of GaN surfaces. However, such studies have not been done on InN surfaces yet.

Investigation of thermal kinetic parameters of hydrogen from InN surfaces, such as activation energy, is very important to understand the growth mechanism, particularly the growth temperature. Eventually, this helps grow better quality film and hence better performing devices.

2.4 References

[1] S. Strite and H. Morkoc, J. Vac. Sci. Technol. B **10**, 1237 (1992).

[2] S. N. Mohammad and H. Morkoc, Prog. Quantum Electron. **20**, 361 (1996).

[3] O. Ambacher, J. Phys. D: Appl. Phys. **31**, 2653 (1998).

[4] I. Akasaki, H. Amano, in Group III nitrides, ed J. H. Edgar, INSPEC, UK, pp. 30-34 (1994).

[5] W. J. Meng, in Group III nitrides, ed J. H. Edgar, INSPEC, UK pp.22-29 (1994).

[6] T. L. Tansley, in Group III nitrides, ed J. H. Edgar, INSPEC, UK pp.35-42 (1994).

[7] B. Gil, Group III nitride semiconductor compounds Physics and applications; Clarendon Press, Oxford (1998).

[8] P. Perlin, C. Jauberthiecarillon, J. P. Itie, A. S. Miguel, I. Grzegory, A. Polian, Phys. Rev.B **45**, 83 (1992).

[9] M. Ueno, M. Yoshida, A. Onodera, O. Shimomura, K. Takemura, Phys. Rev. B **49**, 14 (1994).

[10] Q. Xia, H. Xia, A. L. Ruoff, J. Appl. Phys. **73**, 8198 (1993).

[11] F. Bernardini and V. Fiorentini, Phys. Stat. Sol.b **216**, 391 (1999).

[12] F. Bernardini and V. Fiorentini, Phys. Rev. b **64**, 085207 (2001).

[13] F. A. Ponce, and D. P. Bour, Nature **386**, 351 (1997).

[14] F. A. Ponce, Introduction to Nitride Semiconductor Blue Lasers and Light Emitting Diodes, Ed. by S. Nakamura and S. Chichibu (Taylor and Francis, Ltd., London, 2000), Chapter 4.

[15] I. Vurgaftman and J. R. Meyer, J. Appl. Phys. **94**, 3675 (2003).

[16] V. M. Polyakov and F. Schweirz, Appl. Phys. Lett. **88**, 032101 (2006).

[17] S. N. Mohammad, H. Morkoc, Prog. Quant. Electr. **20**, 361 (1996).

[18] K. Matsubara, T. Takagi, Jpn. J. Appl. Phys. **22**, 511 (1982).

[19] A. S. Barker, M. Illegems, Phys. Rev. B **7**, 743 (1973).

[20] F. Bechstedt, B. Gil (Ed.), Low Dimensional Nitride Semiconductors, Oxford University Press, P.11 (2002).

[21] F. Bernadini, V. Fiorentini, D. Vanderbilt, Phys. Rev. Lett. **79**, 3958 (1997).

[22] R. Juza and H. Hahn, Z. Anorg. Allg. Chem. **239**, 282 (1938).

[23] R. Juza and A. Rabenau, Z. Anorg. Allg. Chem. **285**, 212 (1956).

[24] T. Renner, Z. Anorg. Allg. Chem. **298**, 28 (1958).

[25] J. Pastrnak and L. Souckova, Phys. Status Solidi 3, K71 (1963).

[26] G. V. Samsonov, Nitridy Kiev, 1969.

[27] N. A. Gorjunova, Slosnye Almazopodobnye Poluprovodniki, Moscow (1964).

[28] J. B. McChesney, P. M. Bridenbaugh, and P. B. O'Connor, Mater. Res. Bull. **5**, 783 (1970).

[29] H. J. Hovel and J. J. Cuomo, Appl. Phys. Lett. **20**, 71 (1972).

[30] V. Y. Davydov, A. A. Klochikhin, R. P. Seisyan, V. V. Emtsev, S. V. Ivanov, F. Bechstedt, J. Furthmuller, H. Harima, V. Mudryi, J. Aderhold, O. Semchinova, J. Graul, Phys. Stat. Sol. (b) **229**, R1 (2002).

[31] H. Lu, W.J. Schaff, J. Hwang, H. Wu, W. Yeo, A. Pharkya, L.F. Eastman, Appl. Phys. Lett. **77**, 2548 (2000).

[32] Y. Saito, T. Yamaguchi, H. Kanazawa, K. Kano, T. Araki, Y. Nanishi, N. Teraguchi, A. Suzuki, J. Cryst. Growth **237**, 1017 (2002).

[33] Y. Nanishi, Y. Saito, T. Yamaguchi, Japanese Journal of Applied Physics Part 1-Regular Papers Short Notes & Review Papers **42**, 2549 (2003).

[34] J. Wu, W. Walukiewicz, K. M. Yu, J. W. Ager, E. E. Haller, H. Lu, W.J. Schaff, Y. Saito, Y. Nanishi, Appl. Phys. Lett. **80**, 3967 (2002).

[35] M. Leroux, B. Gil, J.H. Edgar, S. Strite, I. Akasaki, H. Amano, C. Wetzel, Gallium nitride and related semiconductors, Publ. INSPEC (1999).

[36] A. Yamamoto, M. Tsujino, M. Ohkubo, A. Hashimoto, Sol. Energy Mater. Sol. Cells 35 (1994).

[37] I. Mahboob, T. D. Veal, C. F. McConville, H. Lu, and W. J. Schaff, Phys. Rev. Lett. **92**, 036804 (2004).

[38] I. Mahboob, T. D. Veal, L. F. J. Piper, C. F. McConville, H. Lu, W. J. Schaff, J. Furthmüller, and F. Bechstedt, Phys. Rev. B **69**, 201307 (2004).

[39] J. Wu et al., J. Appl. Phys. **94**, 6477 (2003).

[40] H. Lu, W. J. Schaff, L. F. Eastman, J. Appl. Phys. 96 (2004) 3577.

[41] R. Brazis, R. Raguotis, P. Moreau, M. R. Siegrist, Int. J. Infrared Millimeter Waves **21**, 593 (2000).

[42] P. Shiktorov, E. Starikov, V. Gruzinskis, M. Zarcone, D. P. Adorno, G. Ferrante, L. Reggiani, L. Varani, J. C. Vaissiere, Phys. Stat. Sol. (a) - Applied Research **190** , 271 (2002).

[43] E. Starikov, P. Shiktorov, V. Gruzinskis, L. Reggiani, L. Varani, J. C. Vaissiere, J. H. Zhao, Journal of Physics-Condensed Matter **13**, 7159 (2001).

[44] E. Starikov, P. Shiktorov, V. Gruzinskis, L. Reggiani, L. Varani, J. C. Vaissiere, J. H. Zhao, Physica B-Condensed Matter **314**, 171 (2002).

[45] H. Lu, W. J. Schaff, L. F. Eastman, Mater. Res. Soc. Sympo. Proc. 693 (2002).

[46] B. J. Neudecker, R. A. Zuhr, Electrochem. Soc. Proc. **99**, 295 (2000).

[47] S. Yamaguchi, R. Izaki, N. Kaiwa, S. Sugimura, A. Yamamoto, Appl. Phys. Lett. **84**, 5344 (2004).

[48] S. Yamaguchi, R. Izaki, K. Yamagiwa, K. Taki, Y. Iwamura, A. Yamamoto, Appl. Phys. Lett. **83**, 5398 (2003).

[49] O. Ambacher, M. S. Brandt, R. Dimitrow, T. Metzger, M .Stutzmann, R. A. Fischer, A. Miehr, A. Bergmajer, and G. Dollinger, J. Vac . Sci. Technol. B **14**, 3532 (1996).

[50] A. G. Bhuiyan, A. Hashimoto, and A. Yamamoto, J. Appl. Phys., **94**, 2779 (2003).

[51] T. Matsuoka, in GaN and Related Materials, edited by S. J. Pearton, pp. 53–59 (Gordon and Breach, New York, 1997).

[52] A. Koukitu, T. Taki, N. Takahashi, and H. Seki, J. Cryst. Growth **197**, 99 (1999).

[53] M. Adachi, Y. Murakami, A. Hashimoto, and A. Yamamoto, Proceedings of the International Workshop on Nitride Semiconductors (IWN’ 2000) Nagoya, Japan, September 24–27, IPAP conference series 1, p.339 (2000).

[54] S. Keller, I. Ben-yaacov, S. P. Denvers, and U. K. Mishra, Proceedings of the International Workshop on Nitride Semiconductors (2000), Nagoya, Japan, September 24–27, IPAP conference series 1, p.233 (2000).

[55] A. Yamamoto, M. Tsujino, M. Ohkubo, and A. Hashimoto, Sol. Energy Mater. Sol. Cells **35**, 53 (1994).

[56] A. Yamamoto, Y. Murakami, K. Koide, M. Adachi, and A. Hashimoto, Phys. Stat. Sol. (b) **228**, 5 (2001).

[57] A. Yamamoto, T. Shin-ya, T. Sugiura, and A. Hashimoto, J. Cryst. Growth **189/190**, 461 (1998).

[58] A. Koukitu and H. Seki, Jpn. J. Appl. Phys., Part **236**, L750 (1997).

[59] V. V. Mamutin, V. A. Vekshin, V. Y. Davydov, V. V. Ratnikov, T. V. Shubina, S. V. Ivanov, P. S. Kop’ev, M. Karlsteen, Soderwall. U, and M. Willander, Phys. Stat. Sol. (a) **176,** 247 (1999).

[60] H. Lu, W. J. Schaff, J. Hwang, H. Wu, W. Yeo, A. Pharkya, and L. F. Eastman, Appl. Phys. Lett. **77,** 2548 (2000).

[61] V. Y. Davydov, A. A. Klochikhin, Semiconductors **38**, 861 (2004).

[62] M. Alevli, G. Durkaya, A. Weerasekara, A. G. U. Perera, N. Dietz, W. Fenwick, V. Woods, I. Ferguson, Appl. Phys. Lett. **89**, 112119 (2006).

[63] J. B. MacChesney, P. M. Bridenbough, P. B. O'Connor, Mat. Res. Bul. **5**, 783 (1970).

[64] B. H. Cardelino, C. E. Moore, C. A. Cardelino, N. Dietz, Proc. SPIE 5912 (2005).

[65] N. Dietz, III-Nitrides Semiconductor Materials, edited by Z. C. Feng, Imperial college Press, chapter 6 (2006).

[66] N. Dietz, M. Alevli, H. Kang, M. Strassburg, V. Woods, I. Ferguson, C. E. Moore, B. H. Cardelino, Proc. SPIE 5912 (2005).

[67] N. Dietz, M. Alevli, V. Woods, M. Strassburg, H. Kang, I. T. Ferguson, Physica Status Solidi B-Basic Solid State Physics **242**, 2985 (2005).

[68] N. Dietz, M. Strassburg, V. Woods, J. Vac. Sci. & Technol. A **23**, 1221 (2005).

[69] V. Woods, N. Dietz, Materials Science and Engineering B-Solid State Materials for Advanced Technology **127**, 239 (2006).

[70] M. Alevli, Dissertation, Chapter III, (2008).

[71] L. A. Marasina, I. G. Pichugin, and M. Tlaczala, Krist. Tech. **12**, 541 (1977).

[72] D. C. Look, J. R. Sizelove, J. Jasinski, Z. Liliental-Weber, K. Saarinen, S. S. Park, and J. H. Han, in *Mater. Res. Soc. Symp. Proc.*, 575 (2003).

[73] Z. C. Feng, *III-Nitride Semiconductor Materials* (Imperial College Press, 2006).

[74] N. Takahashi, R. Matsumoto, A. Koukitu, and H. Seki, Jpn. J. App. Phys. **36,** L743-L745 (1997).

[75] T. Suntola, J. Antson, US Patent no. 4,058,430 (1977).

[76] M. Leskela, L. Niinisto, in: T. Suntola, M. Simpson (Eds.), Atomic Layer Epitaxy, Blackie, Glasgow, p.1 (1990).

[77] J. Nishizawa, H. Abe, T. Kurabayashi, J. Electrochem. Soc.**132**, 1197 (1985).

[78] S. M. Bedair, M.A. Tischler, T. Katsuyama, N. A. El-Masry, Appl. Phys. Lett. **47**, 51 (1985).

[79] T. Yao, in: T. Suntola, M. Simpson (Eds.), Atomic Layer Epitaxy, Blackie, Glasgow, p.155 (1990).

[80] T. Suntola, Mater. Sci. Rep. **4**, 261 (1989).

[81] M. Ritala, M. Leskela, J.-P. Dekker, C. Mutsaers, P.J. Soininen, J. Skarp, Chem. Vap. Depos. **5**, 7 (1999).

[82] K. Kukli, M. Ritala, M. Leskela, Appl. Phys. Lett. **66**, 3737 (1996).

[83] M. Ritala, K. Kukli, A. Rahtu, et al., Science **288**, 319 (2000).

[84] O. Ambacher, J. Phys. D: Appl. Phys **31,** 2653 (1998).

[85] R. Juza and H. Hahn, Z. Anorg. Allg. Chem. **239**, 282 (1938).

[86] T. L. Tansley and C. P. Foley, J. Appl. Phys. **59**, 3241 (1986).

[87] A. Yamamoto, T. Tanaka, A. G. Bhuiyan, K. Sugita, K. Kasashima, Y. Kimura, A. Hashimoto, and V. Yu. Davydov, 5th International Conference on Nitride Semiconductors (ICNS-5), Nara, Japan, May 25–30, (2003).

[88] T. L. Tansley and C. P. Foley, in Proceedings of the 3rd International Conference on Semi-Insulating III-V Materials, Warm Springs, Oregon, p.497 (1984).

[89] D. W. Jenkins and J. D. Dow, Phys. Rev. B **39**, 3317 (1989).

[90] T. L. Tansley and C. P. Foley, Electron. Lett. **20**, 1066 (1984).

[91] M. Sato, Jpn. J. Appl. Phys., Part 2 **36**, L658 (1997).

[92] S. Yamaguchi, M. Kariya, S. Nitta, T. Takeuchi, C. Wetzel, H. Amano, and I. Akasaki, J. Appl. Phys. **85**, 7682 (1999).

[93] A. Yamamoto, T. Tanaka, K. Koide, and A. Hashimoto, Phys. Stat. Sol. (a) **194**, 510 (2002).

[94] H. Lu, W. J. Schaff, L. F. Eastman, J. Wu, W. Walukiewicz, K. M. Yu, J. W. Auger III, E. E. Haller, and O. Ambacher, Abstract of the 44th Electronic Material Conference, Santa Barbara, CA, June 26–28, 2002; J. Electron. Mater., W. J. Schaff (private communication, Cornell University, Ithaca, NY).

[95] H. Lu, W. J. Schaff, J. Hwang, H. Wu, W. Yeo, A. Pharkya, and L. Eastman, Appl. Phys. Lett. **77**, 2548 (2000).

[96] T. V. Shubina, S. V. Ivanov, V. N. Jmerik, D. D. Solnyshkov, V. A. Vekshin, P. S. Kop'ev, A. Vasson, J. Leymarie, A. Kavokin, H. Amano, K. Shimono, A. Kasic, B. Monemar, Phys. Rev. Lett. **92**, 117407 (2004).

[97] T. Inushima, V. V. Mamutin, V. A. Vekshin, S. V. Ivanov, T. Sakon, M. Motokawa, and S. Ohoya, J. Cryst. Growth **227–228**, 481 (2001).

[98] V. Y. Davydov *et al.*, Phys. Stat. Sol. (b) **230**, R4 (2002).

[99] V. Y. Davydov *et al.*, Phys. Stat. Sol. (b) **234**, 787 (2002).

[100] F. Matsuda, Y. Saito, T. Muramatsu, T. Yamaguchi, Y. Matsuo, A. Koukitu, T. Araki, Y. Nanishi, Phys. Stat. Sol. (c) 0 (2003).

[101] R. P. Bhatta, Dissertation, Chapter IV, (2008).

[102] M. Seelmann-Eggebert, J. L. Weher, H. Obloh, H. Zimmermann, A. Rar, and S. Porowski, Appl. Phys. Lett. **71**, 2635 (1997).

[103] X. Wang, A. Yoshikawa, Progress in Crystal growth and Characterization of Materials **48/49**, 42 (2004).

[104] H. Naoi, D. Muto, T. Hioka, Y. Hayakawa, A. Sujuki, T. Araki, and Y. Nanishi, Phys. Stat. Sol. (b) **244**, 1834 (2007).

[105] Y. Saito, Y. Tanabe, T. Yamaguchi, N. Teraguchi, A. Suzuki, T. Araki, and Y. Nanishi, Phys. Stat. Sol. (b) **228**, 13 (2001).

[106] K. Rapcewicz, M.B. Nardelli, J. Bernholc, Physical Review B **56**, 12725 (1997).

[107] J. Elsner, M. Haugk, G. Jungnickel, T. Frauenheim, Solid State Commun. **106**, 739 (1998).

[108] V. M. Bermudez, Surf. Sci. **565**. 89 (2004).

3 CHARACTERIZATION TECHNIQUES AND METHODS

3.1 Introduction

In order to perform various characterizations of samples, a number of experimental tools and methods are required. The details of the characterization techniques and methods that have been implemented to accomplish this work are discussed in this chapter. In order to do the compositional analysis and monitor the surface cleanliness of the samples Auger electron spectroscopy (AES) is used. The structural characterization of the surface of the samples is done by using low energy electron diffraction (LEED). To study the surface configuration and molecular bonding on the surface, high resolution electron energy loss spectroscopy (HREELS), a surface sensitive vibrational spectroscopic technique, is implemented. Raman spectroscopy is used to study the local bonding in a crystal, whereas long range ordering, i.e., bulk structure is studied by x-ray diffraction (XRD). To scrutinize the kinetics of thermal desorption, temperature programmed desorption (TPD) is employed. In order to find the layer thickness and void fraction, experimental IR reflection spectra are analyzed using a multilayer stack model and Lorentz-drude model. The surface morphology of the epilayers is characterized by atomic force microscopy (AFM). The experiments on AES, LEED, HREELS and TPD were performed in our surface science lab at Georgia State University. The Raman spectroscopy and IR reflection spectroscopy measurements were carried out in Dr. Dietz's lab at Georgia State University. The XRD measurements were done in Dr. Collazo's lab at North Carolina State University, Raleigh and in Dr. Fergusson's lab at University of North Carolina, Charlotte. AFM measurements were performed in Dr. Mustafa's lab at Marmara University, Turkey. Details of the experimental set up and the characterization techniques mentioned here are presented in Victor Bellito's

dissertation [1] and Mustafa Alevli's dissertation [2]. However, it seems relevant to report a brief description of each characterization technique in this dissertation too.

3.2 Low energy electron diffraction

Low-energy electron diffraction (LEED) is the most common technique for the determination of the surface structure [3-5] of crystalline materials by bombardment with a collimated beam of low energy electrons (20-200eV) and observation of diffraction pattern of the electrons scattered from the crystal surface. This technique was discovered in 1927. However, the use of this technique did not gain popularity among the researchers for surface analysis until early 1960s. Due to inadequate vacuum techniques, monitoring directions and intensities of diffracted beams were quite difficult experimentally. In addition, LEED required well-ordered surface structures since it is a surface sensitive technique. In the early 1960s, with the availability of commercial ultra high vacuum devices, the LEED method became an attractive tool for the determination of surface structure of crystalline materials. Using this technique diffracted electrons are accelerated to high energies to produce clear and visible diffraction patterns on a fluorescent screen.

The principle of the LEED method is similar to x-ray diffraction (Bragg's law). According to the wave-particle duality principle, electrons also behave like a wave. The wavelength associated with this wave, called de Broglie wavelength, is given as $\lambda = \frac{h}{p}$, where momentum is calculated by p = mass × velocity = $(2mE_k)^{1/2}$ = $(2meV)^{1/2}$, and where h is the Planck's constant, m is the mass of an electron , e is the electronic charge and V is the

accelerating voltage. Also, inserting the value $p = \sqrt{2meV} = \sqrt{2mE(eV)}$ in equation $\lambda = \frac{h}{p}$ we get,

$$\lambda(\overset{0}{A}) = \left[\frac{150}{E(eV)}\right]^{\frac{1}{2}}$$

where E is the energy in eV. Therefore, as electron energy is increased from 20 to 100 eV, electron wavelength decreases from 2.7 to 0.87 Å. This distance is in the range of interatomic spacing on a surface which is one of the necessary conditions for diffraction. If a beam of low energy electrons is directed at a surface, 1 to 5% of them will be elastically scattered. These elastically scattered electrons can be accelerated into a fluorescent screen. If the surface is well ordered, a pattern of spots will appear due to diffraction of the electrons off of the atoms at or near the crystal surface. The condition for constructive interference of scattered electrons of wavelength λ incident normal on a surface with atoms spaced d apart is, $n \lambda = d \sin\theta$, where n is an integer and θ is the scattering direction measured from the surface normal. Since the surface is a two dimensional array of atoms, interference spots are observed instead of the streaks which are observed for a multiple slit experiment. Due to the low incident energy (< 100 eV), electrons used in LEED penetrate ~ 1 nm before being scattered whereas in x- ray diffraction, the energy used is ~ 30 keV which can penetrate ~ 10^5 nm [5] into the crystal lattice. This is the reason LEED is a sensitive technique for determining surface structure.

Figure 3.1 is a schematic representation of the LEED apparatus [1]. The LEED system consists of four metal grids at different voltages, a fluorescent screen (kept at 6 keV positive potential) and an electron gun which produces the primary electron beam. The sample is

mounted perpendicular to the electron gun. The first grid (counted from the sample) is at ground potential to ensure a field free region around the sample. The next two grids are set to the so-called retarding voltage. This voltage is slightly lower than the kinetic energy of the electrons produced by the gun. It repels almost all the inelastically scattered electrons. The elastically scattered electrons pass the next grid which is set to ground voltage again and are then accelerated towards the fluorescent screen which is set to a high positive voltage. Behind the screen there is a window in the vacuum system so that the LEED pattern can be observed directly or recorded with a camera. The analysis of spot positions provides information on the size, symmetry and rotational alignment of the substrate unit cell as well as the adsorbate unit cell. The sharpness and intensity of the spots is a measure of the degree of surface order. Intensity in the background is an indication of surface disorder. So, bright spots and a dark background on the fluorescent screen indicate the well-ordered surface of the sample.

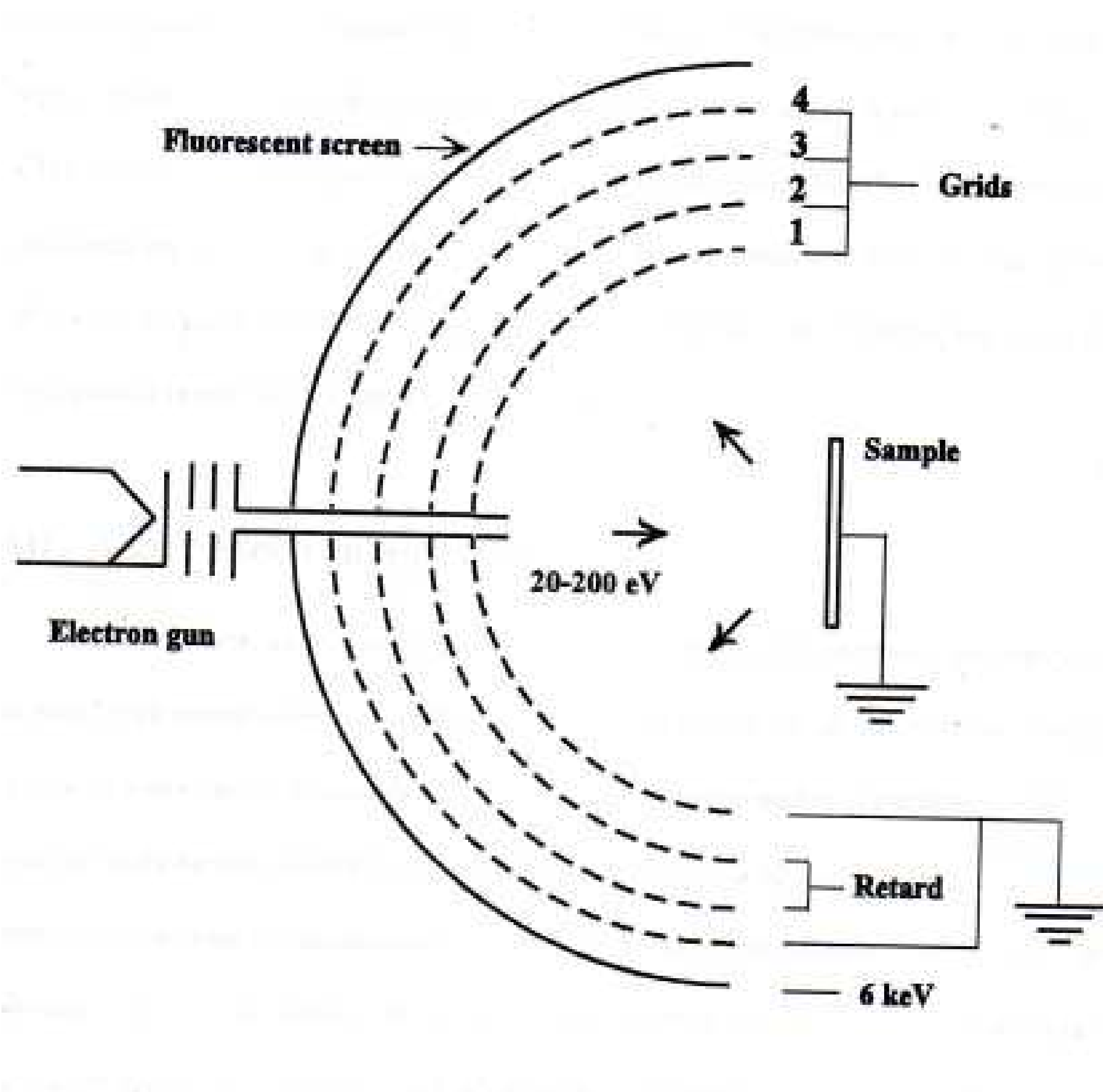

Figure 3.1 Schematic diagram of the LEED system.

3.3 Auger electron spectroscopy

Auger electron spectroscopy (AES), also called Auger spectroscopy was developed from the effect that was first observed by Pierre Auger [6], a French physicist in the mid-1920s. AES is a surface sensitive technique which uses the emission of low energy electrons in the Auger process. It is one of the most commonly employed surface analytical techniques for quantitative analysis of the surface region [3-5, 7]. It is also equally applicable to monitor the surface cleanliness of the samples. In addition, it can be used to determine the chemical states of elements and depth profiling by inert gas sputtering. The sensitivity of AES is very high (about 1% of a monolayer).

In an Auger process, a high energy incident electron strikes the core level electron and ionizes the atom. The vacancy created due to ionization of core level electron is filled with the jump of an electron from upper energy level. Due to this jump of the electron, either an x-ray is released or the energy is shared with another electron at a higher energy level and secondary ionization takes place. This ejected electron during secondary ionization is called Auger electron. The kinetic energy of Auger electron is independent of energy of the incident electron but is the characteristic of the material [8]. The result is a spectrum of the intensity of electrons as a function of the kinetic energy of the Auger electron with the placement of the peaks giving a qualitative view of what elements are present on the surface.

Figure 3.2 represents the schematic diagram of the Auger electron emission process. As shown in the figure, a high energy electron (typically 2-3 keV) is incident which knocks out a core level electron from the atom with energy state E_1. An electron from the upper energy level E_2 falls to the energy level E_1 to fill the vacancy. The energy released in this process either comes out in the form of x-rays or is shared by another electron in the energy state E_3. A part of

this energy is used to overcome the binding energy of the electron in the energy state E_3 and the remaining energy is imparted to the electron (Auger electron) as kinetic energy. Therefore, the kinetic energy of the Auger electron can be expressed in terms of energy levels as,

$$KE = (E_1 - E_3) - E_3.$$

This kinetic energy of Auger electron is independent of the incident energy of the electron and the mechanism of the initial core hole formation. It is characteristic of the material. In the Auger spectrum, peaks at various kinetic energies are observed which correspond to the elements present on the sample being analyzed.

A schematic representation of the Auger system [1] is shown in Fig. 3.3. We use a spherical grid type retarding field analyzer (RFA) for acquisition of Auger data. The experimental set up of Auger system is similar to that of LEED system except the electronics. The two center grids (2 & 3) are connected so that they can discriminate energy of the electrons and only those electrons which succeed to reach fluorescent screen can be determined. Lanthanum-hexaboride (LaB_6) filament is used as a cathode which can emit electrons at low power inputs. In order to emit a consistent beam of electrons, the cathode is heated by passing a current of 1.2 A. The beam of electrons is accelerated to 3 keV energy and focused on to the sample surface. Depending upon the material to be analyzed, the range of energy is varied to different values. For InN samples, the range of energy used is 100 – 550 eV and that for InGaN samples, the range is 100 – 1150 eV. Emitted electrons have energy in the range of 50 – 1200 eV and in this range electrons have a short mean free path in a solid. Only the electrons emitted from the top few layers of the sample emerge with the characteristic energy. Thus AES is surface sensitive. This technique is used for quantitative analysis of the surface region as well as for monitoring the surface cleanliness. However, AES has some limitations. Since AES is a three

electron process, it is not sensitive to hydrogen and helium. AES can be used only for metals and semiconductors. In case of insulators, study by AES is difficult due to surface charging. Due to the high energy electrons beam, this technique may damage the sample surface.

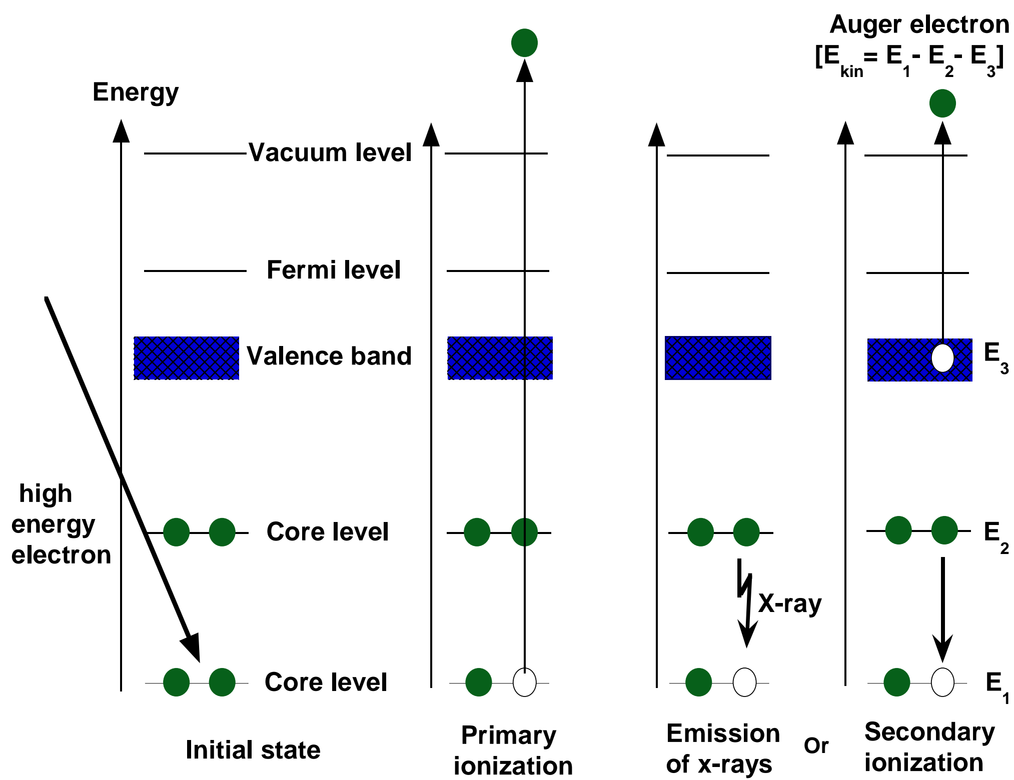

Figure 3.2 Schematic representation of Auger electron process.

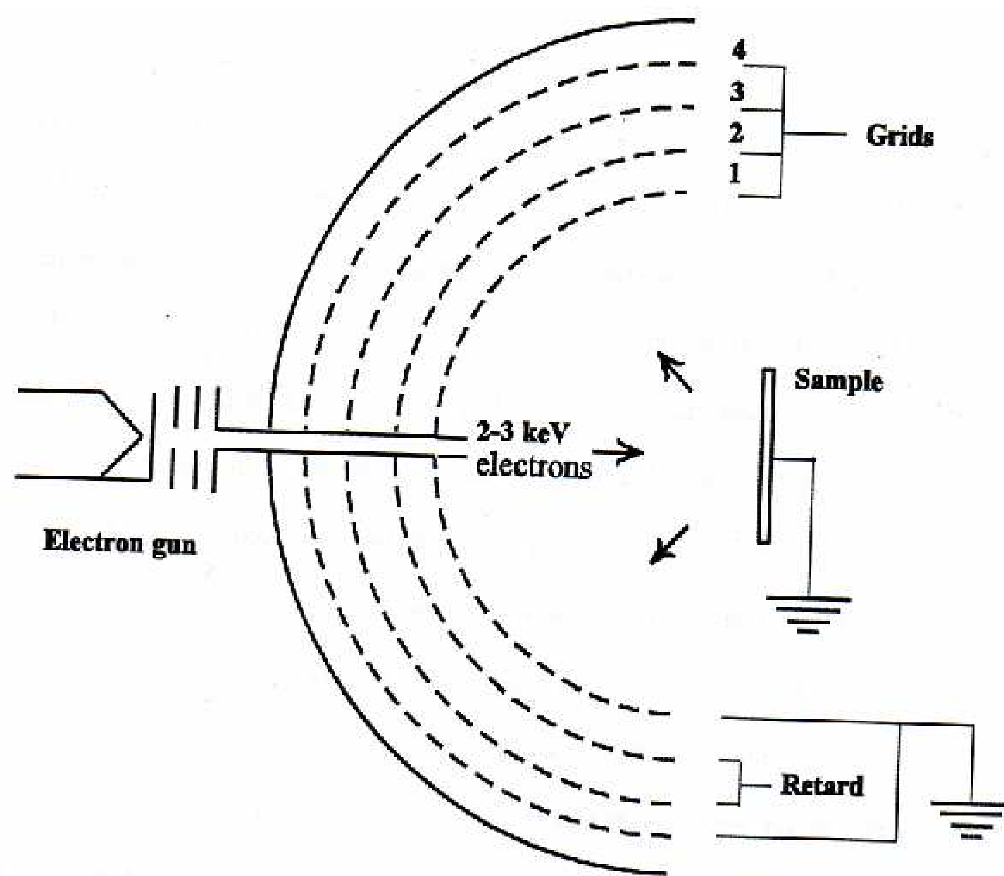

Figure 3.3 Schematic diagram of AES apparatus.

3.4 Raman spectroscopy

Raman spectroscopy is a spectroscopic technique used to study vibrational, rotational, and other low-frequency modes in a system [9]. It can also be used to determine structure, free carrier concentration and to analyze stress as well as defect in the crystal lattice [2]. When a sample is illuminated by a light source (usually laser beam), the interaction of electromagnetic wave with matter leads to polarization. The induced polarization includes two terms, elastic scattering (Rayleigh scattering) and inelastic scattering (Raman scattering). The Raman effect occurs when light impinges upon a molecule and interacts with the electron cloud and the bonds of that molecule. When the molecule relaxes it emits a photon and it returns to a different rotational or vibrational state. The difference in energy between the original state and this new state leads to a shift in the emitted photon's frequency away from the excitation frequency. If the final vibrational state of the molecule is more energetic than the initial state, then the emitted photon will be shifted to a lower frequency in order for the total energy of the system to remain balanced. This shift in frequency is designated as a Stokes shift. If the final vibrational state is less energetic than the initial state, then the emitted photon will be shifted to a higher frequency, and this is designated as an Anti-Stokes shift. According to the symmetry of the crystal and vibrational mode, the intensity of the scattered radiation has a non-zero value only for specific polarizations and scattering geometries. These are known as Raman selection rules, which are essential for determining the crystal symmetry and allowed Raman modes. Hexagonal InN crystallizes into wurtzite structure with four atoms in the unit cell and belongs to C^4_{6v} space group. According to group theory analysis at the Γ point, the phonon modes in hexagonal InN are characterized by the following irreducible representations,

$$\Gamma_{ac} + \Gamma_{opt} = (A_1 + E_1) + (A_1 + 2B_1 + E_1 + 2E_2). \qquad (3.1)$$

Raman selection rules predict that A_1 and E_1 modes are both Raman and IR active, E_2 is only Raman active and B_1 is the silent mode. Thus six optical modes may be observed in a first order Raman spectrum [10]: E_2(high), E_2(low), E_1(LO), E_1(TO), A_1(TO), and A_1(LO). The Raman selection rules for the wurtzite structure of group III-nitrides are given in Table 3.1, of which x(yz)y belongs to 90° scattering geometry, while $z(xy)\bar{z}$, $x(zz)\bar{x}$, $x(yy)\bar{x}$, and $x(yz)\bar{x}$, belong to the backscattering geometry. The allowed modes are highly sensitive to the polarization of the incident light and orientation of the crystal. Hexagonal InN thin films are usually grown along the [0001] direction of the substrate, which puts the c-axis of the hexagonal structure perpendicular to the crystal plane. Therefore, under backscattering geometry, the $z(xx)\bar{z}$, and $z(xy)\bar{z}$ configurations are easily observable due to the z-direction being along the [0001] direction.

Raman measurements were carried out with a custom built Micro Raman spectrometer, which consists of a McPherson 2062 scanning monochromator as the main monochromator, and a McPherson 275 DS double subtractive monochromator as a variable notch filter with an 2.33 eV excitation source. The signal is collected by a nitrogen cooled CCD.

Table 3.1 Raman Selection rules for hexagonal group III-nitrides.

Configuration	Allowed Mode
$z(xx)\bar{z}$	A_1(LO), E_2(low), E_2(high)
$z(xy)\bar{z}$	E_2(low), E_2(high)
$x(zz)\bar{x}$	A_1(LO)
$x(yy)\bar{x}$	A_1(LO), E_2(low), E_2(high)
$x(yz)y$	E_1(TO), E_1(LO)
$x(yz)\bar{x}$	E_1(TO), E_1(LO)

3.5 X-ray diffraction

X-ray diffraction (XRD) is a non destructive technique which is used to determine atomic arrangement, crystalline phases and structural properties of crystals. In addition, it is used to determine the lattice parameters, strain, grain size, epitaxy, phase composition, preferred orientation and to measure the thickness of thin films and multi-layers. This technique is based on the principle of Bragg's law in which a beam of x-rays is incident on atomic planes of the crystal and exhibit the phenomenon of diffraction. A schematic diagram of the x-ray diffraction from the parallel atomic planes is shown in Fig. 3. 4. X-rays diffracted from neighboring parallel atomic planes interfere either destructively or constructively. When the waves interfere constructively, a large output signal is obtained and no signal is obtained in case of destructive interference. For constructive interference to occur, the diffracted waves should satisfy Bragg's condition which is given as:

$$n\lambda = 2d\sin\theta \qquad (3.2)$$

where n is an integer (order of diffraction), λ is the wavelength of the x-ray source, d is the lattice spacing and θ is the Bragg angle. The diffraction pattern from the epilayers is analyzed to determine the a-spacing and c-spacing lattice constants of the crystal according to Bragg's law. In addition, the line width of a rocking curve measurement (ω scans), i.e., full width at half maximum (FWHM), on the a-axis or c-axis may be used to determine the crystalline quality.

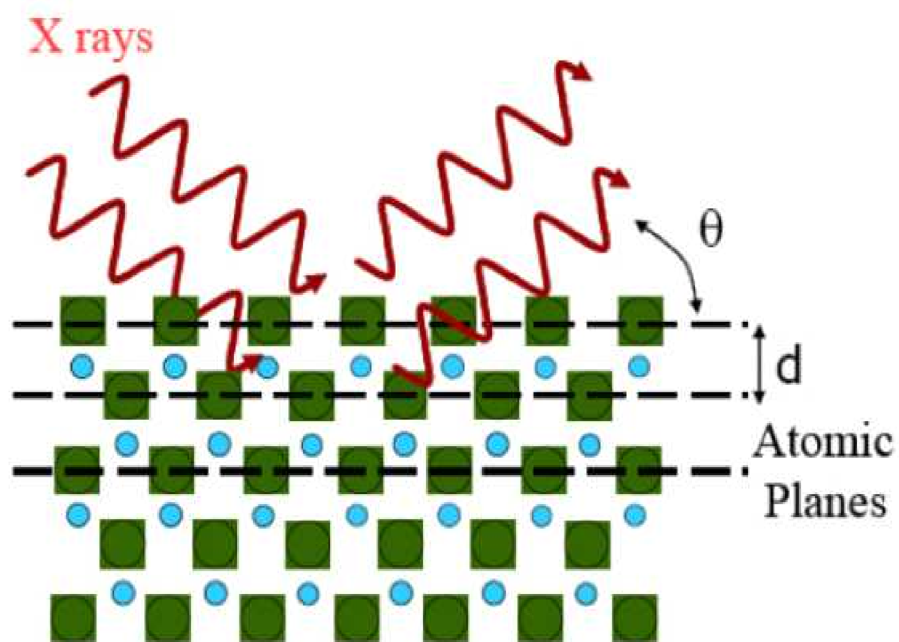

Figure 3.4 A schematic diagram of x-ray diffraction.

3.6 Infrared reflection spectroscopy

3.6.1 Theoretical model

Infrared (IR) reflection spectroscopy is the technique which deals with the infrared region of the electromagnetic spectrum. Experimental infrared reflection spectra are fit to a model by introducing a dielectric function and analyzed to obtain the phonon and plasmon properties, carrier concentrations, carrier mobility, layer thickness, and interface behavior. The dielectric function is determined by establishing the interaction of electromagnetic radiation with the matter through solution of equations of motion for atoms. Assuming the contribution of phonons and free carriers, the IR dielectric function can be written in the following form [2].

$$\varepsilon = \varepsilon(\omega) = \varepsilon_\infty + \sum_i \frac{s_i\left(\omega_{TO}^2 - \omega_{LO}^2\right)}{\omega_{TO}^2 - \omega^2 - i\omega\Gamma} - \frac{\varepsilon_\infty \omega_p^2}{\omega^2 + i\omega\gamma_p}, \qquad (3.3)$$

where γ_p is the electron damping due to the scattering from randomly distributed stationary impurities, ω_p is the plasmon frequency, Γ is the oscillating broadening constant, ω_{TO}, ω_{LO}, S_i are the frequency, oscillator strength, and damping parameter of the ith oscillator, respectively, and ε_∞ is the dielectric response in the high-energy limit for the film. Light propagation in a multilayer thin film structure is modeled using the Transfer Matrix Method [11, 12], assuming a certain number of uniform layers each with own characteristic parameters. Reflectivity is calculated by solving the Maxwell equations for plane electromagnetic waves with boundary conditions for the electric and magnetic field components at the air/film and film/substrate interfaces. There are two waves with the electric-field amplitudes E^+ and E^- propagating in opposite directions in each layer. If air, film and substrate are represented by “0”, “1” and “2”, respectively, the resultant matrix M_r is described by the following equation [9].

$$M_r = M_{01}\, M_1\, M_{12} \qquad (3.4)$$

The reflectance is given by the equation,

$$R = \left| \frac{M_{r1,0}}{M_{r1,1}} \right|^2 \tag{3.5}$$

3.6.2 Experimental methods

Infrared reflection measurements were performed using the Perkin Elmer system 2000 Fourier transform infrared spectrometer along with a Graseby reflection accessories set up. A mercury cadmium telluride detector was used for the short wavelength (1.5 – 20 μm) range, and a TGS based pyroelectric detector was used for the long wavelength (< 50 μm) range. An aluminium mirror was used to collect background spectra I_o. Then, this mirror was replaced with InN sample and scanned for the same number of interferograms. After Fourier transformation, this yields I_R, the reflected intensity spectrum. The reflectivity spectrum R of the InN film is then determined by the ratio I_R/I_o. The best-fit parameters for the InN film and GaN film were obtained using the nonlinear Levenberg-Marquardt [13] fitting algorithm.

3.7 High resolution electron energy loss spectroscopy

High resolution electron energy loss spectroscopy (HREELS) is a non destructive and surface sensitive vibrational spectroscopic technique. This technique utilizes the inelastic scattering of low energy electrons to study the vibrations of adsorbates on the crystal surface [14-16]. Due to the high-sensitivity (<0.1 % of a monolayer) and broad spectral range (0-1000 meV), HREELS is one of the most effective tools to explore the properties of a wide variety of surfaces which include single crystal metals, semiconductors and polycrystalline foils and polymers. In this technique, a highly monochromatic beam of electrons is incident on a crystal surface at a certain angle and inelastically scattered electrons pass through the analyzer. Normally,

inelastically scattered electrons are collected in a specular direction and analyzed spectroscopically. The scattering of electrons may take place by two mechanisms: dipole scattering and impact scattering. Dipole scattering is small-angle scattering in which the incident electrons interact with long range field set up in the vacuum above the crystal surface by the oscillating dipoles. Dipolar scattering is produced not only by vibrational motions of adsorbed molecules and atoms in the crystal surface, but also by any elementary excitation of the sample accompanied by a fluctuation in charge density [14]. While in impact scattering regime, the scattering of electrons is large-angle scattering where a fully microscopic description of the interaction of electrons with the vibrating substrate is required.

The energy loss of the electrons is of the order of few hundred milli electron volts. The analyzer must be capable of high resolution and the incident beam must be highly monochromatic in order to get high resolution with the spectrometer. It is generally useful to combine the HREELS measurement with other surface techniques, primarily those of LEED and AES which enable the HREELS data to be interpreted. The basic theory applicable in the HREELS experiment is shown in the Fig. 3.5.

The HREELS apparatus used in our surface science lab is the ELS3000, manufactured by LK technology which may have resolution below 2 meV and the incident energy of the electron can be varied in the range of 1 to 200 eV. The spectrometer consists of a symmetrical system of input-output zoom lenses positioned between monochromator and analyzer which is used to focus and accelerate/decelerate the electron beam to and from the sample surface. A schematic representation of the HREEL spectrometer [1] is shown in the Fig. 3.6. The ELS3000 spectrometer consists of a cathode containing lanthanum-hexaboride filament which generates electrons on heating the cathode. The electrons can leave the source` only through a lens system

(emission system), e.g., a slot lens system consisting of several slits all on different potential. The purpose of this system is to focus the electrons on the entrance of the monochromator unit to get a high initial electron flux. The monochromator is usually in a cylindrical shape. It lets only those electrons pass which have the chosen initial energy. To make the apparatus more sensitive, an additional monochromator, the second monochromator is used. The electrons are then focused by a lens system onto the sample. Inelastically scattered electrons from the sample pass into the analyzer through a lens system in a specular direction. The analyzer again allows electrons of certain energies to pass to a channeltron, a channel electron multiplier. The analyzer energy is varied to accumulate a spectrum, a plot of intensity vs the energy loss of electrons. The analyzer is fixed in its position but both the monochromators and the sample can be rotated from 0 to 90° to investigate angular distribution of the scattered electrons. Dual magnetic shields are provided at the flange to interface with the chamber magnetic shields in order to minimize the ambient magnetic fields for satisfactory operation. To perform HREELS experiments, the incident energy of the electron is varied from 7 to 35 eV and the loss energy less than 500 meV is detected. The energy loss of electrons is usually expressed in terms of meV or wave number (reciprocal cm), where 1 meV = 8.056 cm^{-1}.

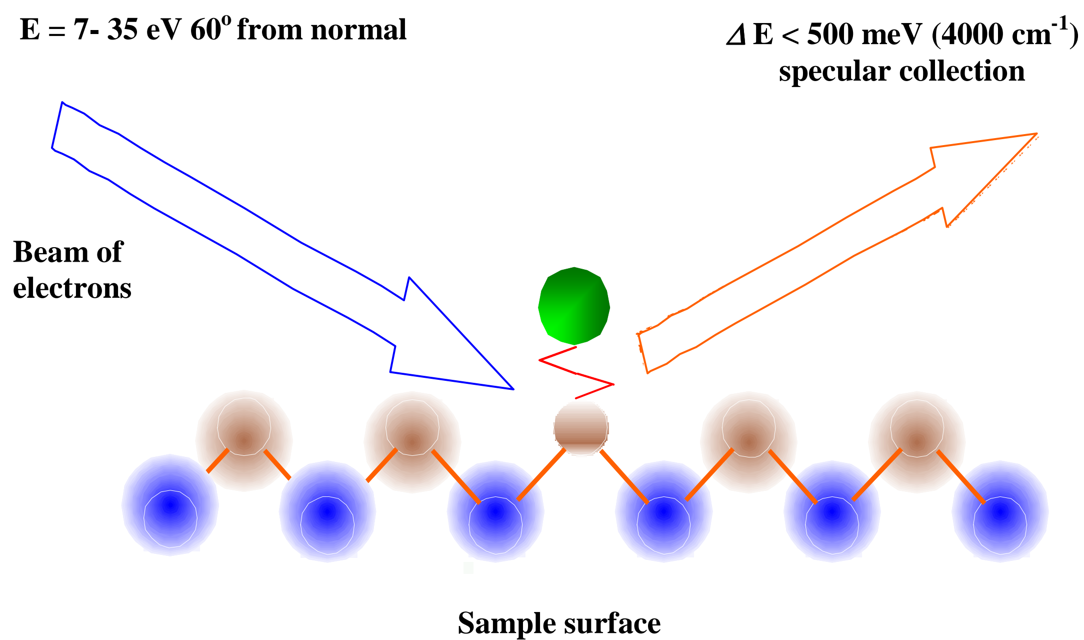

Figure 3.5 Schematic representation of HREELS theory.

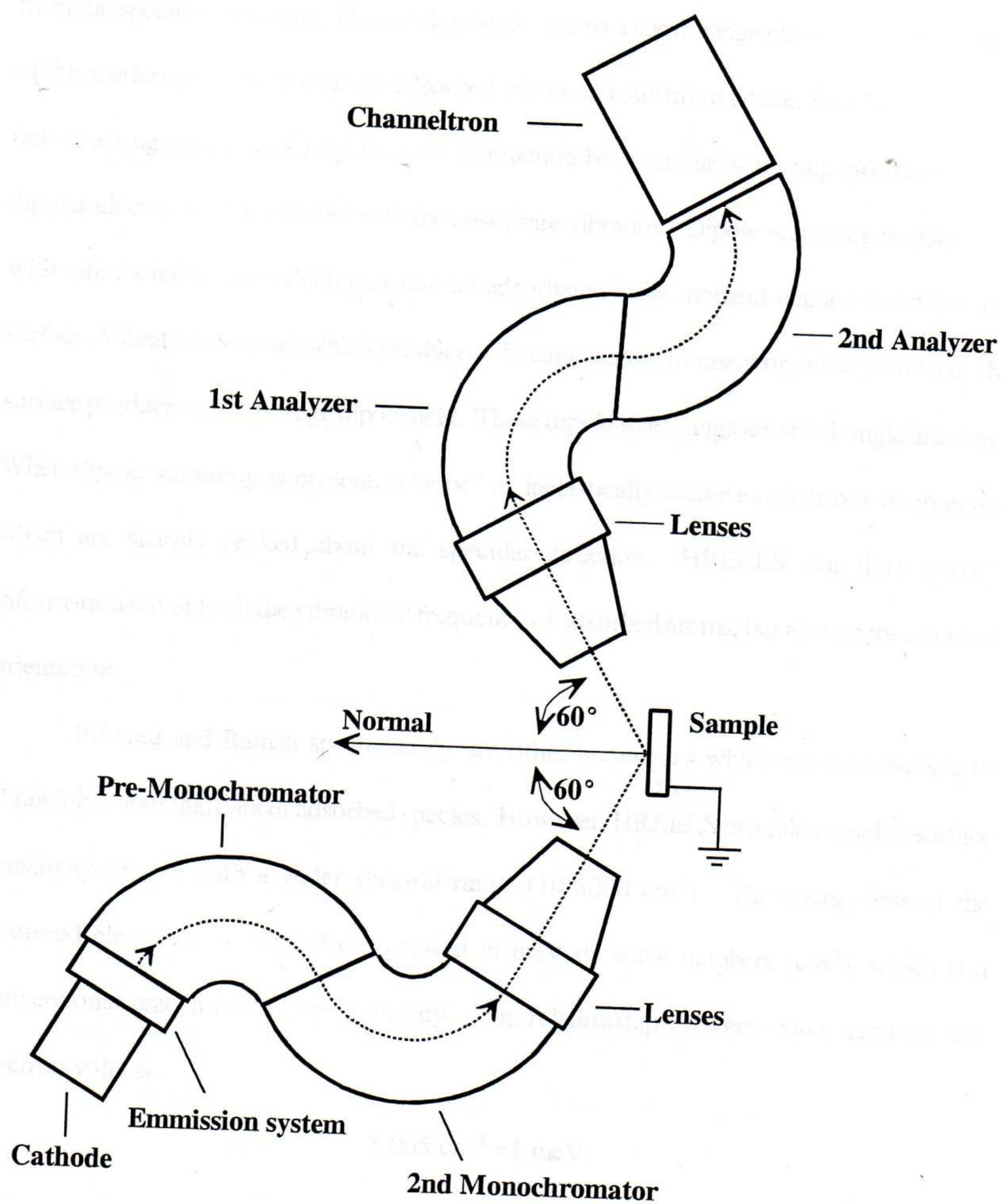

Figure 3.6 Schematic representation of HREEL spectrometer.

3.8 Temperature programmed desorption

3.8.1 Experimental set up

In order to study the kinetics of desorption from semiconductor surfaces, temperature programmed desorption is one of the most important techniques. This technique has been employed successfully for semiconductor surfaces such as Si [17], diamond [18-20], GaAs [21], GaN [22-24], InP [25], and InN [26]. In this technique, the sample surface is generally heated at uniform rate or held at constant temperature. The sample surface is cleaned and desorption of species from the sample surface is performed in a UHV chamber. A schematic diagram of the temperature programmed desorption system is shown in Fig. 3.7. While heating the sample surface with a PID (Proportional Integral Differential) temperature controller, the desorbing flux of selected species and the temperature are recorded by a differentially-pumped mass spectrometer. The details of the mass spectrometry system used in our lab can be found in V. J. Bellitto's dissertation [1]. The desorbed species pass through a small aperture in a nose cone to eliminate signal from background gas or species desorbed from the sample mount. These species are ionized and monitored by a mass spectrometer residing inside the nose cone. The mass spectrometer measures the mass to charge ratio of the ionized species (m/e). Depending on the required analysis, a single mass to charge ratio or multiple mass to charge ratios can be recorded. In these experiments, the effect of re-adsorption is normally neglected due to the large pumping speed. In addition, thermalization is considered to be very fast compared to desorption and the sample is assumed to be in thermal equilibrium.

3.8.2 Theoretical background

When the thermal energy is equal to the adsorption energy of the adsorbed species, the species may desorb from the surface or combine with another species before desorbing and return into the gas phase. This is called the process of thermal desorption. The surface thermal desorption rate R(t) of adsorbed species is generally given by the expression [27],

$$R(t)= - d\theta/dt = \theta^n \nu_n \exp^{-(E/kT)} , \qquad (3.6)$$

where θ is the surface coverage, n is the order of desorption, ν is the pre-exponential factor, E is the activation energy, k is the Boltzmann constant and T is the temperature in Kelvin. The TPD method can be used effectively to determine the value of desorption order n, the activation energy E and the pre-exponential factor ν.

Depending upon the nature of desorption of the species from the heated surface, the desorption orders are generally grouped into 4 types; first order, second order, half order and zero order desorption. In first order desorption (Fig. 3.8a), all the adsorbed particles have the same probability of desorption. This means all the adsorbed particles are independent of each other. The only binding is from the attachment with the surface and is the same to all. In second order desorption (Fig. 3.8b), the detected particles are the chemical combination of the two identical adsorbed surface particles and the combination of the particles is made during the process of desorption. Each component is randomly distributed and the possibility of combination is proportional to the square of the coverage. In half order desorption (Fig.3.8c), the surface particles are distributed in islands. The desorption energy of the particles on the border of the islands is smaller than those inside it so they are more easily activated. In zero order desorption (Fig.3.8d), the surface has built up multiple layers of surface species before heating,

As a result, the desorbed particles do not change the coverage at all and the desorption is temperature dependent only.

Thermal stability of InN epilayers is very important factor in the growth process as well for the device performance and life time. However, fewer studies have been done on the thermal stability and decomposition behavior of the InN epilayers than have been reported for electronic, structural and optical properties. Details of the thermal stability of InN epilayers are presented in chapter 5.

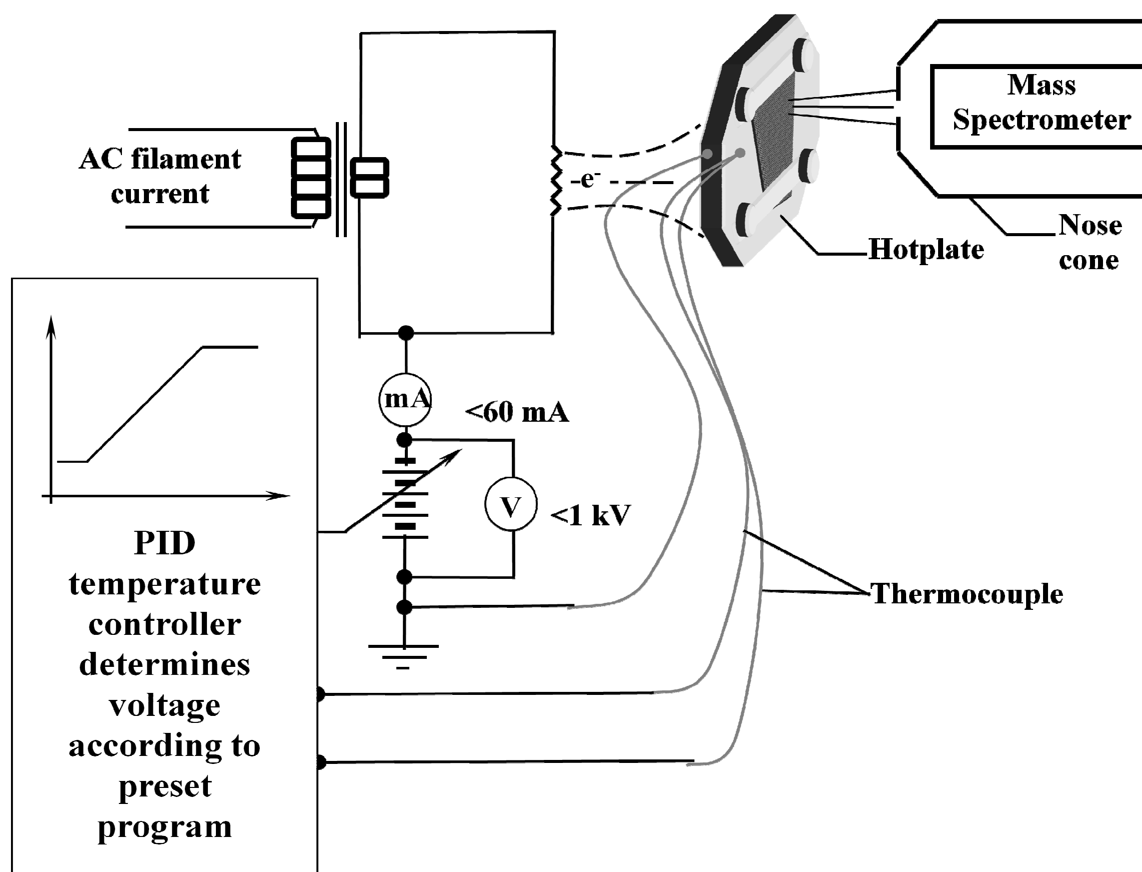

Figure 3.7 Schematic diagram of TPD system.

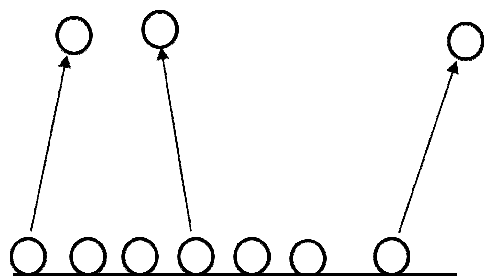

(a) First order

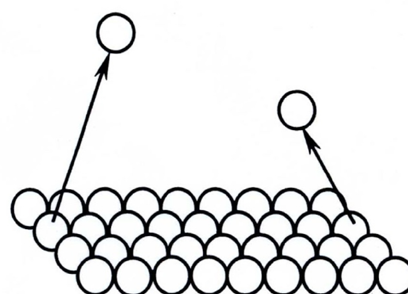

(c) Half order

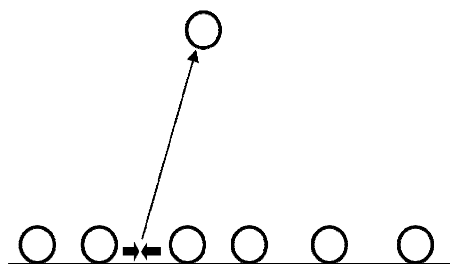

(b) Second order

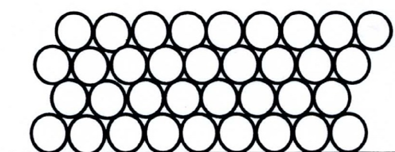

(d) Zero order

Figure 3.8 Schematic representation of various desorption orders from the surface.

3.9 Atomic force microscopy

Atomic force microscopy (AFM) is one of the foremost tools for imaging, measuring, and manipulating matter at the nanoscale. The atomic force microscope was developed to overcome a basic drawback with scanning tunneling microscope (STM) that it can only image conducting or semiconducting surfaces. The AFM, however, has the advantage of imaging almost any type of surface, including polymers, ceramics, composites, glass, and biological samples. The schematic of the microscopic setup of AFM is depicted in Fig. 3.10. In this technique, an atomically sharp tip mounted at the end of a cantilever is scanned across the surface of the sample. When the tip moves up and down over its topography, the displacement caused by the features on the surface can be measured to create an image. The AFM measures the Van der Waals force between the tip and the surface; this may be either the short-range repulsive force (in contact-mode) or the longer-range attractive force (in non-contact mode). There are three scanning modes associated with AFM, namely; contact mode, non-contact mode, and tapping mode. Contact mode is the scanning mode in which the tip is in contact with the surface and the image is obtained by repulsive forces between tip and the sample. In tapping mode, the image is obtained by the tip, which just taps the surface for small periods of time. In non-contact mode, the tip oscillates above the surface, and the image is obtained from the attractive forces between the tip and the sample. The tip is scanned over a surface with feedback mechanisms that enable the piezo-electric scanners to maintain the tip at a constant force (to obtain height information) or height above the sample surface (to obtain force information). As the tip scans the surface of the sample, the focused laser beam is deflected off the attached cantilever into a position sensitive dual photodiode system. Feedback from the dual

photodiode system and the control software enables the tip to maintain either a constant force or constant height above the sample. The surface morphologies of the InN layers in this dissertation were analyzed using a PSIA-XE-100 AFM in both contact and non-contact mode.

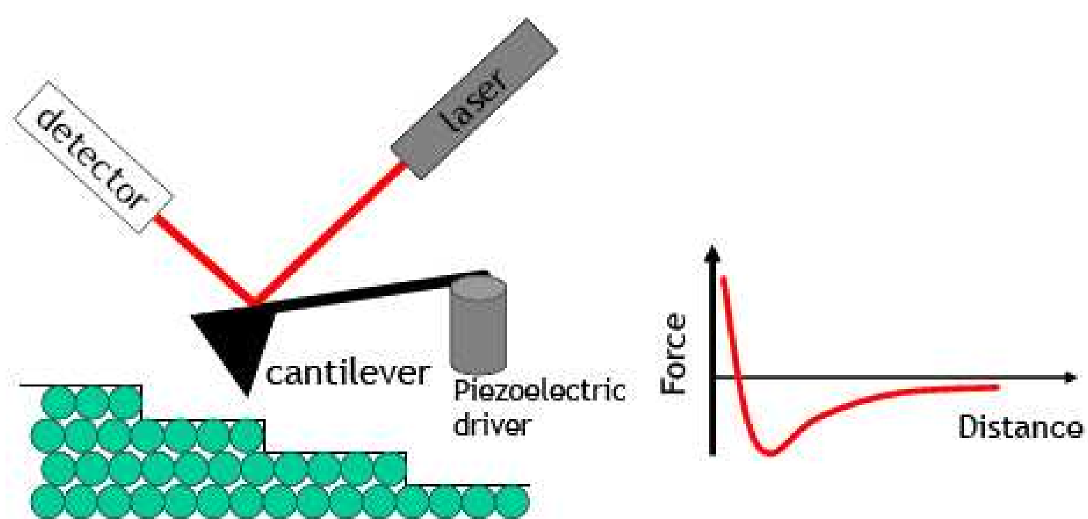

Figure 3.9 Diagram of an atomic force microscopy set up.

3.10 Experimental methods

3.10.1 Sputtering

Since the samples are exposed to the atmosphere prior to the installation in to the UHV chamber, they get contaminated and hence they need to be cleaned before doing any characterization work. One of the effective techniques to remove the surface impurities of the samples is sputtering. Sputtering is the method by which the topmost atomic layers of a sample surface are removed by bombardment with gas ions, typically argon or nitrogen. During the process of cleaning by sputtering, the energetic ion incident on the sample surface transfers its momentum to atom(s) causing its (their) ejection from the surface in the form of neutral, positive, or negative ions [5]. For nitride semiconductors, the sputtering with nitrogen ions is more effective in cleaning and less damaging than that by argon ions [28]. Moreover, sputtering GaN surface with argon ions has been shown to leave a nitrogen deficient surface [29]. Since the cleaning with 1 keV nitrogen ions has been found to leave a contaminant free surface, the samples in this work were sputtered by nitrogen ions.

In order to clean the samples by 1 keV nitrogen ions, sputtering was done with an ion gun. The Kimball Physics ILG-2C ion gun with its matching IGPS-2C power supply was used to produce nitrogen ions. The details of the construction and working of the ion gun can be found in chapter III of V.J. Bellitto's dissertation [1]. The ion gun uses a refractory oxide filament to generate ions by electron impact ionization of background gas or nitrogen gas admitted through a leak valve. The gun can deliver 1 μA into an approximate 1 mm spot, at a 20 mm distance at 1 keV. Both beam energy and beam current are independently adjustable over a wide range. Since the sputtering makes the surface disordered, the ion bombardment is not done directly to avoid

more surface destruction. The samples were bombarded with 1 keV nitrogen ions at 70° from the surface normal.

3.10.2 Atomic hydrogen cleaning

Prior to the installation of sample into the UHV chamber, it needs some cleaning procedures to remove the surface contaminants due to the exposure of the sample to air and other physical contacts. The sample is first cleaned with isopropyl alcohol and inserted into the UHV chamber. In UHV chamber, samples are cleaned by various techniques such as, sputtering with nitrogen ions, heating and exposing atomic hydrogen. It is highly desired to have a cleaning process which can be employed in UHV to remove all oxides, carbides and other contaminations without removing a significant amount of the base semiconductor material. Among the several cleaning processes atomic hydrogen cleaning has been found one of the most efficient techniques to remove contaminants from the sample surface. This technique was first suggested by Prof. McCoville and coworkers at University of Warwick [30]. This technique was employed successfully to remove the oxygen contaminants completely and most of the carbon contaminants from the InN samples grown by high pressure chemical vapor deposition (HPCVD) [31].

A schematic representation of the atomic hydrogen cleaning process is shown in Fig. 3.9. In order to carry out the process of atomic hydrogen cleaning, the upper chamber of UHV system is back filled with molecular hydrogen to a pressure of 8.4×10^{-7} Torr. by opening the leak valve which connects the gas handling system and the upper chamber. The molecular hydrogen passes through a tungsten filament heated to ~ 1575 °C so that it converts molecular hydrogen into atomic hydrogen. The sample is faced towards the heated filament and kept very near to it. The

parameters of sample position are set at x = 5 mm, y = 34 mm, z = 30 mm, and $\theta = 152^{\circ}$. The sample is exposed to hydrogen for 20 minutes which is equivalent to the 1000L exposure of H_2 ($1L = 8.4 \times 10^{-7}$ Torr × 1 sec.). After 20 minutes the sample is heated to 600 K for another 20 minutes keeping the hydrogen exposure on. The exposure of hydrogen is equivalent to another 1000 L. After exposing the sample for a total 40 minutes, the leak valve is closed to stop passing hydrogen in to the UHV chamber. The power of the sample heater is turned off and the sample is pulled back to allow cooling. The power of dosing filament is also turned off. The removal of the surface contaminants is monitored by AES. This process is repeated for few cycles until the removal of contaminants from the sample surface is confirmed.

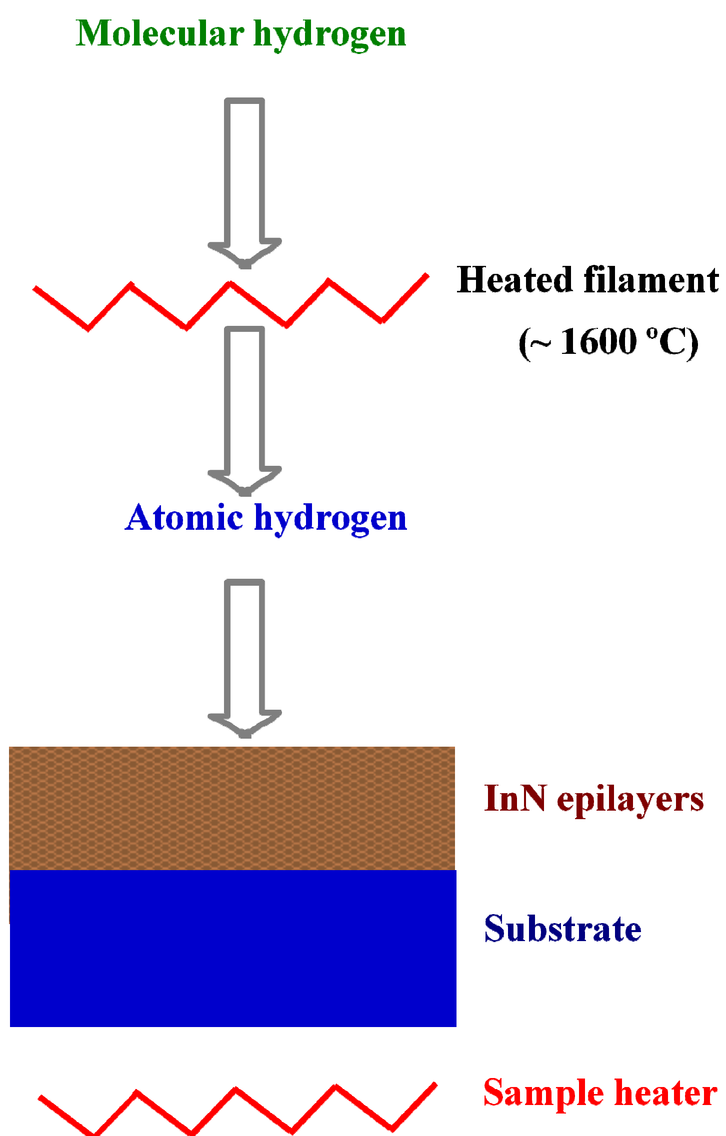

Figure 3.10 Schematic representation of atomic hydrogen cleaning process.

3.10.3 Annealing

As discussed before, sputtering is one of the effective techniques to remove the surface contaminants. However, sputtering results the rough and disordered surface. In order to bring back the well-ordered and smooth surface, annealing has been a useful technique. In addition, after dosing with various gases such as, hydrogen, deuterium, oxygen, etc., the sample is annealed to a different range of temperatures to observe the desorption rate. In order to anneal the sample, the filament at the back of sample mount is heated by passing electric current through it. The sample mount is heated by the bombardment of electrons emitted from the heated filament and the sample is also heated along with the sample mount. The temperature of the sample is measured by a chromel- alumel thermocouple attached on the hot-plate near to the sample. In order to heat the sample, an automatic temperature controlling unit, called the PID (Proportional Integral Differential) temperature controller is used. The PID temperature controller takes the feedback from the thermocouple attached next to the sample and adjusts the heating power by changing only the filament floating voltage to follow the heating profile programmed in it. It responds to the feedback and adjusts the power very efficiently. Heating by the automatic controller is of much better linearity and has a smaller temperature variation than when controlled manually. The typical temperature variation is as low as ±1 °C from the set program.

3.11 Gas handling system

In order to perform the experiments on the interaction of gases with the sample surface, high purity gases are used. For dosing, hydrogen, deuterium and oxygen gases are generally used. For sputtering, either argon or nitrogen gas is used. Our gas handling system consists of a baked metal gas manifold which is equipped to handle gas cylinders. For the gas lines, 1/4” stainless steel tubing is used which is connected to the gas cylinders by manual control valves. Nupro valves isolate the gas manifold from the gas lines. The system is independently pumped with a molecular drag pump. The pressure of the gas handling system is measured with the help of convectron gauge, and the lowest pressure is ~ 1.5×10^{-3} Torr. For dosing and sputtering the sample, gases are delivered into the UHV system through variable leak valves connected to the upper chamber.

3.12 References

[1] V. J. Bellitto, Dissertation, Chapter II, (2000).

[2] M. Alevli, Dissertation, Chapter III, (2008).

[3] A. Zangwill, *Physics at Surfaces*, (Cambridge Univ. Press, Cambridge, 1988).

[4] G. Ertl and J. Küppers, *Low Energy Electrons and Surface Chemistry*, (Verlag Chemie, GmbH, Weinheim, 1974).

[5] J. Hudson, *Surface Science*, (Butterworth- Heinemann, Massachusetts 1992).

[6] P. Auger, J. Phys. Radium **6**, 205 (1925).

[7] I. F. Ferguson, *Auger MicroProbe Analysis*, IOP Publishing, New York (1989).

[8] L. E. Davis, N. C. MacDonald, P. W. Palmberg, G. E. Riach, R. E. Weber, "Handbook of Auger electron spectroscopy" by Physical electronics division, Perkin-Elmer corporation (1978).

[9] D. J. Gardiner, *Practical Raman spectroscopy*, Springer-Verlag (1989).

[10] V. Y. Davydov, and A. A. Klochikhin, Semiconductors **38**, 861 (2004).

[11] M. V. Klein and T. E. Furtac, *Optics*, Wiley, NY (1986).

[12] C. C. Katsidis and D. I. Siapkas, Appl. Optics **41**, 3978 (2002).

[13] W. H. Press, W. T. Teukolsky, W. T. Vetterling, and B. P. Flannery, *Numerical Recipes in C: The art of Scientific Computing*, Cambridge University Press, Cambridge (2003).

[14] H. Ibach and D. L. Mills, *Electron Energy Loss Spectroscopy and Surface Vibrations*, Academic Press, New York (1982).

[15] H. Ibach, Electron Energy Loss Spectrometers, Springer – Verlag, Berlin (1991).

[16] V. Comello, R & D **40**, 63 (1998).

[17] M. L. Tarng, and G. K. Wehner, J. Appl. Phys. **43**, 2268 (1972).

[18] P. W. Palmberg, G. K. Bohn, and J. C. Tracy, Appl. Phys. Lett. **15**, 254 (1969).

[19] M. T. Schulberg, C. A. Fox, G. D. Kubiak, and R. H. Stulen, J. Appl. Phys. **77**, 3484 (1995).

[20] K. Sinniah, M. G. Sherman, L. B. Lewis, W. H. Weinberg, J. T. Yates, Jr., and K. C. Janda, Phys. Rev. Lett. **66**, 567 (1989).

[21] R. E. Thomas, R. A. Rudder, and R. J. Markunas, J. Vac. Sci. Technol. A **10**, 2451 (1992).

[22] Y. L. Yang, L. M. Struck, L. F. Sutcu, and M. P. D'Evelyn, Thin Solid Films **225**, 203 (1993).

[23] K. Bobrov, H. Shechter, M. Folman, and A. Hoffman, Diamon Relat. Mater. **7**, 170 (1998).

[24] K. Bobrov, H. Shechter, M. Folman, and A. Hoffman, Diamon Relat. Mater. **8**, 705 (1999).

[25] C. H. Kuo, C. Choi, G. N. Maracas, T. C. Steimle, J. Vac. Sci. Technol. B **11**, 833 (1993).

[26] A. R. Acharya, S. Gamage, M. K. I. Senevirathne, M. Alevli, K. Bahadir, A. G. Melton, I. Ferguson, N. Dietz, and B. D. Thoms, Appl. Surf. Sci. **268**, 1 (2013).

[27] P. A. Redhead, Vacuum **12**, 203 (1962).

[28] R. W. Hunt, L. Vanzetti, T. Castro, K. M. Chen, L. Sorba, P. I. Cohen, W. Gladfelter, J. M. Van Hove, J. N. Kuznia, M. A. Khan, and A. Franciosi, Physica B **185**, 415 (1993).

[29] H. Ishikawa, S. Kobayashi, Y. Koide, S. Yamasaki, S. Nagai, J. Umezaki, M. Koike, M. Murakami, J. Appl. Phys. **81**, 1315 (1997).

[30] L. F. J. Piper, T. D. Veal, M. Walker, I. Mahboob, C. F. McConville, H. Lu, and W. J. Schaff, J. Vac. Sci. & Technol. A **23** (4), 617 (2005).

[31] R. P. Bhatta, B. D. Thoms, M. Alevli, V. Woods, and N. Dietz, Appl. Phys. Lett. **88**, 122112 (2006).

4 OBSERVATION OF NH_2 SPECIES ON TILTED INDIUM NITRIDE($01\bar{1}1$) FACETS

4.1 Abstract

The structural properties and surface bonding configuration of InN layers grown by high pressure chemical vapor deposition (HPCVD) have been characterized using Raman spectroscopy, x-ray diffraction (XRD) and high resolution electron energy loss spectroscopy (HREELS). The appearance of the A_1(TO) mode at 447 cm^{-1} in un-polarized $z(..)\bar{z}$ Raman spectrum indicates distortions in the crystal lattice due to the growth of tilted plane crystallites. A Bragg reflex in the x-ray diffraction spectrum at $2\Theta \approx 33^0$ has been assigned to tilted InN facets in the polycrystalline InN layer. The HREEL spectrum for this InN layer features vibration modes assigned to NH_2 species indicating a surface orientation consistent with the crystalline properties observed in Raman spectroscopy and XRD. The appearance of tilted planes is suggested to be due to the effects of a high V-III ratio and lattice mismatch on the growth mechanism.

4.2 Introduction

Since the first attempt to synthesize InN by Juza and Hahn in 1938 [1], the interest in studying and understanding the revised physical properties of InN have been growing significantly due to its highly attractive optoelectronic properties. During the last 10 years, it has been shown that InN is a narrow band gap semiconductor (~0.7eV) with potential for a wide range of applications including chemical and biological sensors [2], high electron mobility transistors [3], multi-junction tandem solar cells [4], thermoelectric devices [5] and terahertz radiation devices [6]. InN is the binary corner for ternary (InGaN and InAlN) and quaternary (InGaAlN) group III-nitride alloys, which are presently explored for frequency agile detectors

and emitters operating from ultraviolet (UV) to near infrared (IR) region. For instance, along with GaN, ternary InGaN alloys are integrated in a variety of heterostructure-based optoelectronic devices, such as LEDs [7, 8], laser diodes [9], or in unique detectors that cover the wavelength regime from UV down to the far IR [10]. InN is predicted to have the lowest effective electron mass of all III–nitride semiconductors [11], enabling device elements with high mobility and high saturation drift velocity.

The growth of high crystalline quality InN and indium-rich group III-nitride alloys remains a challenge-mainly due to the low dissociation temperature of InN. Thermal dissociation can be avoided by growing at low enough temperatures, about 600 ^{0}C for low-pressure chemical vapor deposition (LPCVD) [12]. The cracking efficiency of ammonia in this temperature regime is extremely low, requiring a large group V-III precursor ratio [13]. Highly volatile compounds, such as InN and related alloys, can be grown at much higher temperatures if surface stabilization is done at high pressures [14, 15]. In order to stabilize InN growth at elevated temperatures, high-pressure chemical vapor deposition (HPCVD) has been found to be an effective technique for producing high quality III-N layers [13].

Growth of III-nitride based semiconductors in the c-direction may be preferred because of the cost effective fabrication of the devices. However, due to the lattice geometry and the induced strain, large piezoelectric fields are present within the heterostructure [16]. In optoelectronic devices, the spontaneous and piezoelectric polarizations affect the internal quantum efficiency of the quantum well structures [17]. Despite the present difficulty in the device fabrication, new approaches have been explored, e.g., growth on tilted or various non-polar (a-, r- and m-) planes [18, 19]. It has been shown that layers grown on a- or m-plane increase the efficiency of the devices as the polarization effects are minimized. Ahn *et al.* [20]

reported two orders of magnitude increase in the terahertz emission from a-plane compared to c-plane InN.

Other properties such as stability are also affected by the surface orientation of InN layers. Naoi *et al.* have reported that the In-polar surface is chemically more stable whereas the N-polar surface is thermally more stable [21]. They suggest that differences in chemical reactivity and stability for InN surfaces are related to differences in work function. Similar studies of chemical and thermal stability have not yet been reported for non-polar or mixed polarity InN planes.

This work uses Raman spectroscopy, XRD and HREELS to characterize the structure and bonding properties of an HPCVD-grown InN layer exhibiting tilted facets. In addition, the relationship of the growth conditions to the production of tilted facets on the InN surface is discussed.

4.3 Experimental methods

The InN layer analyzed in this work was grown by HPCVD at a growth temperature of 865 °C, a reactor pressure of 15 bar, and an ammonia (NH_3) to trimethylindium (TMI) precursor ratio of 3000. The layer was deposited directly on a sapphire(0001) substrate. In the previous work, studies on InN layers grown on GaN buffer layers on a sapphire(0001) leading to c-plane orientation of the layers were reported [22]. Details of the HPCVD reactor, the growth configuration, and the real-time optical characterization techniques employed have been published elsewhere [13, 23, 24].

For Raman analysis, an excitation source of 532 nm (2.33 eV) was used. The Raman spectrometer consists of a McPherson double subtractive monochromator and a single 2m

monochromator system. The Raman measurements were carried out in back scattering geometry. The ω-2Θ XRD results were obtained utilizing an X`Pert PRO MPD (Philips) 4-circle diffractometer equipped with a monochromatic x-ray (Cu-K_α) source. The sample was aligned prior to the measurements utilizing the substrate's sapphire(0006) Bragg reflex. HREELS, a surface sensitive vibrational technique, was performed in a stainless-steel ultrahigh vacuum (UHV) system with a base pressure of 2×10^{-10} Torr. Bellitto *et al.* have reported the details of the UHV system and sample mount [25]. The sample was cleaned with acetone and rinsed with isopropyl alcohol before insertion into the UHV chamber. Inside the UHV chamber, the sample was cleaned by a procedure of bombardment with 1 keV nitrogen ions followed by atomic hydrogen cleaning (AHC), which was demonstrated as an effective way to remove surface contaminants by Piper *et al.*[26]. The removal of surface contaminants (carbon, oxygen) was confirmed by Auger electron spectroscopy (AES). Atomic hydrogen cleaning was performed by backfilling the vacuum chamber with hydrogen to a pressure of 8.4×10^{-7} Torr in the presence of a tungsten filament heated to 1575 °C to produce H-atoms. The sample was kept at 20 mm from the dosing filament for 5 minutes (giving an exposure of 250 L of hydrogen, 1 L= 1×10^{-6} Torr.s). During this time the sample temperature increased to 60 °C due to the heated dosing filament. After 5 minutes, the sample was heated to 350 °C by the bombardment of the electrons from the back of the sample mount for 10 minutes while H atom exposure continued (giving an additional exposure of 500 L of hydrogen). HREELS experiments were performed in a specular geometry with an incident and scattered angle of 60^0 from the surface normal, and an incident electron beam energy of 5.6 eV.

4.4 Results and discussion

The Raman spectrum for the InN layer is shown in Fig. 4.1. The prominent peak at 592.5 cm^{-1} is assigned to the A_1(LO) vibration mode [27]. The broad peak between 405 cm^{-1} and 540 cm^{-1} is deconvoluted to resolve into four significant components using Gaussian line shape analysis as depicted in Fig. 4.1, with parameters summarized in Table 4.1. The largest peak contribution centered at 489.6 cm^{-1} has been assigned to E_2(high) [27, 28]. The Raman mode centered at 449.6 cm^{-1} has been assigned to A_1(TO) and the peak centered at 470.4 cm^{-1} has been assigned to E_1(TO) modes [27, 29]. From the Raman selection rules, however, the mode pairs A_1(LO)-E_2(high) and A_1(TO)-E_1(TO) are forbidden in the same plane. Thus, the observation of all these modes in the Raman spectrum indicates that the layer contains grain facets tilted against the direction of the incident beam, i.e., the growth direction.

In addition, the weak Raman feature centered at 515.2 cm^{-1} (denoted by β in Fig. 4.1) belongs neither to any known InN modes nor to any sapphire substrate related mode of vibration. One possible explanation for this feature might be a second order Raman effect of the B_1(low) mode. However, Dhara *et al*. [30] have interpreted a feature at the same spectral position to a disorder assisted longitudinal optical (DALO) mode.

The x-ray diffraction spectrum for the InN layer recorded in ω-2Θ-geometry is shown in Fig. 4.2. The XRD spectrum shows a dominant hexagonal InN(0002) Bragg reflex at 31.24° with a FWHM of 536 arcsec, corresponding to a c-lattice constant of 5.722Å. Two additional Bragg reflexes are observed, centered at 32.8° and 33.06°. Shubina *et al.* [31] assigned the “anomalous” peak in x-ray diffraction pattern at $2\Theta \approx 33°$ to metallic indium. However, Yu *et al*. [32] later suggested that the “anomalous” 33° peak might be related to the diffraction peak of polycrystalline InN. Our studies found that the peak centered at 32.86° can be assigned to

residual metallic indium at the surface, related to the In(101) Bragg reflex (2.723Å) with a FWHM of 428 arcsec. The indium on the surface can be removed by 2 min. wet etching in HCl after which the In(101) Bragg reflex at 32.86° is not observed anymore. In agreement with a previous report by Yu *et al.*, the second peak located at 33.06° (2.707Å) with a FWHM of 636 arcsec is attributed to tilted crystallites exposing InN ($01\bar{1}1$) facets [32].

Previous HREELS studies by the authors on InN epilayers grown on GaN/sapphire templates [33-35] showed a strong loss feature at 550 cm^{-1}, which has been assigned to a Fuchs-Kliewer surface phonon. The loss peak at 3260 cm^{-1} for the atomic hydrogen cleaned (AHC) surface was assigned to an N-H stretching vibration, while the loss feature at 870 cm^{-1} was assigned to an N-H bending vibration. From these observations it was concluded that the InN film in that previous work was N-polar and N-H terminated. In one study, a broad loss feature was assigned to a conduction band plasmon excitation and spectra acquired as a function of incident energy revealed the presence of a surface electron accumulation [34].

In the present work, a HREEL spectrum was acquired from the InN sample after atomic-hydrogen cleaning and is shown in Fig. 4.3. Vibrational loss features are observed at 640 cm^{-1}, 1260 cm^{-1}, 1440 cm^{-1}, 1600 cm^{-1}, 2960 cm^{-1}, 3400 cm^{-1} and 3710 cm^{-1}. However, no loss features related to a conduction band plasmon are observed at loss energies up to 4500 cm^{-1} indicating the layer has a relatively high carrier concentration.

The loss peaks at 1260, 1600 and 3400 cm^{-1} indicate that the dominant surface species is NH_2 as opposed to the NH observed in the earlier work [33-35]. The loss feature at 3400 cm^{-1} is assigned to an NH_2 stretching vibration in agreement with that assigned by Tanaka *et al.* [36] for NH_2 symmetric stretching vibration on InP(110). The loss features at 1260 cm^{-1} and at 1600 cm^{-1} are assigned to NH_2 wagging and scissor modes of vibration which have close agreement with

those assigned by Tindall *et al.* [37] on Ge(100). Bhatta *et al.* [35] reported a strong but sharp loss feature at 550 cm^{-1} on InN($000\bar{1}$) which they assigned to Fuchs-Kliewer surface phonon and Tindall *et al.* [37] reported a rocking mode of NH_2 vibration at 884 cm^{-1}. Instead of these two individual loss features, a strong and broad loss feature has been observed at 640 cm^{-1} in this work. This strong and broad loss feature is assigned to the unresolved overlap of the Fuchs-Kliewer surface phonon and the rocking mode of the NH_2 vibration. A small C-H stretch vibrational peak is observed at 2960 cm^{-1} due to residual carbon. Though no carbon was seen in AES after a few cycles of sputtering followed by atomic hydrogen cleaning, the HREEL spectrum shows a little carbon contaminant on the surface since HREELS is more sensitive than AES. Small loss features at 1440 cm^{-1} and at 3710 cm^{-1} have been assigned to the bending mode of C-H and the stretching mode of O-H, respectively. Nienhaus *et al.* [38] reported the InH stretching vibration at 1650-1700 cm^{-1} in HREELS experiments and at 1630-1650 cm^{-1} from *ab initio* calculations [39] on InP surfaces. However, no loss feature in this range was observed in the present work indicating no surface InH exists on the atomic hydrogen cleaned surface. HREELS spectra (not shown) were also taken from the sample dosed with hydrogen at temperature as low as 60 ^{0}C. But no loss feature related to InH was observed in the HREEL spectra. Although surface metallic indium was indicated in XRD, the sample was sputtered to remove contaminants before taking the HREELS measurements which showed no indium-related vibrations on the surface. The various loss features and their assignments have been summarized in Table 4.2.

The Raman spectroscopic analysis indicates the existence of non c-plane crystallites at or near the InN surface. The existence of such non c-plane crystallites is further supported by XRD results, which show the presence of tilted ($01\bar{1}1$) InN facets [32]. Similarly, the observation of

NH_2 rather than NH surface species indicates a non c-plane surface orientation. In the wurtzite structure $(01\bar{1}1)$ facets are semi-polar and both In and N atoms would be expected to be present at the surface. However, in the HREEL spectrum no loss features attributable to InH are observed but only NH_2 vibrations. It is suggested that surface indium atoms are either not present or not available for reaction with atomic hydrogen. No surface reconstruction was observed in low energy electron diffraction due to the polycrystalline nature of the layer. If indium atoms were present and reactive, exposure to atomic hydrogen near room temperature should have produced InH vibrations in HREELS. From the HREELS spectrum, it can be concluded that the presence of NH_2 species on InN layer is due to the tilted facets, consistent with the XRD and Raman spectroscopy results.

It is expected that the presence of tilted planes may change the piezoelectric polarization properties of the surface as well as any surface electron accumulation [40,41]. Both of these effects may impact the properties of heterojunction interfaces or metallic contacts. The predominance of NH_2 species on the surface, in contrast to the NH termination observed on c-plane oriented layers, suggests that these tilted planes are likely to also exhibit differences in surface chemistry that can affect growth and processing.

The growth of tilted planes and the appearance of NH_2 related vibrational modes on the surface may be due to the growth of microcrystals associated with a 3D crystal growth mode. Two possible reasons reported for the 3D growth of InN are insufficient adatom surface diffusion due to nitrogen-rich growth conditions, i.e., high V/III ratio condition, and strain produced by lattice mismatch between InN and the substrate [42]. In previous studies of HPCVD-grown InN layers by the authors [33-35], c-plane orientation was observed from layers grown on GaN buffer layers on the sapphire substrate (lattice mismatch between GaN and InN ~ 10%). In the present

work, growth occurred directly on sapphire with no buffer layer (lattice mismatch between InN and sapphire ~ 29%). The strain due to the larger lattice mismatch may be a cause for the growth of tilted crystallites. However, the V-III precursor ratio may also be a contributing factor. The c-plane oriented layers in the author's previous work were grown with lower ammonia to TMI ratios (as low as 630) than the layer exhibiting tilted planes studied in the present work (ammonia to TMI ratio of 3000). Other parameters, such as, pressure, temperature, and precursor flow rate were similar between the present work and the previous studies. When V/III ratio is high, there is insufficient adatom surface diffusion due to nitrogen-rich growth conditions. Lattice mismatch may lead to the formation of 3D islands during epitaxy to relieve the film strain [42]. The present work suggests that sapphire substrate and high NH_3 to TMI ratio are key factors for the growth of InN layers in different orientations other than c-plane.

The present work shows correlations between characterizations of surface and bulk structure and bonding on InN($01\bar{1}1$) facets but additional work is needed to investigate the effects on interface and device properties. Since the performance of InN based devices depends upon the surface orientation, the study of chemical reactivity and thermal stability on the tilted planes may be of importance. In the authors' research group the study of surface reactions and thermal stability on the tilted InN planes is in progress.

4.5 Conclusion

In summary, the structural properties of an InN layer grown on sapphire was studied by Raman spectroscopy, XRD and HREELS. The Raman analysis shows the appearance of both mode pairs, A_1(LO)-E_2(high) and A_1(TO)-E_1(TO), due to the presence of tilted InN facets in the layer. XRD shows an additional Bragg reflex at 33.06° supporting the presence of tilted ($01\bar{1}1$)

InN crystallites. The tilted orientation of the crystals results in an InN surface mainly consisting of NH_2 species as observed in HREELS in contrast to the NH vibrations observed from the InN($000\bar{1}$) surface. Growth of tilted planes in InN is a consequence of a 3D growth mode suggested to be due to the high V/III ratio and large lattice mismatch with the sapphire substrate.

Table 4.1 Raman spectroscopy results and assignments.

Symmetry Mode	Literature Value[27] Center peak pos. (cm^{-1})	Literature Value[29] Center peak pos. (cm^{-1})	Experimental Value Center peak pos. (cm^{-1})
A_1 (TO)	443	445	449.6
E_1 (TO)	477	472	470.4
E_2^H	491	488	489.6
β	-	-	515.2
A_1 (LO)	590	588	592.5

Table 4.2 HREELS vibrational frequencies and assignments from InN.

Frequency (cm^{-1})	Assignment
640	Fuchs-Kliewer phonon + NH_2 rock
1260	NH_2 Wag
1440	C-H bend
1600	NH_2 Scissor
2960	C-H stretch
3400	NH_2 stretch
3710	O-H stretch

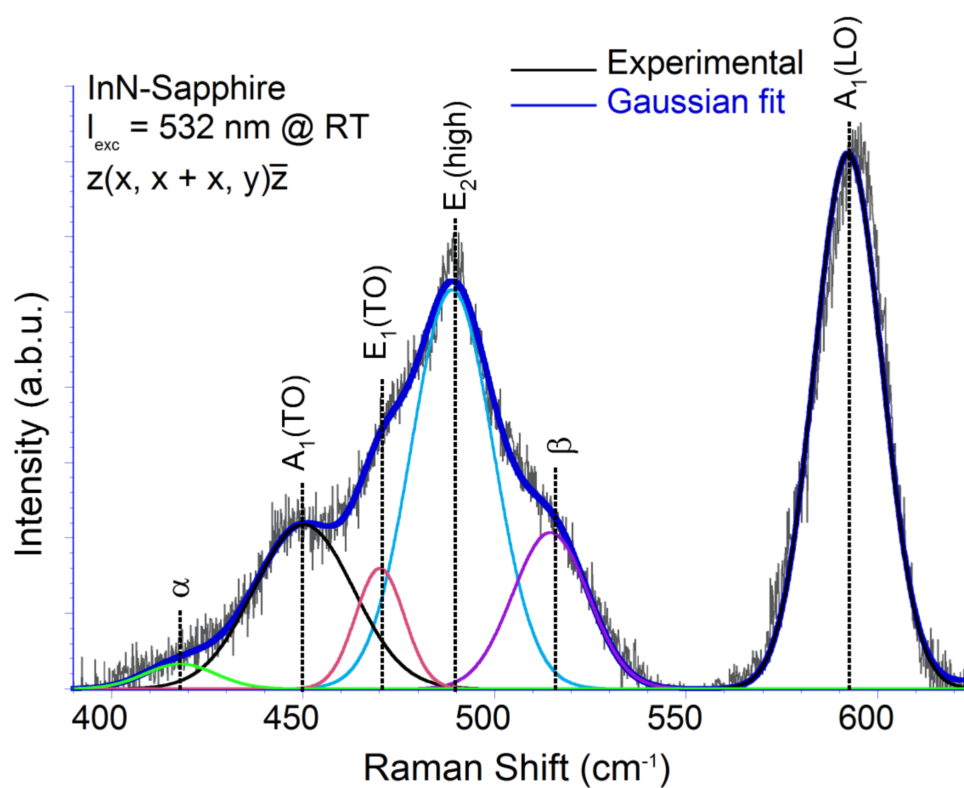

Figure 4.1 Raman spectrum of an InN layer grown on sapphire with deconvolution of the Raman modes using Gaussian curves.

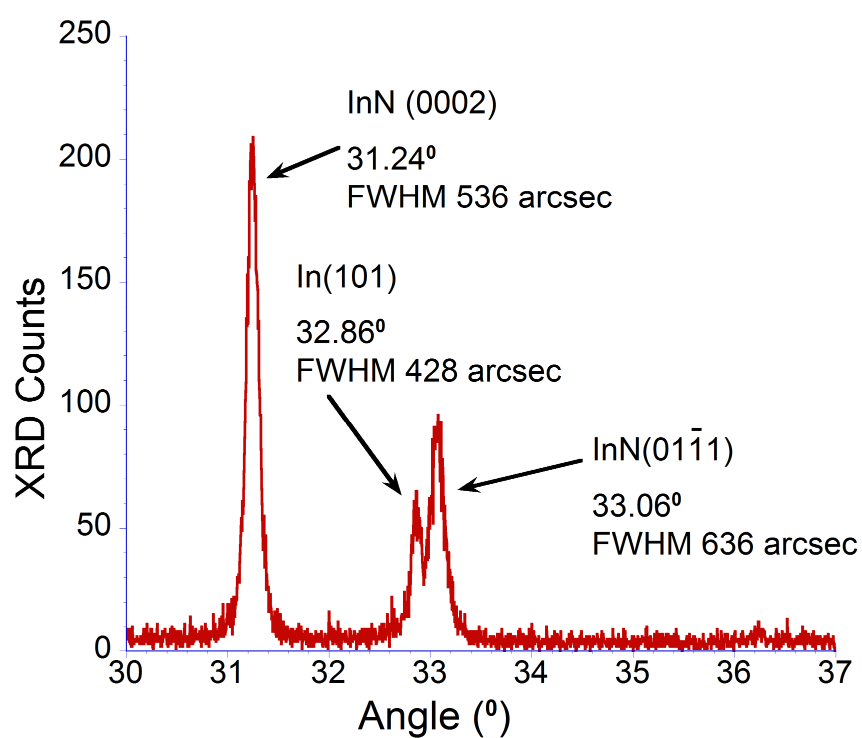

Figure 4.2 X-Ray diffraction results of HPCVD-grown InN in ω-2Θ-geometry.

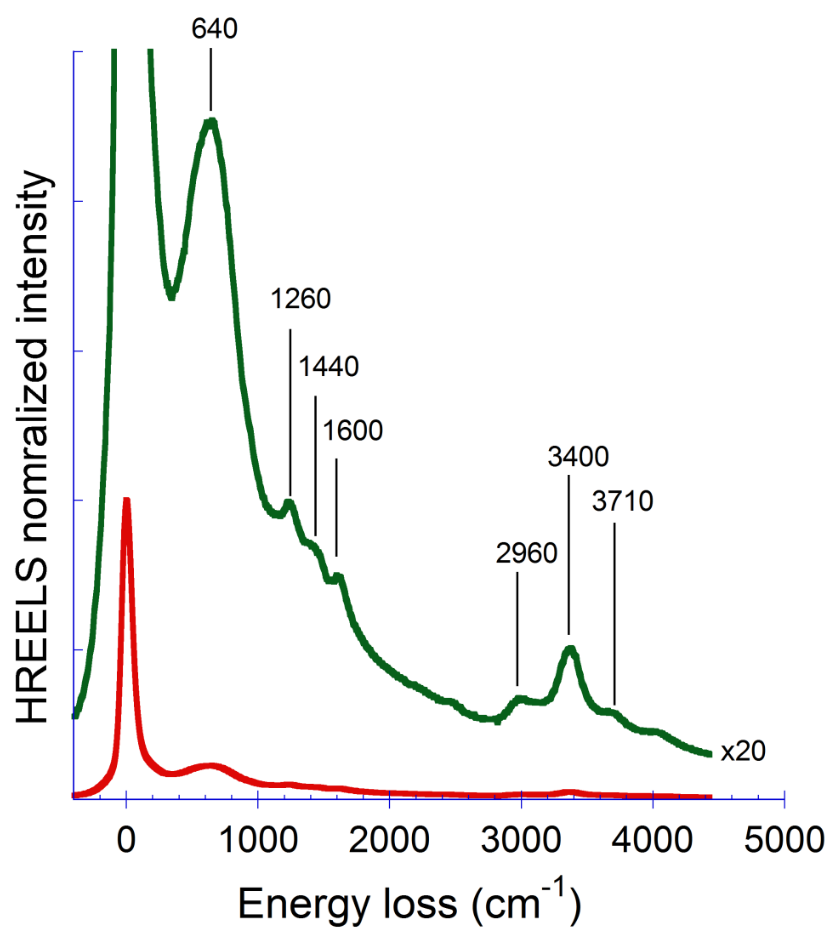

Figure 4.3 HREEL spectra of HPCVD-grown InN after atomic hydrogen cleaning.

4.6 References

[1] R. Juza and H. Hahn, Z. Anorg. Allg. Chem. **239**, 282 (1938).

[2] H. Lu, W.J. Schaff, L.F. Eastman, J. Appl. Phys. **96**, 3577 (2004).

[3] M. Singh, J. Singh, J. Appl. Phys. **94**, 2498 (2003).

[4] A. Yamamoto, Md. R. Islam, T. Kang, and A. Hashimoto, Phys. Stat. Sol. (c) **7**, 1309 (2010).

[5] S. Yamaguchi, R. Izaki, N. Kaiwa, S. Sugimura, A. Yamamoto, Appl. Phys. Lett. **84,** 5344 (2004).

[6] Y. M. Meziani, B. Maleyre, M. L. Sadowski, S. Ruffenach, O. Briot, W. Knap, Phys. Stat. Sol. (a) **202**, 590 (2005).

[7] I. Akasaki, H. Amano, N. Koide, M. Kotaki, and K. Manabe, Physica B **185**, 428 (1993).

[8] S. Nakamura, M. Senoh, and T. Mukai, Jpn. J. Appl. Phys. **32**, L8 (1993).

[9] S. Nakamura, M. Senoh, S. Nagahama, N. Iwasa, T. Yamada, T. Matsushita, H. Kiyoku, and Y. Sugimoto, Jpn. J. Appl. Phys. **35**, L74 (1996).

[10] M. Buegler, M. Alevli, R. Atalay, G. Durkaya, I. Senevirathna, M. Jamil, I. Ferguson, and N. Dietz, Proc. SPIE **7422**, 742218 (2009).

[11] S. N. Mohammad and H. Morkoc, Prog. Quantum Electron. **20**, 361 (1996).

[12] A. G Bhuiyan, A. Hashimoto, and A. Yamamoto, J. Appl. Phys. **94** , 2779 (2003).

[13] N. Dietz, M. Strassburg, and V. Woods, J. Vac. Sci. Technol. A **23**, 1221 (2005).

[14] J. MacChesney, P. M. Bridenbaugh, and P. B. O'Connor, Mater. Res.Bull. **5**, 783 (1970).

[15] N. Dietz, in *III-Nitrides Semiconductor Materials*, edited by Z. C. Feng Imperial College Press, 203 (2006).

[16] S. Schwaiger, F. Lipski, T. Wunderer, and F. Scholz, Phys. Stat Sol. (c) **7**, No.7-8, 2069 (2010).

[17] P. Lefebvre, A. Morel, M.Gallard, T. Talierco, J. Allegre, B. Gil, H. Mathieu, B. Damilano, N. Grandjean, and J. Massies, Appl. Phys. Lett. **78**, 1252 (2001).

[18] P. Waltereit, O. Brandt, A. Trampert, H. T. Grahn, J. Menniger, M. Ramsteiner, M. Reiche, and K. H. Ploog: Nature **406**, 865 (2000).

[19] K. Kusakabe, S. Ando, K. Ohkawa, J. Cryst. Growth **298**, 293 (2007).

[20] H. Ahn, Y. P. Ku, C. H. Chuang, C. L. Pan, H. W. Lin, Y. L. Hong, and S. Gwo, Appl. Phys. Lett. **92**, 102103 (2008).

[21] H. Naoi, D. Muto, T. Hioka, Y. Hayakawa, A. Sujuki, T. Araki, and Y. Nanishi, Phys. Stat. Sol. (b) **244**, 1834 (2007).

[22] R. P. Bhatta, B. D. Thoms, M. Alevli, and N. Dietz, Surf. Sci. **602**, 1428 (2008).

[23] N. Dietz, M. Alevli, V. Woods, M. Strassburg, H. Kang, and I. T. Ferguson, Phys. Stat. Sol. (b) **242**, 2985 (2005).

[24] V. Woods and N. Dietz, Mater. Sci. Eng., **B 127**, 239 (2006).

[25] V. J. Bellitto, B. D. Thoms, D. D. Koleske, A. E. Wickenden, R. L. Henry, Surf. Sci. **430**, 80 (1999).

[26] L. F. J. Piper, T. D. Veal, M. Walker, I. Mahboob, C. F. McConville, H. Lu, and W. J. Schaff, J. Vac. Sci. Technol. A **23**, 617 (2005).

[27] A. Kasic, M. Schubert, Y. Saito, Y. Nanishi, and G. Wanger, Phys. Rev B **65**, 115206 (2002).

[28] T. Inushima, T. Shiraishi, and V. Yu. Davydov, Solid State Commun. **110**, 491 (1999).

[29] J. S. Dyck, K. Kim, S. Limpijumnong, W. R. L. Lambrecht, K. Kash, and J. C. Angus, Solid state commun. **114**, 355 (2000).

[30] S. Dhara, P. Magudapathy, R. Kesavamoorthy, S. Kalavathi, V. S. Sastry, K. G. M. Nair, G. M. Hsu, L. C. Chen, K. H. Chen, K. Santhakumar , and T. Soga, Appl. Phys. Lett. **88**, 241904 (2006).

[31] T. V. Shubina, S. V. Ivanov, V. N. Jmerik, D. D. Solnyshkov, V. A. Vekshin, P. S. Kop'ev, A. Vasson, J. Leymarie, A. Karvokin, H. Amano, K. Shimono, A. Kasic, and B. Monemar, Phys. Rev. Lett. **92**, 117407 (2004).

[32] K. M. Yu, Z. Lilintal-Weber, W. Walukiewicz, W. Shan, J. W. Ager lll, S. X. Li, R. E. Jones, E. E. Haller, H. Lu, and W. J. Schaff, Appl. Phys. Lett. **86**, 071910 (2005).

[33] R. P. Bhatta, B. D. Thoms, M. Alevli, V. Woods, and N. Dietz, Appl. Phys. Lett. **88**, 122112 (2006).

[34] R. P. Bhatta, B. D. Thoms, M. Alevli, and N. Dietz, Surf. Sci. **601**, L120 (2007).

[35] R. P. Bhatta, B. D. Thoms, A.Weerasekera, A. G. U. Perera, M. Alevli, and N. Dietz, J. Vac. Sci. Technol.A **25**, 967 (2007).

[36] S. Tanaka, M. Onchi, and M. Nishijima, Surf.Sci.**191**, L756 (1987).

[37] C. Tindall, and J. C. Hemminger, Surf. Sci. **330**, 67 (1995).

[38] H. Nienhaus, S. P. Grabowski, and W. Monch, Surf. Sci. **368**, 196 (1996).

[39] J. Fritsch, A. Echert, P. Pavone, and U. Schroder, J. Phys.: Condens. Matter **7**, 7717 (1995).

[40] C. G. Van de Walle and D. Segev , J. Appl. Phys. **101**, 081704 (2007).

[41] V. Darakchieva, M. Schubert, T. Hofmann, B. Monemar, Ching-Lien Hsiao, Ting-Wei Liu, Li-Chyong Chen, W. J. Schaff, Y. Takagi, and Y. Nahishi, Appl. Phys. Lett. **95**, 202103 (2009).

[42] B. Liu, T. Kitajima, D. Chen, and S. R. Leone, J. Vac. Sci. Technol. A **23 (2)**, 304 (2005).

5 THERMAL STABILITY OF INDIUM NITRIDE EPILAYERS GROWN BY HIGH PRESSURE CHEMICAL VAPOR DEPOSITION

5.1 Abstract

The thermal stability of InN layers grown on sapphire by high-pressure chemical vapor deposition has been studied by thermal desorption, atomic force microscopy, x-ray diffraction, and infrared reflection measurements. Desorption products from samples grown with group V/III precursor ratios from 1200 to 4800, but otherwise identical growth conditions, have been monitored using differentially-pumped mass spectrometry while the sample temperature was ramped from room temperature to 825 °C. No significant desorption of nitrogen from the surface was observed below 630 °C, with a rapid increase of desorption of molecular nitrogen at substrate temperatures above 630 °C. No significant desorption of NH or NH_2 fragments was observed. From Arrhenius plots, the activation energy for desorption of nitrogen was found to be 1.6 ± 0.2 eV. It was observed that the activation energy for the desorption of nitrogen from InN samples was independent of V/III precursor ratio. However, the temperature corresponding to the maximum desorption was found to be dependent on V/III precursor ratio, increasing from 749 °C for V/III precursor ratio of 1200 to 776 °C for V/III precursor ratio of 4800. The observed shift in the peak desorption temperature with increasing group V/III precursor ratio is attributed to the decrease in extended defects and the increase in grain size.

5.2 Introduction

Due to the low band gap and unique optoelectronic properties of InN, the binary cornerstone InN has attracted renewed attention in the development of group III-nitride based

materials structures and device elements. The band gap energy of InN has been reported to be as low as 0.7 eV [1], which enables the utilization of the group III-nitride material system to a host of potential optoelectronic device structures such as light-emitting diodes operating from near-infrared to deep ultraviolet [2] or high efficiency photovoltaic solar cells [3]. Among the III-nitride semiconductors InN has the highest measured electron mobility, exceeding 3500 cm^2/Vs at room temperature [4]. Recent theoretical calculations using ensemble Monte Carlo methods have predicted that the room temperature electron mobility of InN may be as high as 14000 cm^2/Vs [5]. This exceptional electronic transport property is most favorable for high speed electronic devices and hence InN could be an ideal material for high electron mobility transistors. In addition, InN has a potential for a wide range of applications including chemical and biological sensors [6] as well as thermoelectric devices [7] and terahertz radiation devices [8].

Despite having a number of remarkable physical properties, the utilization of InN is hampered by a limitation in the growth of high-quality InN by chemical vapor deposition (CVD) due to thermal instability and inconsistent surface morphologies. One of the ways to avoid thermal dissociation is to grow InN epilayers at low temperature. But at low temperature the cracking efficiency of ammonia precursor is extremely low, requiring a large group V/III precursor ratio for low-pressure CVD growth [9]. It has been reported that InN and related alloys can be grown at much higher temperatures through surface stabilization at higher reactor pressures [9]. High-pressure chemical vapor deposition (HPCVD) has been shown to be a viable approach to produce high quality III-N epilayers [9].

In recent decades several research groups explored the epitaxial growth of InN layers using techniques such as plasma-assisted molecular beam epitaxy (PA-MBE), low- and high-

pressure metal organic chemical vapor deposition (MOCVD), and hydride vapor phase epitaxy (HVPE). Fewer studies have been done on the thermal stability and decomposition behavior of the InN epilayers [10-14] than have been reported for electronic, structural and optical properties. Thermal stability is very important factor in the growth process as well for the device performance and life time. However, these studies have shown inconsistent results for the decomposition activation energy ranging from 1.15 eV to 3.4 eV. Huang *et al*. [10] studied the thermal stability of MOCVD-grown InN in a nitrogen environment using in-situ laser reflectance. The reported activation energy and onset temperature of nitrogen desorption were 2.1 ± 0.1 eV and 500 °C respectively. Togashi *et al.* [11] studied the temperature dependent decomposition of HVPE grown N-polar InN in a nitrogen ambient. The estimated values of the activation energy and onset temperature of nitrogen desorption were 3.33 eV and 610 °C respectively. In another study [12] the same authors observed a polarity dependent activation energy when the samples were annealed in hydrogen ambient. In that work N-polar InN displayed an activation energy of 1.10 eV and desorption onset temperature was 350 °C while In-polar InN showed an activation energy of 1.74 eV. These results indicate that the decomposition of InN is enhanced by the presence of hydrogen and the activation energy is dependent on growth direction. Ambacher *et al.* [13] performed experiments on the decomposition of low pressure chemical vapor deposition (LPCVD)-grown InN. The sample was put in a quartz tube evacuated to less than 1.5×10^{-8} Torr and the desorbed species were measured with a quadrupole mass spectrometer (QMS). Desorption spectra were measured by heating samples inside the quartz tube with a linear temperature ramp (20 °C/min) from room temperature to 1100 °C. From the Arrhenius plot, the calculated activation energy was 3.48 eV and the observed onset of nitrogen desorption temperature was 630 °C. Koblmüller *et al.* [14] studied the thermal

instability of InN (0001) grown by PA-MBE, monitoring the indium desorption under vacuum conditions using QMS. From their analysis, different values of the activation energy were found for two temperature regimes, lower temperature (560 – 595 °C) and higher temperature (605 – 645 °C). In higher temperature regime, the reported value of the activation energy was 1.15 eV whereas in lower temperature regime, the activation energy was measured to be 4.4 eV and the onset of temperature for InN decomposition was 560 °C. The reported variation in the activation energy of InN epilayers indicates a strong influence of the growth process on the thermal stability and physical properties of InN, motivating our studies on the thermal stability of InN samples grown under HPCVD conditions. In this paper, we report the results of an investigation of the thermal stability of HPCVD-grown InN epilayers by temperature programmed desorption including a determination of the activation energy for molecular nitrogen evolution.

5.3 Experimental methods

The indium nitride (InN) epilayers studied in this work were grown on sapphire substrates at a temperature of 832 °C and a reactor pressure of 15 bar. Ammonia (NH_3) and trimethylindium (TMI) were used as group-V and group-III precursors, respectively. The precursors were embedded into a nitrogen carrier gas stream. In order to avoid gas phase reactions during the growth process they were injected separately by pulsed injection which was temporally controlled, maintaining a constant reactor pressure at all times. The carrier gas flow was adjusted so that the gas flow velocity above the sample surface was kept constant. Details of the HPCVD reactor system, the growth configuration, as well as real-time optical characterization techniques employed have been published elsewhere [15, 16]. The four InN

samples discussed in this work were grown under identical process conditions and growth duration, varying only the group V/III precursor ratio from 1200 to 4800.

Infrared (IR) reflection measurements were performed at room temperature over the frequency range of 450–7000 cm^{-1} using a fast Fourier transform infrared spectrometer and mercury cadmium telluride detector [17]. All IR reflection spectra were taken under near normal (~8°) incident light arrangement to minimize the anisotropy effect in InN films. The surface morphology of the layers was analyzed by atomic force microscopy (AFM). The crystalline structure of the InN layers was characterized with ω - 2θ x-ray diffraction (XRD) measurements which confirmed the crystallite orientation of $(01\bar{1}\ 1)$ for these polycrystalline films as observed in the authors' earlier work [18].

The InN samples were rinsed with isopropyl alcohol before transfer into the ultra high vacuum (UHV) chamber. The samples were mounted on a tantalum sample holder and held in place by tantalum clips. The details of the UHV system and sample mount have been reported elsewhere [19]. The base pressure of our UHV system was 1.7×10^{-10} Torr. To remove the surface contaminants due to the exposure to the air, sample cleaning was performed by sputtering with 1 keV nitrogen ions followed by atomic hydrogen cleaning. The details of sputtering and atomic hydrogen cleaning are also published elsewhere [18, 20]. Auger electron spectroscopy (AES) was used to monitor the cleanliness of the samples. AES was also used to determine the composition of the near surface region which showed equal amounts of indium and nitrogen indicating no In adlayers or droplets after surface preparation in UHV.

The desorption study was carried out by heating the samples from room temperature to 825 °C by ramping at the rate of 30 °C per minute using a temperature controller. The samples were heated by the bombardment of electrons from the back of the tantalum sample holder and

the temperatures were measured using a chromel-alumel thermocouple attached on the mount next to the sample. In order to check the reliability of the temperature measurements by thermocouple, an optical pyrometer was also used. No significant difference in temperatures was observed between the two measurements. Desorption products were measured with a differentially-pumped QMS having a pinhole in the nose cone. The sample was placed approximately 5 mm from the nose cone of the mass spectrometer and the desorbed species were monitored with the QMS while the sample temperature was ramped.

5.4 Results and discussion

The desorption of molecular nitrogen from InN with the increase of temperature is shown in Fig. 5.1. No significant NH_3 (17 amu) desorption was observed. The 14 and 28 amu desorption signals showed identical behavior at T > 600 °C. This confirms desorption of nitrogen from the InN samples in the form of N_2. However, below 600 °C, a small desorption peak of 28 amu was observed with no desorption of 14 amu. The 28 amu signal desorbed below 600 °C is attributed to carbon monoxide. In all four samples, desorption of nitrogen started at around 630 °C, increased rapidly with increasing temperature, and peaked before decreasing as shown in Fig. 5.2. After attaining the peak value, the desorption rate decreased with the increase of temperature indicating that the film was getting thinner until the entire film was desorbed completely. Though the signal to noise ratio for indium desorption was not as good as that for nitrogen, the desorption of indium was observed similar to that of nitrogen (not shown). In all InN samples studied, the shape of desorption curves was similar. However, the temperature corresponding to the maximum desorption was found to be different as seen in Fig. 5.2.

The experimental IR reflection spectra were analyzed using a multilayer stack model [21] and a Lorentz-Drude model for the dielectric of the medium to obtain the thickness of the layers. From the analysis, the film thicknesses of 270 nm, 360 nm, 320 nm and 270 nm were obtained for the samples grown with group V/III precursor ratios of 1200, 2400, 3600 and 4800 respectively. Ideally, a direct correlation of the film thicknesses with the area under the desorption curves (Fig. 5.2) is expected. However, if the films contain different amount of voids and defects, the thicknesses of the films would not correlate with the area under the desorption curves. Using the effective medium theory, the void fraction was calculated in each sample. The void fractions were 0.023, 0.23, 0.09 and 0.26 for the samples grown with group V/III precursor ratios of 1200, 2400, 3600 and 4800 respectively. Corrected values for the total thickness accounting for the void fraction were calculated and these values correlate very well with the area under the desorption curves.

Figure 5.3 shows 1μm × 1μm AFM images obtained from three of the four InN samples grown with group V/III molar precursor ratios of 1200, 2400, and 4800. The results show average grain sizes of 180 nm, 200 nm and 220 nm for the three films, respectively, indicating that average grain size increases with the increasing group V/III precursor ratio. The increase in the average grain area (larger grain size) with increasing V/III molar precursor ratio suggests a decrease in extended defects (fewer grain boundaries) for higher V/III molar precursor ratios [22]. It has been reported that thermal stability decreases with the decrease of grain size [23]. That is, as the extended defects are reduced and grain size is increased, the material is more thermally stable and a longer or higher temperature annealing is required to desorb InN films. This is consistent with the result reported here that films grown with higher group V/III ratios also exhibit larger grain sizes and yield a higher temperature of maximum desorption.

Desorption curves were used to calculate an activation energy for the desorption of nitrogen from each sample by an Arrhenius analysis. The desorption rate, R, is assumed to be described by the equation [24],

$$R = - d\theta/dt = \theta^n \nu_n e^{-(E/kT)} \quad (5.1)$$

where θ is the surface coverage, n is the order of desorption, ν is the pre exponential factor, E is the activation energy, k is the Boltzmann constant and T is the temperature in Kelvin. The desorption order was assumed to be zero since decomposition leaves the surface in an identical configuration. So the desorption rate would then be given by

$$R = - d\theta/dt = \nu_0 e^{-(E/kT)}. \quad (5.2)$$

For each of the four samples studied here the natural log of the desorption rate was plotted versus inverse temperature to determine the activation energy for the desorption of nitrogen from InN. In each case, only the leading edge of the desorption curve (Fig. 5.2) was used to find the activation energy. Figure 5.4 shows the fitting used to determine the activation energy for one of the samples in this work. The value of the activation energy was found to be 1.6 ± 0.2 eV for all four samples showing that the activation energy of InN layers is independent of group V/III precursor ratio. The activation energies for thermal decomposition of InN reported previously together with our results are summarized in Table 5.1.

In this work, the decomposition of InN was studied under high vacuum conditions. The desorbed species were measured with a QMS, keeping the nose cone of the mass spectrometer in close proximity (~5 mm) to front of the sample. The onset of the InN decomposition was observed around 630 °C. From the Arrhenius plots of each sample the calculated value of activation energy was found out to be 1.6 ± 0.2 eV. Although the activation energy as determined in previous studies varies by a large amount, the value determined in this work is

close to that reported by Koblmüller *et al.* [14] for the high temperature regime and also similar to the value given by Huang *et al*. [10]. These decomposition studies show that InN has also a large range for the activation energy (1.15 – 3.4 eV) similar to the range reported for decomposition of GaN (0.34 – 3.62 eV) [25, 26]. For GaN, the decomposition rate is reported to depend upon growth reactor designs and flow dynamics [26].

The studies on thermal stability of InN also indicate that a number of factors may affect the decomposition rate and activation energy. The analysis results summarized in Table 5.1 were performed on InN layers grown by five different methods which resulted in at least three different growth directions. Although there are wide variations in the activation energy reported, no clear trend with growth technique or film orientation is apparent. However, from the data in Table 5.1 it is clear that the onset temperatures are similar (500-630 °C) for measurements made in nitrogen or vacuum ambient while considerably lower in the presence of hydrogen (<350 °C). The activation energy measured in a hydrogen background is also at the low end of the range compared with measurements made when no hydrogen is introduced. Hydrogen in the InN layers may react or be evolved during the decomposition process. Hydrogen may also be liberated from metals during the heating of the samples. The effects of unintentional hydrogen introduction are difficult to account for or to eliminate. We suggest that the effects of hydrogen on the decomposition may add to the wide variation in measured activation energies reported.

5.5 Conclusion

In summary, thermal desorption measurements were used to study the thermal stability of HPCVD-grown InN epilayers that had been characterized by AFM, XRD, and infrared reflection measurements. The desorption of nitrogen from the InN surface started around 630 °C with a

calculated activation energy of 1.6 ± 0.2 eV, which is independent from the group V/III precursor ratio. The temperature at which the maximum desorption was observed shifted with increasing group V/III precursor ratio from 749 °C for a ratio 1200 to 776 °C for a ratio 4800. The analysis of surface topography suggests that this shift is related to the decreased extended defects and increased grain size with increasing group V/III precursor ratio.

Table 5.1 Summary of the results for thermal stability of InN reported in the literature and current work.

Authors (Reference)	Growth technique	Growth direction	Measurement technique	Annealing medium	Desorption onset temp. ($^{\circ}$C)	Activation energy (eV)
Huang *et al*. (Ref. 10)	MOCVD	-	Laser reflection	N_2	500	2.1 ± 0.1
Togashi *et al*. (Ref. 11)	HVPE	$[000\bar{1}]$	-	N_2	610	3.33
Togashi *et al*. (Ref. 22)	HVPE	[0001]	-	N_2	550	-
Togashi *et al*. (Ref. 22)	HVPE	$[000\bar{1}]$	-	H_2	< 350	1.10
Togashi *et al*. (Ref. 22)	HVPE	[0001]	-	H_2	< 350	1.74
Ambacher *et al.* (Ref. 12)	LPCVD	-	QMS	Vacuum	630	3.48
Koblmüller *et al.* (Ref. 13)	PA-MBE	$[000\bar{1}]$	QMS	Vacuum	560	1.15 (high temp. regime)
Koblmüller *et al.* (Ref.13)	PA-MBE	$[000\bar{1}]$	QMS	Vacuum	560	4.4 (low temp. regime)
Current work	HPCVD	$[01\bar{1}1]$	QMS	Vacuum	630	1.6 ± 0.2

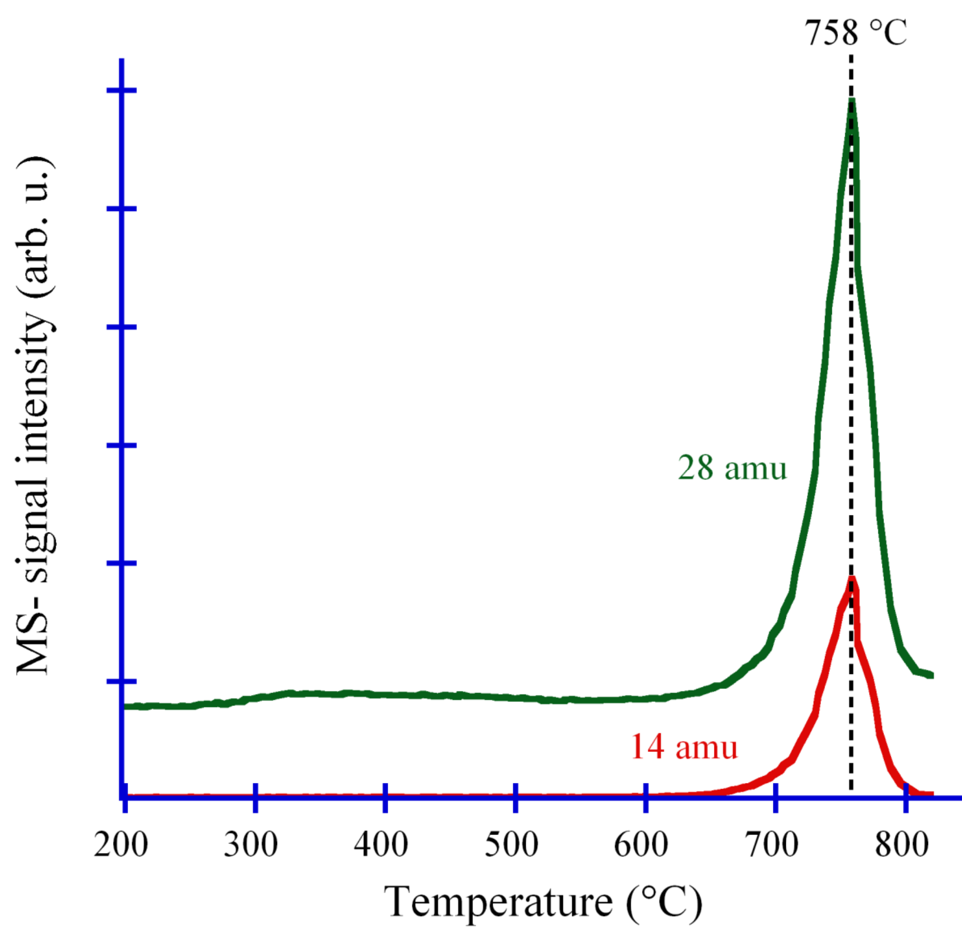

Figure 5.1 Mass spectrometer signal intensity of nitrogen species desorbed from InN as a function of temperature. These data were collected from InN layer grown with a V/III precursor ratio of 2400 although data from other samples are similar.

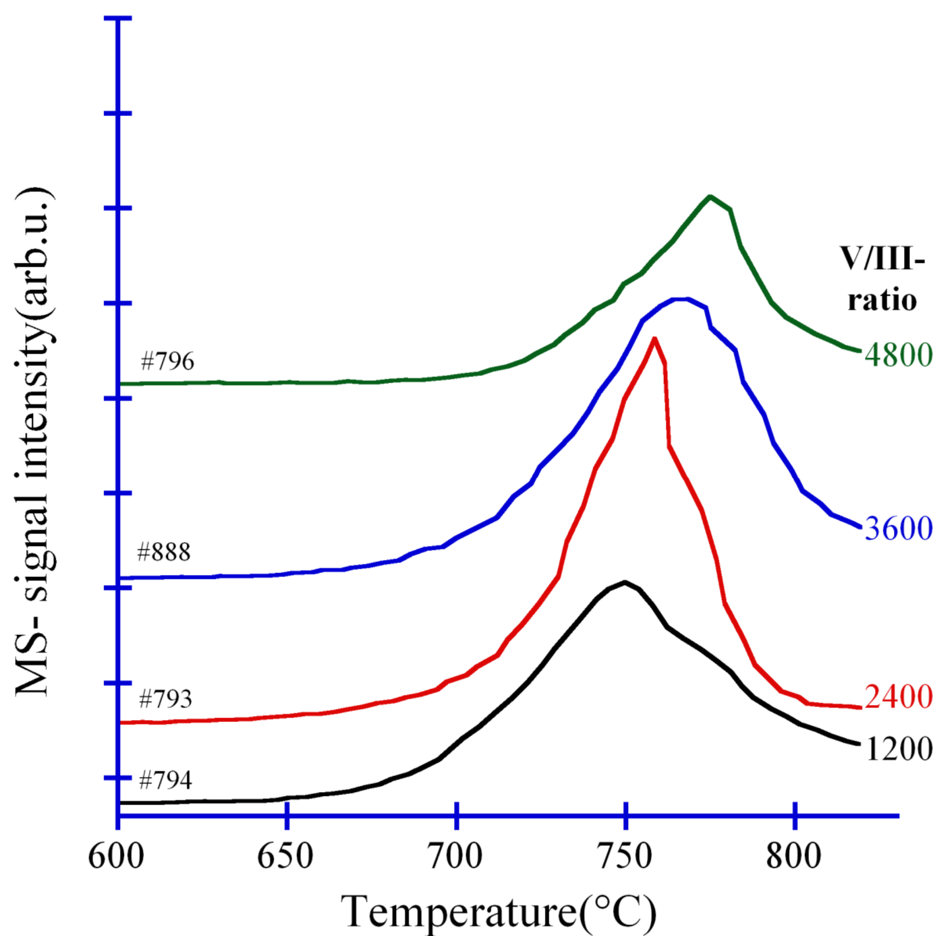

Figure 5.2 Mass spectrometer signal intensity for 28 amu as a function of temperature measured while sample temperature was increased linearly at 30 °C /min from InN samples of V/III precursor ratios varying from 1200 to 4800.

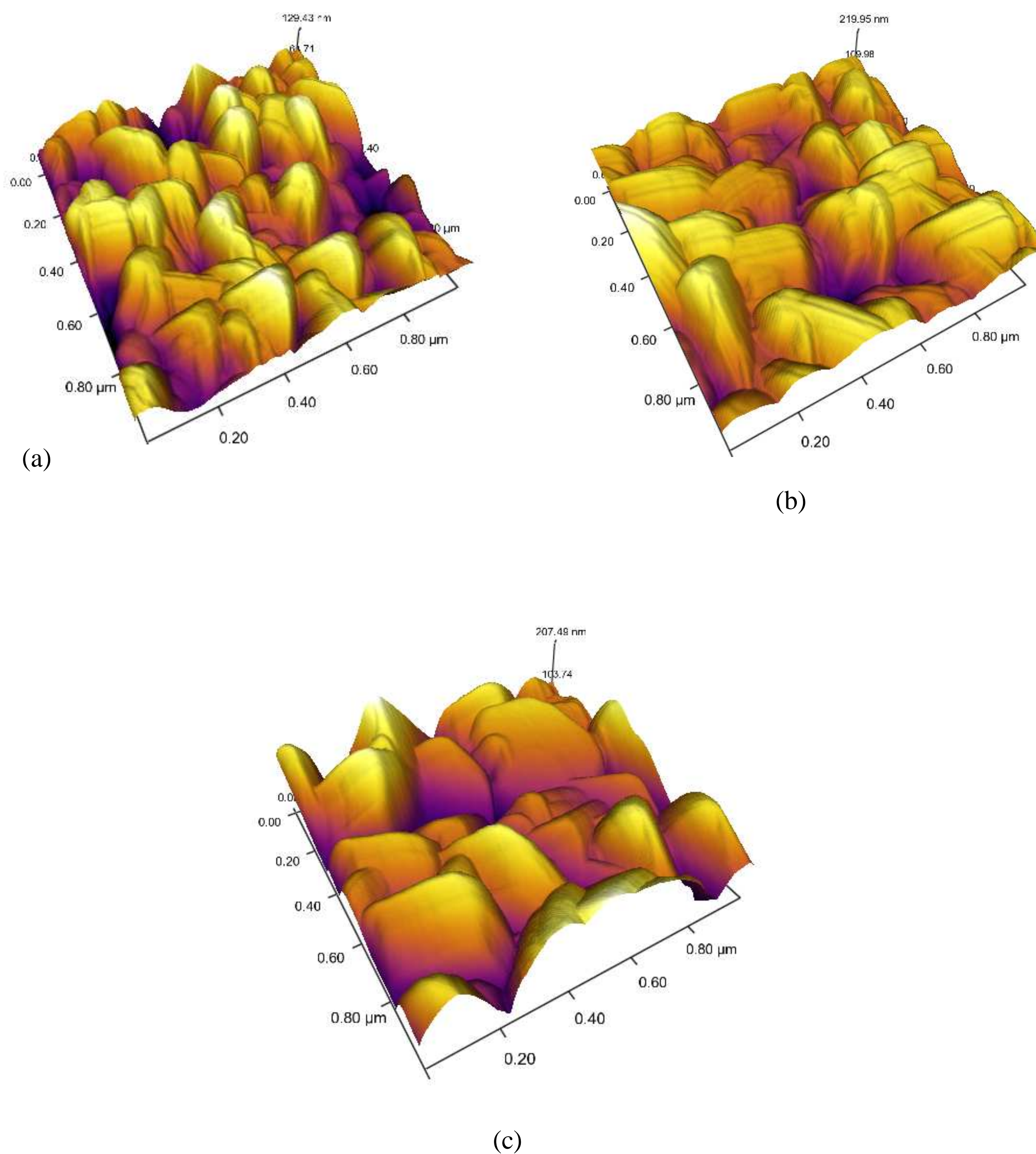

Figure 5.3 1μm × 1μm AFM images for InN epilayers deposited on sapphire (0001) substrates. The layers were grown with group V/III molar precursor ratios of (a) 1200 (b) 2400, and (c) 4800. Analysis of the images yields average grain sizes of 180 nm, 200 nm and 220 nm for the three films, respectively.

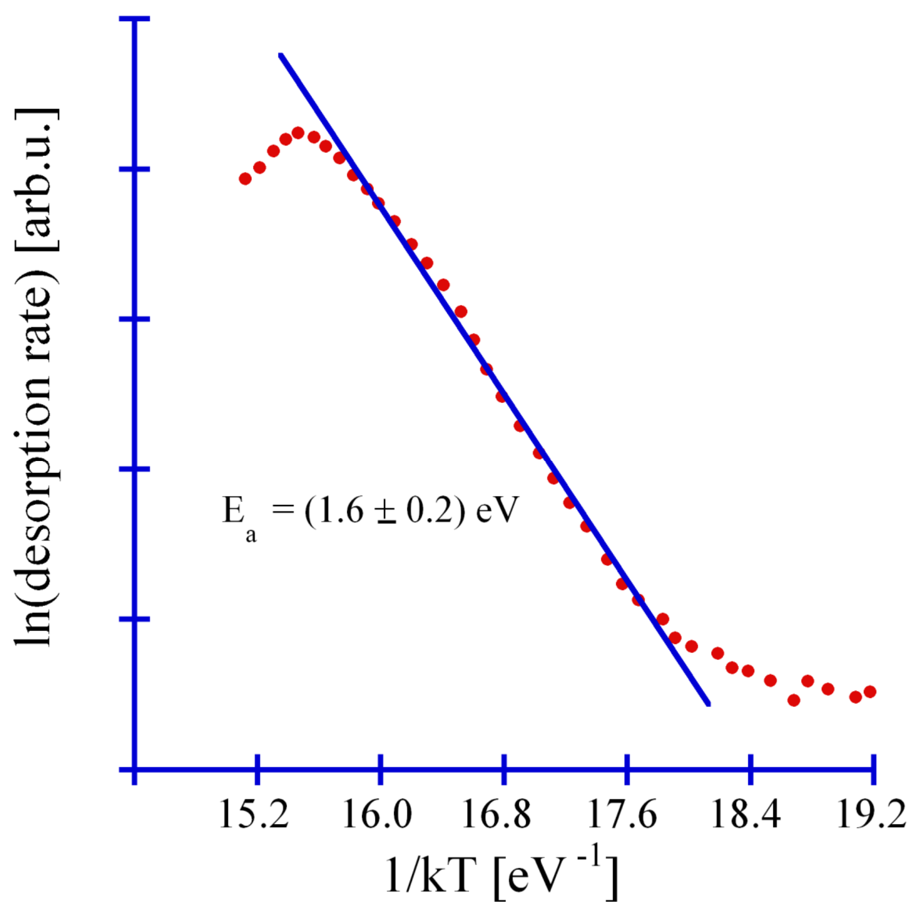

Figure 5.4 Natural log of 28 amu mass spectrometer signal as a function of 1/kT for InN sample with V/III- ratio of 2400 while sample temperature was linearly increased at 30 °C /min. The activation energy was calculated using the slope of the best fit line for the linear region of the graph.

5.6 References

[1] K. M. Yu, Z. Liliental-Weber, W. Walukiewicz, W. Shan, J. W. Ager, S. X. Li, R. E. Jones, E. E. Haller, Hai Lu, and William J. Schaff, Appl. Phys. Lett. **86**, 071910 (2005).

[2] M. Higasshiwaki and T. Matsui, Jpn. J. Appl. Phys. **41**, L540 (2002).

[3] J. Wu, W. Walukiewicz, K. M. Yu, W. Shan, J. W. Ager, E. E. Haller, Hai Lu, William J. Schaff, W. K. Metzger, and Sarah Kurtz, J. Appl. Phys. **94**, 6477 (2003).

[4] T. B. Fehlberg *et al.*, Jpn. J. Appl. Phys. **45**, L1090 (2006).

[5] V. M. Polyakov and F. Schweirz, Appl. Phys. Lett. **88**, 032101 (2006).

[6] H. Lu, W. J. Schaff, L. F. Eastman, J. Appl. Phys. **96**, 3577 (2004).

[7] S. Yamaguchi, R. Izaki, N. Kaiwa, S. Sugimura, A. Yamamoto, Appl. Phys. Lett. **84**, 5344 (2004).

[8] Y. M. Meziani, B. Maleyre, M. L. Sadowski, S. Ruffenach, O. Briot, W. Knap, Phys. Stat. Sol. (a) **202**, 590 (2005).

[9] N. Dietz, M. Strassburg, and V. Woods, J. Vac. Sci. Technol. A **23**, 1221 (2005).

[10] Y. Huang, H. Wang, Q. Sun, J. Chen, J. F. Wang, Y. T. Wang, and H. Yang, J. Crystal Growth **281**, 310 (2005).

[11] R. Togashi, T. Kamoshita, Y. Nishizawa, H. Murakami, Y. Kumagai, and A. Koukitu, Phys. Stat. Sol. (c) **5**, 1518 (2008).

[12] R. Togashi, T. Kamoshita, H.Adachi, H. Murakami, Y. Kumagai, and A. Koukitu, Phys. Stat. Sol.(c) **6**, S372 (2009).

[13] O. Ambacher, M. S. Brandt, R. Dimitrov, T. Metzger, M. Stutzmann, R. A. Fischer, A. Miehr, A. Bergmaier, and G. Dollinger, J. Vac. Sci. Technol. B **14**, 3532 (1996).

[14] G. Koblmüller, C. S. Gallinat, and J. S. Speck, J. Appl. Phys. **101**, 083516 (2007).

[15] N. Dietz, M. Alevli, V. Woods, M. Strassburg, H. Kang, I. T. Ferguson, Phys. Stat. Sol. (b) **242**, 2985 (2005).

[16] V. Woods, N. Dietz, Mat. Sci. Eng. B **127**, 239 (2006).

[17] Z. G. Hu, M. Strassburg, A. Weerasekara, N. Dietz, A. G. U. Perera, M. H. Kane, A. Asghar, and I. T. Ferguson, Appl. Phys. Lett. **88**, 061914 (2006).

[18] A. R. Acharya, M. Buegler, R. Atalay, N. Dietz, B. D. Thoms, J. S. Tweedie, and R. Collazo, J. Vac. Sci. Technol. A **29**, 041402 (2011).

[19] V. J. Bellitto, B. D. Thoms, D. D. Koleske, A. E. Wickenden, and R. L. Henry, Surf. Sci. **430**, 80 (1999).

[20] R. P. Bhatta, B. D. Thoms, M. Alevli, and N. Dietz, Surf. Sci. **601**, L120 (2007).

[21] A. B. Weerasekara, Z. G. Hu, N. Dietz, A. G. U. Perera, A. Asghar, M. H. Kane, M. Strassburg, and I. T. Ferguson, J. Vac. Sci. Technol. B **26**, 52 (2008).

[22] G. Durkaya, M. Buegler, R. Atalay, I. Senevirathna, M. Alevli, O. Hitzemann, M. Kaiser, R. Kirste, A. Hoffmann, and N. Dietz, Phys. Stat. Sol.(a) **207**, 1379 (2010).

[23] G. Korotcenkov, S. D. Han, B. K. Cho, V. Brinzari, Critical Reviews in Solid State and Material Sciences **34** (1–2), 1–17 (2009).

[24] P. A. Redhead, Vacuum **12**, 203 (1962).

[25] D. D. Koleske, A. E. Wickenden, R. L. Henry, M. E. Twigg, J. C. Culbertson, R. J. Gorman, Appl. Phys. Lett. **73**, 2018 (1998).

[26] D. D. Koleske, A. E. Wickenden, R. L. Henry, J. C. Culbertson, M. E. Twigg, J. Cryst. Growth **223**, 466 (2001).

6 SURFACE STRUCTURE, POLARITY AND SURFACE KINTETICS OF INDIUM NITRIDE GROWN BY PLASMA-ASSISTED ATOMIC LAYER EPITAXY: A HREELS STUDY

6.1 Abstract

The surface bonding configuration and kinetics of hydrogen desorption from InN grown on Si(100) by plasma-assisted atomic layer epitaxy have been investigated. High resolution electron energy loss spectra exhibited loss peaks assigned to a Fuchs-Kliewer surface phonon, N-N and N-H surface species. The observation of N-H but no In-H surface species suggests N-polar InN. Isothermal desorption data was best fit by the first-order desorption kinetics with an activation energy of 0.88 ± 0.06 eV and pre-exponential factor of $(1.5 \pm 0.5) \times 10^5$ s^{-1}. The lower activation energy, the first-order desorption kinetics and surface N-N vibrations are attributed to surface defects.

6.2 Introduction

Indium nitride, a group-III nitride compound semiconductor, has attracted an extensive research interest over the past decade due to its unique electronic properties such as; small effective mass, large electronic mobility, high peak and saturation velocities and small band gap energy. These properties make InN a potential material for a number of electronic and optoelectronic devices [1]. However, among other group–III nitride semiconductors, InN is less studied due to difficulties in producing good quality InN films ensuing from its low dissociation temperature, high equilibrium vapor pressure of nitrogen and lack of suitable lattice matched substrates [2]. InN epilayers have been grown by a number of techniques including metal

organic chemical vapor deposition (MOCVD), molecular beam epitaxy (MBE), liquid phase epitaxy (LPE), and hydride vapor phase epitaxy (HVPE). Atomic layer epitaxy (ALE) has been found to be an effective technique to produce good quality metal nitrides [3, 4]. This technique has a wide range of advantages such as stoichiometric film growth with large area uniformity, precise thickness control, and low temperature deposition [5].

In recent years, the number of publications related to InN research has increased significantly. Most of the studies have been focused on the structural (crystalline), chemical, electrical and optical properties. However, there are a very few studies on the fundamental surface properties of InN. These studies are very important to gain an understanding of the growth mechanism because surface structure and bonding affect kinetic processes during growth which determine the quality of the films and the performance of subsequent devices fabricated in such films [6]. In previous work from the author's research group, Bhatta *et al.* [6] reported on the surface structure and bonding configurations of high pressure chemical vapor deposition (HPCVD)–grown InN samples using high resolution electron energy loss spectroscopy (HREELS). From HREELS measurements it was concluded that the HPCVD-grown InN surfaces were nitrogen terminated indicating that the films were N polar. In other work from the author's group tilted planes on HPCVD–grown InN were observed and attributed to the effects of high group V/III ratio and lattice mismatch [7].

During the metalorganic growth of InN films, surface reactions involving hydrogen are important steps. When a precursor such as $In(CH_3)_3$, trimethylindium (TMI), is decomposed during the growth of InN, surface hydrogen atoms are produced. These surface hydrogen atoms reduce the number of available reaction sites for indium and nitrogen precursors affecting the quality and composition of the films. The surface hydrogen atoms produced during epitaxial

growth of InN are usually eliminated by desorption after reacting with adsorbed methyl groups or other hydrogen atoms. It has been reported that an increase in hydrogen partial pressure decreases the deposition rate of InN and the increase in H_2 production switches the system from deposition mode to the etching mode [8]. Moreover, InN strongly reacts with atomic hydrogen resulting in the depletion of nitrogen and formation of In droplets at the surface [9].

Knowing the kinetic parameters for surface reactions is crucial in order for determining the effects of hydrogen on the growth of InN. However, very few studies have been done and both qualitative and quantitative details of many of the important surface reactions occurring during the growth are still unknown [10]. In this work, we have determined the kinetic parameters for hydrogen desorption from the plasma-assisted atomic layer epitaxy (PA-ALE)-grown InN surface using HREELS. In addition, HREELS has been used to study the surface bonding configurations and polarity of InN grown by PA-ALE.

6.3 Experimental methods

The InN layers used in this study were grown by PA-ALE on silicon(100) at 240 ℃ as described in detail by Nepal *et al.* [11]. After *ex situ* cleaning with deionized water and acid pretreatment, the substrate was treated *in situ* with 50 sccm N_2 plasma at 300 W prior to the growth of InN in an argon ambient. Trimethylindium (TMI), a group III-precursor, was pulsed for 60 ms and added to 30 sccm flow of ultrahigh purity (UHP) argon carrier gas while 100 sccm of UHP argon was introduced separately through the plasma source. This total flow of argon resulted in a reactor pressure to 166 millitorr. In order to enhance the saturation of the sample surface with TMI molecules, the main pumping valve was stopped for 5 sec after each TMI pulse. After each stop, the chamber was purged with UHP Ar for 10 sec to remove unreacted

precursor and by products. A 20 s long, 300 W UHP nitrogen plasma pulse with a flow rate of 100 sccm was used as a group-V precursor. Unreacted precursors and reaction products were then removed by purging the deposition chamber with UHP Ar for 10s. In order to synthesize InN epilayers, 800 cycles of ALE were employed and the growth rate was 0.51 nm/cycle (1 atomic layer per cycle).

The sample was exposed to air before insertion into an ultra-high vacuum (UHV) chamber with a base pressure of 1.5×10^{-10} Torr. The sample was mounted on a tantalum sample holder, and held in place by tantalum clips. Sample heating was done by bombardment of electrons from the back of the tantalum sample holder. The temperature of the sample was measured with a chromel-alumel thermocouple. Auger electron spectroscopy (AES) was performed to monitor the surface cleanliness. AES of the as-inserted sample showed oxygen and carbon contamination due to the exposure of the sample to the atmosphere. Sample cleaning was performed by sputtering the sample surface with 1 keV nitrogen ions followed by atomic hydrogen cleaning (AHC) or atomic deuterium cleaning (ADC). The details of the cleaning the sample by sputtering followed by AHC have been published elsewhere [6, 7, 10]. AES spectra after a few cycles of cleaning confirmed that the InN surface was free from contaminants. HREEL spectra were achieved in a specular geometry with an incident and scattered angle of 60º from the normal. The energy of the incident electrons was 7.0 eV. In order to determine the surface kinetic parameters, two series of isothermal desorption experiments were performed. To avoid the confounding effects of background hydrogen, deuterium (D_2) was used to model the surface interaction with hydrogen. In the first series the sample was heated to a target temperature between 200 ºC and 375 ºC and held for 900 seconds. In the second series sample was heated to a target temperature between 200 ºC to 425 ºC and held for 90 seconds. The

surface was restored to its original condition through ADC before each isothermal heating treatment.

6.4 Results and discussion

HREEL spectra of InN acquired after AHC and ADC are shown in Fig. 6.1. A loss peak observed at 550 cm^{-1} in both spectra is assigned to the Fuchs-Kliewer surface phonon [12]. Loss peaks observed at 3260 cm^{-1} for the AHC surface and 2410 cm^{-1} for the ADC surface are assigned to N-H and N-D stretching vibrations, respectively. These assignments are in excellent agreement with those by Bhatta *et al.* [6] on AHC/ADC InN surface grown by high pressure chemical vapor deposition (HPCVD). In contrast to the previous work on HPCVD-grown InN, two prominent peaks at 1240 cm^{-1} and 2020 cm^{-1} are observed from both AHC and ADC PA-ALE-grown InN surfaces. These peaks are not related to hydrogen because no isotope shift is observed between AHC and ADC surfaces. The authors suggest that these loss peaks are due to surface N-N vibrational modes. In the literature, N-N stretching vibrational modes have been reported over a wide range of frequencies. N-N stretching modes of vibration on Ru(001) were reported at 2195 cm^{-1} and 2200-2250 cm^{-1} by De Paola *et al.* [13] and Anton *et al* [14], respectively. Apen and Gland [15] observed the N-N stretching mode on the GaAs surface at 1671 cm^{-1}. So, it is suggested that the loss peak at 2020 cm^{-1} is due to a surface N-N stretch while the loss peak at 1240 cm^{-1} could be due to a N-N bend.

On InP surfaces, the InH stretch has been reported at 1650 – 1700 cm^{-1} in HREELS experiments [16-18] and at 1630 – 1680 cm^{-1} from calculations [19]. However, the present study showed no HREELS loss features in this range indicating no InH on the InN surface. The x-ray diffraction pattern measured in ω-2Θ scan (not shown here) shows Bragg reflexes from InN

(0002) indicating the growth of the film along c-axis. The observation of surface N-H vibrations but no In-H vibrations demonstrates nitrogen termination of the InN layer. Together x-ray diffraction and HREELS results are consistent with a c-axis oriented nitrogen polar InN film [6].

HREEL spectra acquired after annealing the ADC surface to various temperatures for 900 s are shown in Fig. 6.2. The surface was restored to the same condition by sputtering and ADC before each desorption experiment. Heating to 275 ºC produced little change in the intensity of N-D peak. Heating to 350 ºC resulted in a much larger decrease in the intensity of the N-D peak and heating to 375 ºC completely removed deuterium from InN surface as shown in Fig. 6.2. The results of a similar experiment on the sample with anneal times of 90 seconds (Figure not shown) showed that as the temperature increased, the N-D peak intensity decreased and the peak disappeared after annealing the sample at 425 ºC. In both cases, the peaks at 1240 cm^{-1} and 2020 cm^{-1} remained unchanged even after removing the deuterium completely from the sample surface. This further supports the idea that these loss peaks are not related to hydrogen vibrational modes. With higher annealing temperatures, N-H stretching vibrational peaks appear at 3260 cm^{-1} and are attributed to the readsorption of hydrogen liberated from the sample mount during the heating [20].

To date, there has been no published work on the desorption of hydrogen from the ALE-grown InN surface. However, there have been a few reports on the desorption of hydrogen from InN and GaN surfaces grown by other techniques. Bhatta *et al.* [21] reported the desorption of hydrogen from HPCVD-grown N-polar InN surface at 425 ºC annealed for 900 s or at 500 ºC annealed for 30 s. Bellitto *et al.* [22] observed a complete disappearance of Ga-H stretch intensity from MOCVD-grown GaN surface after briefly heating at 380 ºC. Sung *et al.* [23] reported the desorption of hydrogen from the nitrogen sites on a metal organic vapor phase

epitaxy grown GaN surface at 850 ºC. In contrast, Chiang *et* al. [24] reported hydrogen desorption from Ga-sites of a GaN surface at 250 ºC and from N-sites at 500 ºC. The desorption temperature from N-sites on ALE-grown InN reported in this work is lower than that reported for N-sites on InN and GaN grown by other techniques. [21-24]. Rendulic *et al*. [25] studied the role of surface defects in the desorption of hydrogen on Ni(111) surface. They reported that surface defects introduced non-activated adsorption sites which lowered the desorption temperature. In this study, the HREELS spectra showed the prominent loss peaks related to N-N vibrations indicating the presence of a significant amount of surface defects. Therefore, we suggest that the observation of lower desorption temperature of hydrogen from ALE-grown InN surface is attributed to the presence of surface defects.

The kinetic parameters have also been determined from the HREEL spectra. Relative surface coverages were obtained by integrating the area under N-D stretching vibrational peak in each normalized HREEL spectrum. The normalized N-D stretch intensity is assumed to be proportional to the surface coverage [26]. The normalized N-D intensity was plotted as a function of annealing temperature. During ADC, the sample was annealed to 325 ºC. However, the exposure with atomic deuterium was continued until the sample was cooled down to ~200 ºC. For this reason, N-D stretch intensities after ADC are plotted as equivalent to a 200 ºC anneal.

The experimental data were fit using the first and second order desorption kinetics. To determine the kinetic parameters for hydrogen desorption the integrated N-D stretch intensities were fit using equations for first and second order desorption kinetics. The data were fit with the equations [10],

$$\frac{\theta}{\theta_o} = e^{-\nu_1 t \exp(-E/kT)} \tag{6.1}$$

and

$$\frac{\theta}{\theta_o} = \frac{1}{1 + \theta_o \nu_2 t \, e^{(-E/kT)}} \tag{6.2}$$

where θ is the surface deuterium coverage, θ_o is the initial coverage, t is the anneal time, v_1 is the first-order pre-exponential factor, v_2 is the second-order pre-exponential factor, E is the activation energy, k is the Boltzmann constant and T is the temperature in Kelvin. The normalized N-D stretch intensity as a function of temperature was fit to both first-order and second-order desorption kinetics using equations (6.1) and (6.2), respectively. First- and second-order fits to data for 900 s anneals are shown in Fig. 6.3. Although the data can be fit well using either first- or second-order kinetics, only first-order kinetics was able to fit data for both 900 s and 90 s (not shown) anneal data with the same activation energy and pre-exponential factor. This analysis yields first-order desorption kinetics with activation energy of 0.88 ± 0.06 eV and a pre-exponential factor of (1.5 ± 0.5) $\times 10^5$ s^{-1}. Bhatta *et al.* [21] reported that desorption of hydrogen from HPCVD-grown InN samples was best described by second-order kinetics with an activation energy of 1.3 ± 0.2 eV. We suggest that surface defect sites result in first-order desorption process for hydrogen recombination being dominant on this surface and resulting in a lower activation energy and temperature [25] than observed in the case of HPCVD-grown InN.

6.5 Conclusion

In summary, the surface bonding configuration and kinetics of hydrogen desorption from PA-ALE-grown InN were investigated using high resolution electron energy loss spectroscopy. HREELS showed surface N-N vibrational modes at 1240 cm^{-1} and 2020 cm^{-1} indicating the presence of surface defects. Hydrogenated and deuterated InN surface showed N-H and N-D stretch vibrations, respectively, while no In-H modes were observed indicating N-polar InN. Complete desorption of surface hydrogen was observed after heating to 375 ºC for 900 s or 425 ºC for 90 s. First-order kinetics best described the desorption of hydrogen from InN surface with an activation energy of 0.88 ± 0.06 eV and a pre-exponential factor of (1.5 ± 0.5) $\times 10^5$ s^{-1}. The lower values of activation energy and desorption temperature than previously reported along with first-order desorption kinetics were attributed to the presence of surface defects.

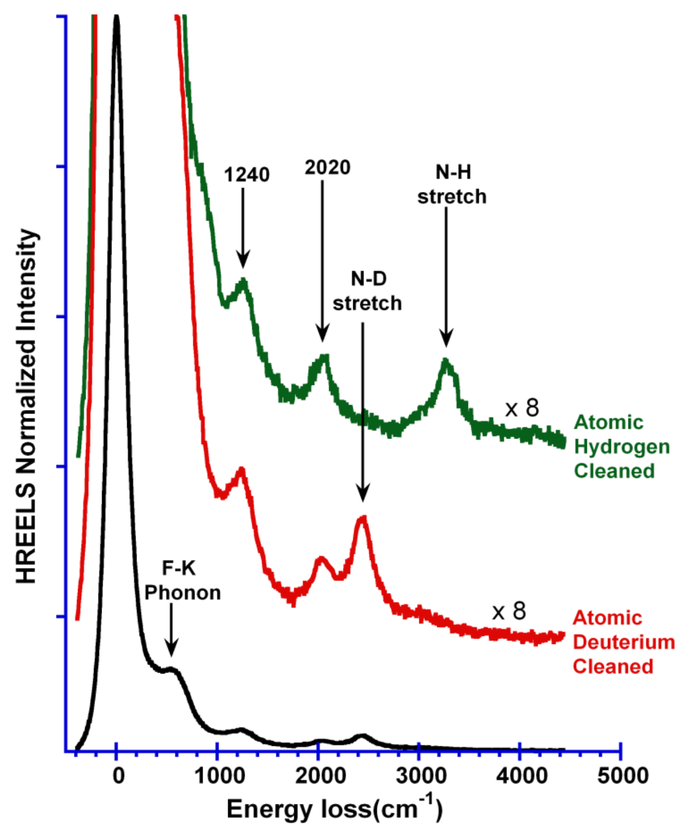

Figure 6.1 HREELS of InN after atomic hydrogen and atomic deuterium cleaning. Spectra were acquired in the specular direction with an incident electron energy of 7.0 eV.

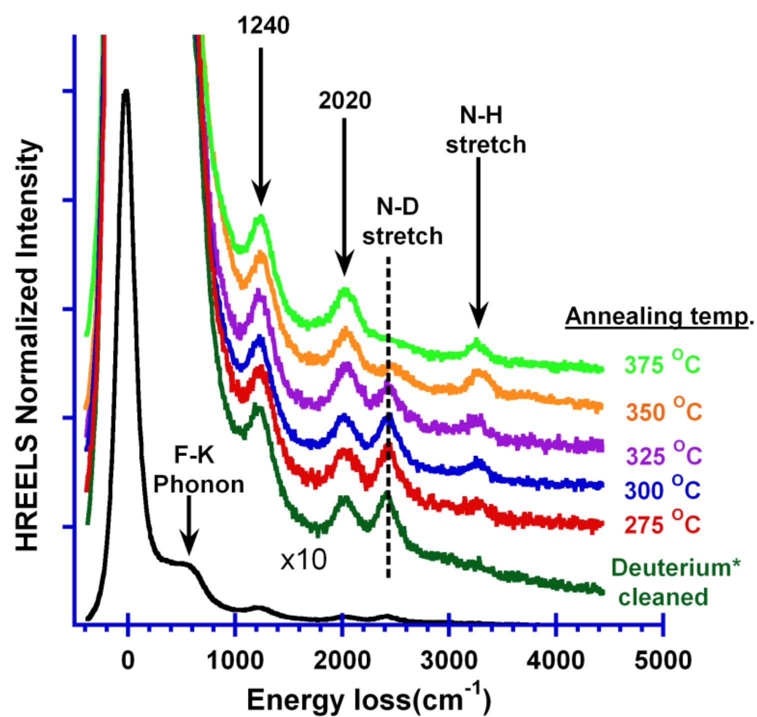

Figure 6.2 HREEL spectra after InN sample preparation by atomic deuterium cleaning (ADC) and after heating to 275, 300, 325, 350 and 375 ºC for 900 s. The surface was restored to the same initial state with ADC prior to each heat treatment.

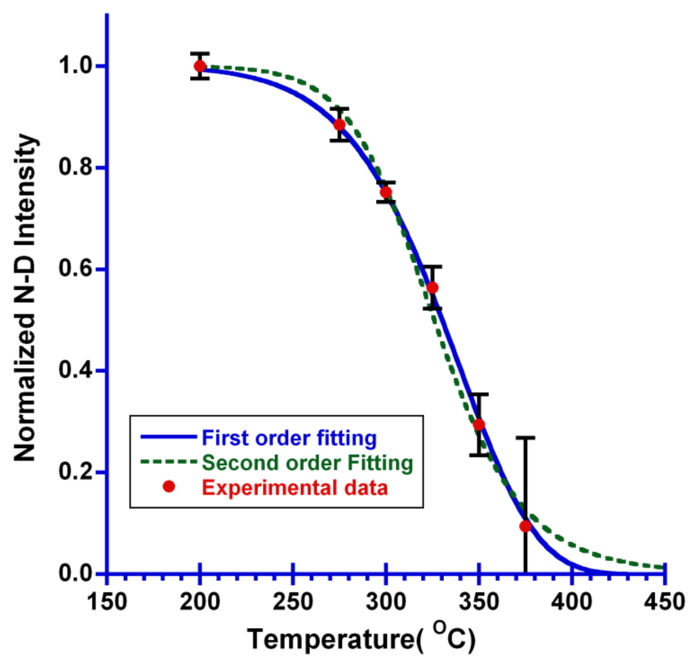

Figure 6.3 Fitting of first and second-order desorption kinetics to measurements of deuterium coverage (obtained from HREELS N-D stretch intensity) as a function of heating temperature for the InN sample after preparation by atomic deuterium cleaning and heating for 900 s to 275, 300, 325, 350, and 375 ºC. Equations and parameters used in the fitting are described in the text.

6.6 References

[1] N. Ma, X. Q. Wang, F. J. Xu, N. Tang, B. Shen, Y. Ishitani, and A. Yoshikawa, Appl. Phys. Lett. **97**, 222114 (2010).

[2] R. Cuscó, N. Domènech-Amador, L. Artús, T. Gotschke, K. Jeganathan, T. Stoica, and R. Calarco, Appl. Phys. Lett. **97**, 221906 (2010).

[3] H. Kim, J. Vac. Sci. Technol. A **21**, 2231 (2003).

[4] M. Ritala and M. Leskela, in: Handbook of Thin Film Materials, Vol. 1, edited by H. S. Nalwa (Academic Press, New York, 2002).

[5] Mikko Ritala, Markku Leskelä, "Hand Book of Thin Film Materials", Volume 1, chapter 2, "Deposition and Processing of Thin Film", Academic Press (2002).

[6] R. P. Bhatta, B. D. Thoms, M. Alevli, V. Woods, and N. Dietz, Appl. Phys. Lett. **88**, 122112 (2006).

[7] A. R. Acharya, M. Buegler, R. Atalay, N. Dietz, B. D. Thoms, J.S. Tweedie, and R. Collazo, J. Vac. Sci. Technol. A **29**, 041402 (2011).

[8] A. Koukitu, T. Taki, N. Takahashi, H. Seki, J. Cryst. Growth **197**, 99 (1999).

[9] M. Losurdo, M. M. Giangregori, G. Bruno, T. H. Kim, P. Wu, S. Choi, M. Morse, A. Brown, F. Masia, A. Polimeni, M. Capizzi, Matter. Res. Symp. Proc. **892**, FF08 (2006).

[10] R. P. Bhatta, B. D. Thoms, M. Alevli, and N. Dietz, Surf. Sci. **602**, 1428 (2008).

[11] N. Nepal, N. A. Mahadik, L. O. Nyakiti, S. B. Qadri, M. J. Mehl, J. K. Hite, and C. R. Eddy, Jr., Cryst. Growth Des., **13 (4)**, 1485 (2013).

[12] R. Fuchs and K. L. Kliewer, Phys. Rev. **140**, A2076 (1965).

[13] R. A. de Paola, F. M. Hoffmann, D. Heskett, E. W. Plummer, Phys. Rev. B **35**, 4236 (1986).

[14] A. B. Anton, N. R. Avery, B. H. Toby, W. H. Weinberg, J. Electron Spectros. Relat. Phenom. **29**, 181 (1983).

[15] E. Apen, J. L. Gland, Surf. Sci. **321**, 308 (1994).

[16] N. Nienhaus, S. P. Grabowski and W. Monch, Surf. Sci. **368**, 196 (1996).

[17] U. D. Pennino, C. Mariani, A. Ammoddeo, F. Proix, and C. Sebenne, J. Electron. Spectrosc. Relat. Phenom. **64**, 491 (1993).

[18] X. Hou, S. Yang, G. Dong, X. Ding, and X. Wang, Phys. Rev.B **35**, 8015 (1987).

[19] J. Fritsch, A. Eckert, P. Pavone, and U. Schroder, J. Phys.: Condens. Matter **7**, 7717 (1995).

[20] A. R. Acharya, S. Gamage, M. K. I. Senevirathna, M. Alevli, K. Bahadir, A. G. Melton, N. Dietz, and B. D. Thoms, Appl. Surf. Sci., **268**, 1 (2013).

[21] R. P. Bhatta, B. D. Thoms, M. Alevli, and N. Dietz, Surf. Sci. **602**, 1428 (2008).

[22] V. J. Bellitto, Y. Yang, B. D. Thoms, D. D. Koleske, A. E. Wickenden, and R. L. Henry, Surf. Sci. **442,** L1019 (1999).

[23] M. M. Sung, J. Ahn, V. Bykov, J. W. Rabalais, D. D. Koleske, A. E. Wickenden, Phys. Rev. B **54,** 14652 (1996).

[24] C. M. Chiang, S. M. Gates, A. Bensaoula, J. A. Schultz, Chem. Phys. Lett. **246**, 275 (1995).

[25] K. D. Rendulic, A. Winkler, and H. P. Steinruck, Surf. Sci. **185**, 469 (1987).

[26] H. Ibach, D. L. Mills, Electron Energy Loss Spectroscopy and Surface Vibrations, Academic Press, New York, 1982.

7 STRUCTURAL, COMPOSITIONAL, AND THERMAL STABILITY STUDIES ON $In_{0.96}Ga_{0.04}N$ EPILAYERS GROWN BY HIGH PRESSURE CHEMICAL VAPOR DEPOSITION

7.1 Abstract

The structural and compositional properties of indium gallium nitride ($In_{0.96}Ga_{0.04}N$) epilayers grown by high-pressure chemical vapor deposition have been studied using x-ray diffraction (XRD), Auger electron spectroscopy (AES) and high-resolution electron energy loss spectroscopy (HREELS). In addition, the thermal stability of the epilayers has been studied using temperature programmed desorption (TPD). The peak at 31.38° in the XRD pattern is assigned to $In_{0.96}Ga_{0.04}N$ (0002) Bragg reflex, indicating single-phase and c-axis oriented epilayers. AES measurements also indicate 4% gallium and 96% indium in the film. The HREEL spectra of atomic hydrogen-exposed surfaces exhibited modes assigned to a surface N–H species, which were confirmed by observation of isotopic shifts following exposure to atomic deuterium. No In–H or Ga-H vibrations were observed suggesting an N-polar film. Two prominent peaks at 1240 cm^{-1} and 2020 cm^{-1} were assigned to N-N modes of vibration indicating the present of surface defects. The thermal desorption study indicated that nitrogen desorption from the sample started at 625 °C and peaked at 740 °C. No significant desorption of NH or NH_2 fragments was observed. From an Arrhenius plot, an activation energy for the desorption of nitrogen of 1.14 ± 0.06 eV was calculated.

7.2 Introduction

$In_{1-x}Ga_xN$ alloy system, a ternary compound of III-nitride materials, attracts significant attention to the researchers as it is a potential material for device applications such as light emitting diodes and photovoltaics [1,2]. GaN and Ga-rich $In_{1-x}Ga_xN$ have been considered as the most important and indispensable materials used for the fabrication of light emitters which are active in entire visible and part of the near UV spectral regions. The optical band gap of the $In_{1-x}Ga_xN$ alloy system can be tuned continuously from ultraviolet (GaN=3.4 eV) to near-infrared (InN=0.7eV) [3-6], which has an almost perfect match to the terrestrial solar spectrum. This is of interest for the development of high-efficiency monolithic multijunction photovoltaic solar cells [7], photoelectrochemical cells [8] and high brightness nitride light emitting diodes and laser diodes [3]. Despite having outstanding applications, however, the realization of high crystalline quality $In_{1-x}Ga_xN$ films in the entire composition range is a great challenge, particularly when a high indium concentration is required. One of the main problems associated with the growth of high crystalline quality $In_{1-x}Ga_xN$ alloys is the thermal instability of InN. One of the ways to avoid thermal dissociation is to grow $In_{1-x}Ga_xN$ epilayers at low temperature. But at low temperature the cracking efficiency of the ammonia precursor is extremely low, requiring a large group V-III precursors ratio for low-pressure CVD growth [9]. It has been reported that InN and related alloys can be grown at much higher temperatures through surface stabilization at higher reactor pressures [9]. High-pressure chemical vapor deposition (HPCVD) has been shown to be a viable approach to produce high quality III-N epilayers [9].

Despite the extensive study and significant progress in $In_{1-x}Ga_xN$ technology, however, the fundamental physics related to the $In_{1-x}Ga_xN$ materials has not been well developed yet. Some of the physical and chemical properties are still estimated based on the two binary

compounds, GaN and InN [10]. Moreover, though there are several reports on the fundamental surface properties of GaN and InN [11-15], no such studies have been done in $In_{1-x}Ga_xN$. Studies of the surface structure and reactions are an important part of gaining an understanding of the growth mechanism. Surface structure and bonding affect kinetic processes during the growth which determine the quality of the films and the performance of the devices [11]. It is well known that the polarity of III-nitride materials strongly influences its electrical and chemical properties [16, 17]. On the other hand, studies on the thermal stability and decomposition behavior of the $In_{1-x}Ga_xN$ epilayers is very important in understanding and controlling the growth process as well as estimating the device performance and life time [18]. In this work, the structure, composition and surface bonding configuration of HPCVD-grown $In_{0.96}Ga_{0.04}N$ epilayers have been studied using X-ray diffraction (XRD), Auger electron spectroscopy (AES), and high resolution electron energy loss spectroscopy (HREELS). From the HREELS measurement, the polarity of the $In_{0.96}Ga_{0.04}N$ film is reported. In addition, we report the results of an investigation of the thermal stability of HPCVD-grown $In_{0.96}Ga_{0.04}N$ epilayers by temperature programmed desorption including a determination of the activation energy for molecular nitrogen evolution.

7.3 Experimental methods

The $In_{0.96}Ga_{0.04}N$ epilayers investigated were grown by HPCVD on ~5mm thick GaN/c-plane sapphire template. Trimethylindium (TMI), trimethylgallium (TMG), and ammonia (NH_3) precursors were used as the sources of indium, gallium and nitrogen, respectively. The precursors were temporally embedded in a nitrogen carrier gas stream, such that the total flow and pressure remained constant at any given time. The $In_{0.96}Ga_{0.04}N$ epilayers were grown at a

temperature of 875 °C, a reactor pressure of 15 bar, a main gas carrier flow (N_2) of 12 slm (standard liters per minute), and a growth time of 3 hours. The details of the growth process have been published elsewhere [19, 20]. The ω-2Θ XRD results were obtained utilizing an X`Pert PRO MPD (Philips) 4-circle diffractometer equipped with a monochromatic x-ray (Cu-K_α) source. The sample was aligned prior to the measurements utilizing the substrate's sapphire (0006) Bragg reflex. The sample was rinsed with isopropyl alcohol and mounted on a tantalum sample holder with the help of tantalum clips in the UHV chamber. The details of the UHV system and sample mount have been reported elsewhere [14]. The base pressure of our UHV system was 1.5×10^{-10} Torr. Sample cleaning was performed by sputtering with 1 keV nitrogen ions followed by atomic hydrogen cleaning (AHC). Atomic deuterium cleaning (ADC) was also performed in a similar way to aid in the assignment of vibrational modes. The details of sputtering and atomic hydrogen cleaning are published elsewhere [12, 15]. In order to perform the compositional analysis and monitor the cleanliness of the samples, Auger electron spectroscopy (AES) was used. HREELS, a surface sensitive technique was used to study the bonding configurations on the sample surface. HREELS experiments were performed in a specular geometry with an incident and scattered angle of 60^0 from the surface normal, and incident electron beam energy of 8.0 eV. The desorption study was carried out by heating the sample from room temperature to 935 °C by ramping at the rate of 30 °C per minute using a temperature controller. The sample was heated by the bombardment of electrons from the back of the tantalum sample holder. The temperature was measured using a chromel-alumel thermocouple. A differentially-pumped quadrupole mass spectrometer (QMS) having a pinhole in the nose cone was equipped in the UHV chamber. The sample was placed approximately 5

mm from the nose cone of the mass spectrometer and the desorbed species were monitored with the QMS while the sample temperature was ramped up.

7.4 Results and discussion

The x-ray diffraction pattern for the $In_{1-x}Ga_xN$ recorded in ω-2Θ-geometry is shown in Fig. 7.1. The XRD spectrum shows three prominent peaks at 31.41°, 32.86° and 34.51°. The peaks at 31.42° and 34.51° are assigned to hexagonal $In_{1-x}Ga_xN$(0002) and GaN(0002) Bragg reflexes, respectively. Our studies found that the peak centered at 32.86° can be assigned to residual metallic indium at the surface, related to the In(101) Bragg reflex. The indium on the surface can be removed by 2 minutes wet etching in HCl after which the In(101) Bragg reflex at 32.86° is no longer observed [15]. The XRD results exhibit single $In_{1-x}Ga_xN$(0002) Bragg reflex, indicating no macroscopic observable phase separation. XRD spectra were analyzed by Gaussian curve fitting to determine the position and full width at half maximum (FWHM) of the (0002) Bragg reflex. The position and corresponding miller indices of this Bragg reflex were evaluated together to calculate the lattice parameter 'c' of the $In_{1-x}Ga_xN$ layers [21]. The composition of the $In_{1-x}Ga_xN$ epilayers were estimated using Vegard's law, which assumes a linear dependence of the ternary lattice parameters and their binaries alloys GaN and InN, respectively. Neglecting further any interfacial strain effects on XRD spectra, the lattice parameter 'c' can be expressed as,

$$c_{InGaN} = x.c_{InN} + (1 - x).c_{GaN} \quad (7.1)$$

from which x can be determined by

$$x = \frac{c_{InGaN} - c_{GaN}}{c_{InN} - c_{GaN}} \quad (7.2)$$

Using equation (7.2), the indium and gallium compositions in the sample were found to be 96% and 4% respectively. The indium and gallium compositions were also calculated using AES

measurements. The indium and gallium percentage in the sample as obtained from AES measurements were in excellent agreement with those obtained from XRD measurements.

Several papers have reported the bonding configurations on the surface of GaN [14, 22-27] and InN [11-13, 15, 28] samples using HREELS. On the GaN surface, the intense loss peak at 700 cm^{-1} has been assigned to the Fuchs-Kliewer (F-K) phonon [22-27]. The loss peaks at 1400, 2100, 2800 and 3500 cm^{-1} are assigned to the multiple loss peaks of the F-K phonons [22, 24-27]. Bellito *et al.* [14] performed HREELS experiments to study the hydrogenated GaN surface. From these observations, they confirmed the Ga-polarity of the MOCVD-grown GaN. Similar experiments were performed on HPCVD-grown InN samples by Bhatta *et al.* [11-13]. The loss peak at 550 cm^{-1} was assigned to F-K surface phonon [29]. A loss peak was seen at 3260 cm^{-1} (2410 cm^{-1}) for the AHC (ADC) surface which they assigned to an N-H (N-D) stretching vibration. Since N-H termination of the surface was observed but no In-H, N-polarity indium nitride was concluded. To our knowledge, no such studies have been reported on the ternary $In_{1-x}Ga_xN$ alloys using HREELS. In this paper, the bonding configuration of HPCVD-grown $In_{0.96}Ga_{0.04}N$ surface is reported. Assigning the modes of vibration, the polarity of the $In_{0.96}Ga_{0.04}N$ sample is also reported.

HREEL spectra of HPCVD-grown $In_{0.96}Ga_{0.04}N$ sample after AHC and ADC are depicted in Fig. 7.2. An intense loss peak is observed at 600 cm^{-1} in both hydrogenated and deuterated surfaces. We assign this loss peak to an F-K surface phonon. A loss peak is observed at 3280 cm^{-1} (2420 cm^{-1}) for the AHC (ADC) surface. This peak is assigned to an N-H (N-D) stretching vibration [30]. The Ga-H and Ga-D stretching vibrations have been reported at 1830-1875 cm^{-1} and 1340-1360 cm^{-1}, respectively, on the hydrogenated GaAs surface [31, 32]. The In-H stretching vibration has been reported at 1650-1750 cm^{-1} in HREELS experiments on InP

surfaces [33-35]. However, no loss features in these ranges were observed in the present work indicating that no In-H or Ga-H on the surface of the $In_{0.96}Ga_{0.04}N$ sample. The observation of surface N-H but no In-H or Ga-H vibrations indicates a nitrogen polar $In_{0.96}Ga_{0.04}N$ film. Two prominent peaks at 1240 cm^{-1} and 2020 cm^{-1} are observed from both AHC and ADC $In_{0.96}Ga_{0.04}N$ surfaces. These peaks are not related to hydrogen because no isotope shift is observed between AHC and ADC surfaces. The authors suggest that these loss peaks are due to surface N-N vibrational modes. In the literature, N-N stretching vibrational modes have been reported over a wide range of frequencies. De Paola *et al.* [36] and Anton *et al.* [37] reported N-N stretching mode of vibration on a Ru(001) surface at 2195 cm^{-1} and 2200-2250 cm^{-1}. Apen and Gland [38] observed the N-N stretching mode on the GaAs surface at 1671 cm^{-1}. So, it is suggested that the loss peak at 2020 cm^{-1} is due to a surface N-N stretch while the loss peak at 1240 cm^{-1} could be due to a N-N bend. The prominent loss peaks related to N-N vibrations indicate the presence of a significant amount of surface defects in the film [39].

In our previous study [18], we reported on the thermal stability of InN epilayers grown by HPCVD. The onset of nitrogen desorption was reported at around 630 °C and the activation energy was calculated to be 1.6 ± 0.2 eV which was independent of the group V/III precursors ratio. In this work, the thermal stability of HPCVD-grown $In_{0.96}Ga_{0.04}N$ epilayers has also been studied using TPD following the same procedure as in the previous work [18]. The desorption of molecular nitrogen from $In_{0.96}Ga_{0.04}N$ with increase of temperature is shown in Fig. 7.3. No significant NH_3 (17 amu) desorption was observed. The 14 and 28 amu desorption signals showed identical behavior at 600 °C < T< 820 °C. This confirms desorption of nitrogen from the InN samples in the form of N_2. The desorption of nitrogen started at around 625 °C, increased rapidly with increasing temperature, and peaked at 740 °C before decreasing as shown in Fig.

7.3. After attaining the peak value, the desorption rate decreased with the increase of temperature indicating that the film was getting thinner and thinner until the film was desorbed completely. Though the signal to noise ratio for indium and gallium desorption was not as good as that for nitrogen, the desorption pattern of indium and gallium (not shown) was observed to be similar to that of nitrogen. After 820 °C, the desorption of 28 amu increased again with the increase of temperature. However, the desorption of 14 amu remained unchanged with the increase of temperature beyond 820 °C. This is attributed to the desorption of CO from the GaN template. A similar trend was observed between the temperature range 250-350 °C. This is also attributed to the desorption of CO. The activation energy for the desorption of nitrogen from $In_{0.96}Ga_{0.04}N$ was calculated using the slope of the best fit line for the linear region of the Arrhenius plot. The details of calculating the activation energy have been reported previously [18]. We report that the activation energy of the nitrogen desorption from the $In_{0.96}Ga_{0.04}N$ sample is 1.14 ± 0.06 eV. Thaler *et al.* [40] have reported an activation energy of 0.87 ± 0.07 eV for nitrogen desorption from $In_{0.18}Ga_{0.82}N$ film. These results indicate that activation energy of nitrogen desorption from $In_{1-x}Ga_xN$ film may depend on indium or gallium incorporation in the film. The studies on thermal stability of InN have indicated that a number of factors might affect the decomposition rate and activation energy. Depending upon the growth technique, film orientation and annealing medium, the activation energy for nitrogen desorption from InN varied over a broad range (1.15-4.4 eV) [18].

The present work reports the surface and bulk characterizations as well as the thermal stability of $In_{0.96}Ga_{0.04}N$ epilayers grown under high pressure which may help optimize the parameters for the growth of good quality $In_{1-x}Ga_xN$ epilayers. However, further studies are required to address several issues concerned with the performance of $In_{1-x}Ga_xN$ based devices.

As discussed before, thermal stability of $In_{1-x}Ga_xN$ epilayers may depend on the film stoichiometry and the influence of growth process conditions. However, there have not been enough studies on $In_{1-x}Ga_xN$ epilayers to know the dependence of stability on these factors and a systematic study over a broader range of x values ($0<x<1$) and growth process conditions is suggested.

7.5 Conclusion

In summary, HPCVD-grown $In_{0.96}Ga_{0.04}N$ epilayers have been studied by XRD, AES, HREELS and TPD. The XRD pattern showed a single phase InGaN film. Both XRD and AES measurements indicate 4% gallium and 96% indium incorporation in the sample. HREELS showed F-K phonons at 600 cm^{-1}. Loss peaks at 1240 cm^{-1} and 2020 cm^{-1} are assigned to N- N vibrational modes which indicate the presence of surface defects. Hydrogenated and deuterated InN surface showed N-H and N-D stretch vibrations, respectively, while no In-H and Ga-H modes were observed indicating N-polar $In_{0.96}Ga_{0.04}N$ film. The desorption of nitrogen from the sample started at 625 $^{\circ}C$ and peaked at 740 $^{\circ}C$. No significant desorption of NH or NH_2 fragments was observed. From Arrhenius plot, the activation energy for desorption of nitrogen was found to be 1.14 ± 0.06 eV.

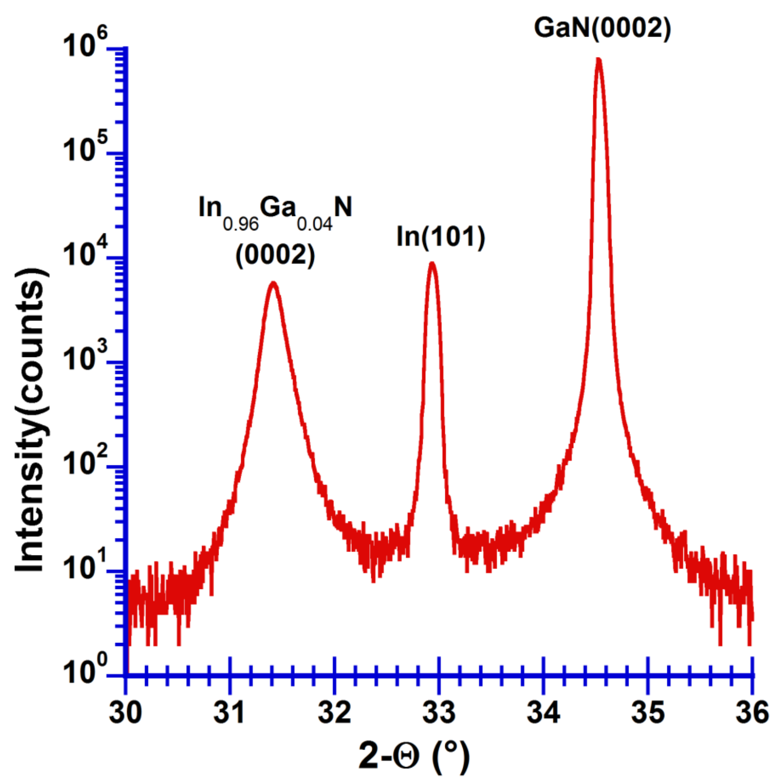

Figure 7.1 X-Ray diffraction results of HPCVD-grown $In_{0.96}Ga_{0.04}N$ in ω-2Θ-geometry.

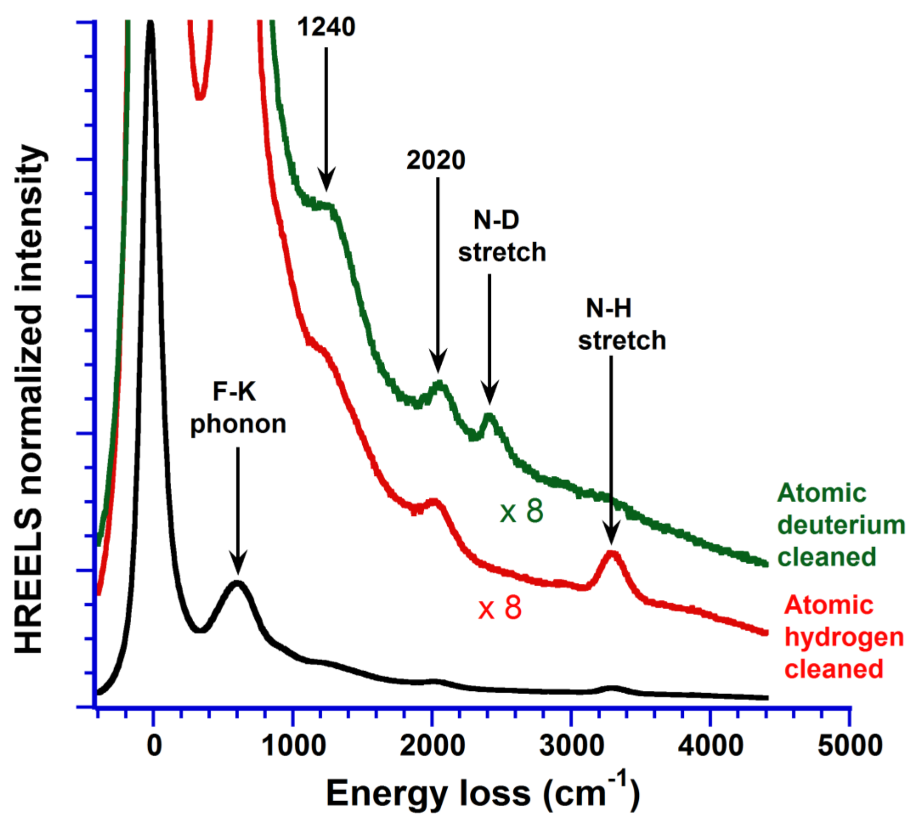

Figure 7.2 HREEL spectra of HPCVD-grown $In_{0.96}Ga_{0.04}N$ after atomic hydrogen and atomic deuterium cleaning.

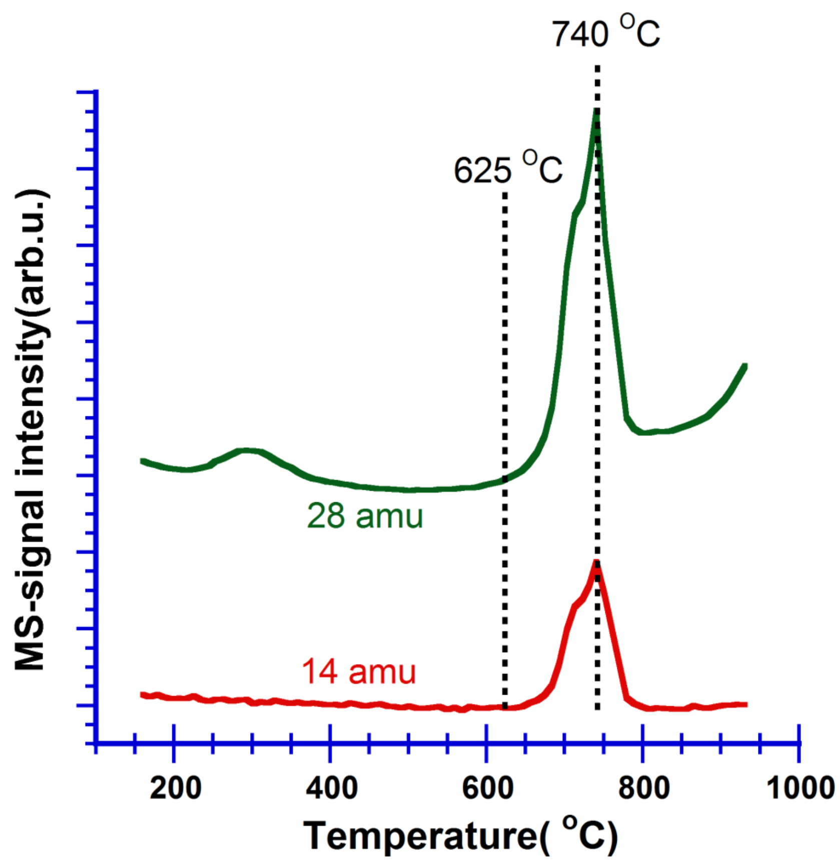

Figure 7.3 Mass spectrometer signal intensity of nitrogen species desorbed from $In_{0.96}Ga_{0.04}N$ as a function of temperature.

7.6 References

[1] J. Wu, J. Appl. Phys. **106**, 011101(2009).

[2] S. K. O'Leary, B. E. Foutz, M. S. Shur, and L. F. Eastman, J. Mater. Sci. Mater. Electron. **17**, 87 (2006).

[3] S. Nakamura and G. Fasol, *The Blue Laser Diode* (Springer, Berlin, 1997), pp. 201-260.

[4] J. Wu, W. Walukiewicz, K. M. Yu, J. W. Ager III, E. E. Haller, H. Lu, and W. J. Schaff, Appl. Phys. Lett. **80**, 4741 (2002).

[5] J. Wu, W. Walukiewicz, K. M. Yu, J. W. Ager III, E. E. Haller, H. Lu, W. J. Schaff, Y. Saito, and Y. Nanishi, Appl. Phys. Lett. **80**, 3967 (2002).

[6] V. Yu. Davydov, A. A. Klochikhin, R. P. Seisyan, and V. V. Emtsev, Phys. Stat. Sol. (b) **229**, R1 (2002).

[7] J. Wu, W. Walukiewicz, K. M. Yu, W. Shan, J. W. Ager III, E. E. Haller, H. Lu, W. J. Schaff, W. K. Metzeger, and S. Kurtz, J. Appl. Phys. **94**, 6477 (2003).

[8] K. Fujii, K. Kusakabe, and K. Ohkawa, Jpn. J. Appl. Appl. Phys., Part 1, **44**, 7433 (2005).

[9] N. Dietz, M. Strassburg, and V. Woods, J. Vac. Sci. Technol. A **23**, 1221 (2005).

[10] F. K. Yam, and Z. Hassan, Superlattices and Microstructures **43**, 1 (2008).

[11] R. P. Bhatta, B. D. Thoms, M. Alevli, V. Woods, and N. Dietz, Appl. Phys. Lett. **88**, 122112 (2006).

[12] R. P. Bhatta, B. D. Thoms, M. Alevli, N. Dietz, Surf. Sci. **601**, L120 (2007).

[13] R. P. Bhatta, B. D. Thoms, A. Weerasekara, A. G. U. Perera, M. Alevli, N. Dietz, J. Vac. Sci. Technol. A **25**, 967 (2007).

[14] V. J. Bellito, B. D. Thoms, D. D. Koleske, A. E. Wickenden, and R. L. Henry, Surf. Sci. **430**, 80 (1999).

[15] A. R. Acharya, M. Buegler, R. Atalay, N. Dietz, B. D. Thoms, J. S. Tweedie, and R. Collazo, J. Vac. Sci. Technol. A **29**, 041402 (2011).

[16] K. Xu and A. Yoshikawa: Appl. Phys. Lett. **83**, 251 (2003).

[17] K. Xu, W. Terashima, T. Hata, N. Hashimoto, M. Yoshitani, B. Cao, Y. Ishitani, and A. Yoshikawa: Phys. Stat. Sol. (c) **0**, 2814 (2003).

[18] A. R. Acharya, S. Gamage, M. K. I. Senevirathne, M. Alevli, K. Bahadir, A. G. Melton, I. Ferguson, N. Dietz, and B. D. Thoms, Appl. Surf. Sci. **268**, 1 (2013).

[19] G. Durkaya, M. Buegler, R. Atalay, I. Senevirathna, M. Alevli, O. Hitzemann, M. Kaiser, R. Kirste, A. Hoffmann, and N. Dietz, Phys. Stat. Sol. (a) **207**, 1379 (2010).

[20] G. Durkaya, M. Alevli, M. Buegler, R. Atalay, S. Gamage, M. Kaiser, R. Kirste, A. Hoffmann, M. Jamil, I. Ferguson, and N. Dietz, Mater. Res. Soc. Symp. Proc., **1202**, I5.21-1 (2010).

[21] F. K. Yam, Z. Hassan, Superlatt. and Microstr. **43**, 1 (2008).

[22] Z. Q. He, X. M. Ding, X. Y. Hou, X. Wang, Appl. Phys Lett. **64**, 315 (1994).

[23] P. Gassman, G. Schmitz, R. Franchy, Surf. Sci. **380**, L459 (1997).

[24] D. Freundt, D. Holz, H. Lüth, M. Romani, A. Rizzi, D. Gerthsen, J. Vac. Sci. Technol. B **15**, 1121 (1997).

[25] T. Tsuruoka, N. Takahashi, R. Franchy, S. Ushioda, Y. Naoi, H. Sato, S. Sakai, J. Cryst. Growth **189**, 677 (1998).

[26] V. M. Polyakov, F. S. Tautz, S. Sloboshanin, J. A. Schaefer, A. S. Usikov, B. Ja. Ber, Semicond. Sci. Technol. **13**, 1396 (1998).

[27] S. P. Grabowski, T. U. Kampen, H. Nienhaus, W. Mönch, Appl. Surf. Sci. **123**, 33 (1998).

[28] I. Mahboob, T. D. Veal, L. F. J. Piper, C. F. McConville, H. Lu, W. J. Schaff, J. Furthmüller, and F. Bechstedt, Phys. Rev. B **69**, 201307 (2004).

[29] R. Fuchs and K. L. Kliewer, Phys. Rev. **140**, A2076 (1965).

[30] C. Soto, V. Boiadjiev, and W. T. Tysoe, Chem. Mater. **8**, 2359 (1996).

[31] M. Wolf, X.-Y. Zhu, T. Huett, J. M. White, Surf. Sci. **275**, 41 (1992).

[32] S. P. Grabowski, H. Nienhaus, W. Monch, Surf. Sci. **352**, 310 (1996).

[33] N. Nienhaus, S. P. Grabowski, and W. Monch, Surf. Sci. **368**, 196 (1996).

[34] U. D. Pennino, C. Mariani, A. Ammoddeo, F. Proix, and C. Sebenne, J. Electron Spectrosc. Relat. Phenom. **64**, 491 (1993).

[35] X. Hou, S. Yang, G. Dong, X. Ding, and X. Wang, Phys. Rev. B **35**, 8015 (1987).

[36] R. A. de Paola, F. M. Hoffmann, D. Heskett, E. W. Plummer, Phys. Rev. B **35**, 4236 (1986).

[37] A. B. Anton, N. R. Avery, B. H. Toby, W. H. Weinberg, J. Electron Spectros. Relat. Phenom. **29**, 181 (1983).

[38] E. Apen, J. L. Gland, Surf. Sci.**321**, 308 (1994).

[39] A. R. Acharya, N. Nepal, C. R. Eddy, Jr., and B. D. Thoms, in preparation (2013).

[40] G. T. Thaler, D. D. Koleske, S. R. Lee, K. H. A. Bogart, and M. H. Crawford, J. Cryst. Growth **312**, 1817 (2010).

8 SUMMARY AND FUTURE WORK

8.1 Summary

The research presented in this dissertation has focused on the composition, structure, surface bonding configuration, thermal stability and hydrogen desorption kinetics of InN and InGaN epilayers grown by HPCVD and ALD techniques. These properties were analyzed using various techniques. The surfaces of the samples were prepared by sputtering with 1 keV nitrogen ions followed by atomic hydrogen cleaning in an UHV system. Sputtering and AHC removed the contaminants such as, carbon and oxygen, accumulated on the surface of the sample due to its exposure to the atmosphere. AES was used to monitor the cleanliness and investigate the composition of the samples. In order to study the surface morphology of the samples, AFM was used. The short range and long range orderings of the samples were analyzed by Raman spectroscopy and XRD, respectively. Surface bonding configurations were investigated by HREELS. The experimental IR reflection spectra were analyzed using a multilayer stack model and a Lorentz-Drude model for the dielectric of the medium to obtain the thickness of the layers. Thermal desorption experiments were carried out using mass spectroscopy and temperature-programmed desorption.

The correlations between characterizations of surface and bulk structure and bonding on HPCVD-grown InN were studied. HREELS study on InN sample grown on sapphire revealed the presence of NH_2 species. Raman spectroscopy and XRD measurements investigated the presence of tilted $(01\bar{1}\,1)$ InN crystallites. The tilted orientation of the crystals resulted in an InN surface mainly consisting of NH_2 species as observed in HREELS experiments. Growth of tilted planes in InN was a consequence of a 3D growth mode suggested to be due to the high V/III ratio and large lattice mismatch with the sapphire substrate. The thermal stability HPCVD –

grown InN epilayers was studied using thermal desorption measurements. The desorption of nitrogen from the InN surface started around 630 °C with a calculated activation energy of 1.6 ± 0.2 eV. The activation energy was found independent of the group V/III precursor ratio. The temperature at which the maximum desorption was observed shifted with increasing group V/III precursors ratio from 749 °C for a ratio 1200 to 776 °C for a ratio 4800. The analysis of surface topography suggested that this shift was related to the decreased extended defects and increased grain size with increasing group V/III precursors ratio. Corrected values for the total thickness accounting for the void fraction were calculated which correlated very well with the area under the desorption curves.

These studies have also been extended to preliminary work on the ternary alloy InGaN. The structure, composition, surface bonding configuration and thermal stability of HPCVD-grown InGaN epilayers were investigated using XRD, AES, HREELS, and TPD. Both XRD and AES measurements resulted in estimates of 4% gallium and 96% indium incorporation in the sample. HREEL spectra taken at incident energy of 7 eV showed F-K phonons at 600 cm^{-1}. Loss peaks at 1240 cm^{-1} and 2020 cm^{-1} are assigned to N- N vibrational modes which indicate the presence of surface defects. Only the modes of vibration related to N-H but no In-H or Ga-H were observed in the HREEL spectra which indicated N-polarity of the film. The desorption of nitrogen from the $In_{0.96}Ga_{0.04}N$ surface started around 625 °C with a calculated activation energy of 1.14 ± 0.06 eV.

The surface bonding configuration and desorption of hydrogen from ALD-grown InN ($000\bar{1}$) were studied using HREELS. HREEL spectra taken at incident energy of 7 eV showed Fuchs – Kliewer phonons at 550 cm^{-1} and surface N-N vibrational modes at 1240 cm^{-1} and 2020 cm^{-1}. The observation of modes of N-N vibration indicated the presence of surface defects.

Hydrogenated and deuterated InN surface showed N-H and N-D stretch vibrational modes at 3260 cm^{-1} and 2410 cm^{-1}, respectively. The modes of vibration related to In-H were not observed in the HREELS spectra. Hence the InN film was N-polar. The desorption of hydrogen from InN surface was studied by annealing the sample at different temperatures for 900 s and 90 s. The surface hydrogen was completely desorbed after annealing the sample at 425 ºC for 900 s or 375 ºC for 90 s. First-order kinetics best described the desorption of hydrogen from InN surface with an activation energy of 0.88 ± 0.06 eV and a pre-exponential factor of $(1.5 \pm 0.5) \times 10^5$ s^{-1}. The lower value of activation energy was attributed to the presence of surface defects.

8.2 Future work

The ternary compounds of III-nitride materials, $In_{1-x}Ga_xN$ alloy system have attracted significant attention to researchers due to their potential applications in the fabrication of optoelectronic device structures. They are used as the active layer in short-wavelength light emitting diodes and laser diodes [1, 2]. The optical band gap energy of the $In_{1-x}Ga_xN$ alloy system can be tuned from 3.4 eV to 0.7 eV [3,4] that covers a broad range of spectrum from ultraviolet to near-infrared region. So, use of the $In_{1-x}Ga_xN$ alloy system makes it possible to produce nitride-based light emitting diodes operating from the ultraviolet well into the infrared. The tunable band gap energy is also of interest for the development of high-efficiency monolithic multijunction photovoltaic solar cells [5]. Despite having outstanding physical properties and potential applications, however, the realization of high crystalline quality $In_{1-x}Ga_xN$ films in the entire composition range is a great challenge, particularly when a high indium concentration is required. The major challenges associated with the growth of high quality $In_{1-x}Ga_xN$ films are: higher equilibrium vapor pressure of nitrogen over InN, lattice mismatch between GaN and InN

and lower dissociation temperature of InN than that of GaN. Studies of the fundamental surface properties, surface reactions and thermal stability are an important part of gaining an understanding of the growth mechanism of the III-nitride semiconductors. We have performed such studies on GaN and InN and presented the results which have given a high impact on the growth of good quality materials. In order to study the fundamental surface properties, reactions and thermal stability of $In_{1-x}Ga_xN$ epilayers over a broad range ($0<x<1$), we would like to perform the following experiments in the future.

1) Investigation of the surface structure, composition, bonding configuration and polarity of $In_{1-x}Ga_xN$ epilayers using LEED, AES and HREELS.
2) Study of the desorption kinetics from $In_{1-x}Ga_xN$ surface using HREELS and TPD.
3) Study of the thermal stability of $In_{1-x}Ga_xN$ epilayers using TPD.

8.3 References

[1] S. Nakamura, T. Mukai, M. Senoh, Appl. Phys. Lett. **64**, 1687 (1994).

[2] I. Akasaki, S. Sota, H. Sakai, T. Tanaka, M. Koike, H. Amano, Electron. Lett. **32**, 1105 (1996).

[3] S. Nakamura and G. Fasol, *The Blue Laser Diode* (Springer, Berlin, 1997), pp. 201-260.

[4] J. Wu, W. Walukiewicz, K. M. Yu, J. W. Ager III, E. E. Haller, H. Lu, and W. J. Schaff, Appl. Phys. Lett. **80**, 4741 (2002).

[5] J. Wu, W. Walukiewicz, K. M. Yu, W. Shan, J. W. Ager III, E. E. Haller, H. Lu, W. J. Schaff, W. K. Metzeger, and S. Kurtz, J. Appl. Phys. **94**, 6477 (2003).